SLAC – 288
UC-37
(E/I)

THE ROTOR ELECTROMETER: A NEW INSTRUMENT FOR FRACTIONAL CHARGE SEARCHES*

John C. Price

Stanford Linear Accelerator Center
Stanford University
Stanford, California 94305

November 1985

Prepared for the Department of Energy
under contract number DE-AC03-76SF00515

Printed in the United States of America. Available from the National Technical Information Service, U.S. Department of Commerce, 5285 Port Royal Road, Springfield, Virginia 22161. Price: Printed Copy A10, Microfiche A01.

* Ph.D. Dissertation.

Abstract

A very sensitive electrometer with a charge resolution of less than the charge of one electron is described. The instrument has been developed in hopes that it will allow fractional charge search experiments with very large samples. The method employed is electronic, in contrast to other fractional charge search techniques which involve the measurement of a small force. Pairs of conducting pads are placed around the perimeter of a high speed magnetically levitated rotor, with one member of each pair grounded, and the other capacitively coupled to a low noise JFET amplifier. As the pads move past the stationary sample, which hangs from a quartz glass fiber, a periodic voltage proportional to the charge appears at the amplifier input. Amplifier noise limited resolution of better than one electron per root hertz may be achieved in principle, and in practice a resolution of about one third of an elementary charge has been demonstrated. Photoemission of electrons from the sample is used to calibrate the instrument directly in terms of the electron's charge.

Acknowledgements

I thank my adviser, Martin Perl, for providing the things every graduate student wants: an intriguing topic, excellent facilities, complete freedom, and a sympathetic source of guidance.

I am very grateful to Walter Innes for an enormous amount of day-to-day advice and assistance. Many technical problems would never have been solved without his help.

I would like to thank my reading committee members, David Ritson and Blas Cabrera, for their helpful comments.

Many members of the SLAC staff have contributed to this project. I would especially like to thank Ron Stickley for help with fabrication and design problems, and Ken Hughes for his craftsmanship in the machine shop.

Table of Contents

Abstract ii

Acknowledgements iii

Table of Contents iv

List of Tables vii

List of Figures viii

1. Introduction 1

2. Hadron Structure and Fractional Charge 4

2.1 The Quark Model 4

2.2 Quantum Chromodynamics 8

2.3 Alternatives to QCD 9

2.4 Models with Integer Quark Charges 10

2.5 Summary 14

3. Fractional Charge Searches 15

4. Electronic Charge Measurement 22

4.1 Basic Circuits 22

4.2 Spinning Faraday Cups 26

4.3 Other Implementations 30

5. History of the Project 34

5.1 Model I 35

5.2 Model II 38

5.3 Model III 41

6. Description of the Rotor Electrometer 43

6.1 Overview 43

6.2 Magnetic Bearing 53

6.3 Rotor 65

6.4 Rotor Drive 69

6.5 Coupling Capacitors 73

6.6 Preamplifier and Signal Processing 73

6.7 Active Horizontal Damping 79

6.8 Samples and Related Parts 81

6.9 Vacuum System 84

7. Electronic Design 87

7.1 Pad Geometry 87

7.2 Electrostatic Efficiency 90

7.3 Sample Container 96

7.4 Amplifier Noise Properties 101

8. Mechanical Design 113

8.1 Vibration and Critical Speeds 113

8.2 Rotor Materials 118

8.3 Rotor Gyrodynamics 122

8.3.1 Normal Modes 123

8.3.2 Damping of the Forward Whirl 135

8.4 Design Summary 145

9. Performance of the Instrument 146

9.1 No-sample Noise 146

9.2 Rotor Motion 147

9.2.1 Vertical Motion 147

9.2.2 Radial Motion 151

9.2.3 Phase Motion 151

9.3 Properties of Samples 153

9.4 Sample-in Noise 162

9.5 Detection of Electrons 184

10. Prospects for a Fractional Charge Search 189

REFERENCES 193

List of Tables

2.1 Quark Charges in the Han-Nambu Scheme 11

7.1 2N3686 Noise Data 108

8.1 Rotor Materials 119

8.2 Whirl Threshold Data 143

9.1 Sample O Data Runs 164

9.2 Motion Sensitivities for the SMIN Data 175

List of Figures

2.1 Pseudovector Meson $\longrightarrow e^+e^-$ 7

2.2 $e^+e^- \longrightarrow e^+e^-$ + Hadrons 12

3.1 Results of Bulk Matter Searches 17

4.1 A dc Electrometer Circuit 23

4.2 Two ac Electrometer Circuits 24

4.3 Spinning Faraday Cups 27

4.4 Background Subtraction 29

5.1 Model I Rotor, Model II Rotor, and Model III Rotor . . . 37

6.1 Cutaway Close-up View 44

6.2 Photograph of the Rotor Electrometer 45

6.3 Block Diagram 46

6.4 Photograph of the Rotor 48

6.5 Close-up Photograph of the Rotor Electrometer 49

6.6 Cutaway View of the Instrument 52

6.7 Magnet Force Versus Gap 54

6.8 Magnetic Bearing Servo Loop 56

6.9 Demodulator, Filters, Oscillator, LED Driver 57

6.10 Photodiode Preamplifier 58

6.11 Nyquist Plot 66

6.12 Mechanical Drawing of the Rotor 68

6.13 Rotor Drive Electronics 71

6.14 Preamplifier Schematic 75

6.15 Test Sample 82

7.1 Surface Potential Signal 89

7.2 Capacitance Definitions 92

7.3 Lumped Element Model 94

7.4 Sample Container Electrostatics 99

7.5 Sample Container Schematic 100

7.6 Noise Model for the Feedback Amplifier 102

7.7 FET Circuit Model 107

7.8 Measured 2N3686 Noise Parameters 109

7.9 Signal to Noise versus C_S and Frequency 111

8.1 An Unbalanced Rotor 114

8.2 Circuit Model for Dielectric Loss Noise 121

8.3 Coordinate Systems 125

8.4 Geometry for Calculation of the Driving Force 138

9.1 No-sample Noise 148

9.2 Vertical Motion Spectrum 150

9.3 Radial Motion Spectrum 152

9.4 Phase Motion Spectrum 154

9.5 Sample-in Spectra; SMIN33, SMIN34, SMIN35 165

9.6 Sample-in Spectra; SMIN37, SMIN38, SMIN39 166

9.7 Sample-in Spectra; SMIN40, SMIN41, SMIN42 167

9.8 Average and Difference Window 169

9.9 Sample-in Histograms; SMIN33, SMIN34, SMIN35 170

9.10 Sample-in Histograms; SMIN37, SMIN38, SMIN39 . . . 171

9.11 Sample-in Histograms; SMIN40, SMIN41, SMIN42 . . . 172

9.12 Sum of the SMIN Histograms 174

9.13 Sample O Noise Summary 177

9.14 Unexplained Noise 178

9.15 Least Squares Average and Difference Window 180

9.16 Test for Spontaneous Charge Changes 182

9.17 INSR31 – INSR35 and INSR36 – INSR39 185

9.18 INSR40 – INSR44 and INSR45 – INSR51 186

9.19 Photoemission Statistics 188

1. Introduction

The motivation for the work described in this thesis is the same as for Millikan's classic oil drop experiments: to discover the smallest unit of electric charge. Millikan observed a fundamental unit of charge, q_e, and proposed that the net charge of every object has the form $\pm N \times q_e$, where N is any integer or zero*. One of the most successful generalizations of physics, Millikan's rule is obeyed by all atoms and molecules, and hence by all ordinary matter. In addition, the charges of all nuclei and elementary particles observed in cosmic ray and accelerator experiments obey $q = \pm N \times q_e$.

Nevertheless it was suggested by several workers in the early 1960s that our description of the strongly interacting particles (the hadrons) could be greatly simplified if it were supposed that they were made up of constituents, dubbed "quarks" by Gell-Mann, which carry fractional electric charge equal to $\pm\frac{1}{3} \times q_e$ or $\pm\frac{2}{3} \times q_e$. To recover Millikan's rule it was necessary to suppose that 1) the sum of the quark charges in a hadron is equal to $\pm N \times q_e$ and 2) quarks are permanently confined inside hadrons, or are only liberated at energies greater than those available in accelerators. The quark model is widely accepted today because of its descriptive power. Most importantly it explains the observed multiplet structure of the hadrons.

The success of the quark model raises the possibility that isolated fractional charges might be observed. Several lines of research have been pursued since

---

* In this thesis $q_e = +1.602 \times 10^{-19}$ C, the magnitude of the electron's charge.

the early 1960s. Accelerator experiments have been done at the highest available energies to search for the production of fractional charge. To date we know that free quarks are not produced in e^+e^- collisions up to about 40 GeV (center of mass) and in $\bar{p}p$ collisions up to about 500 GeV. Experimenters have also looked for fractional charge in primary and secondary cosmic rays—here too results have been negative. In case fractional charges might be present as a rare impurity in ordinary matter, searches of the Millikan type have been done on ever larger samples. These experiments have shown that there is not more than one fractional charge per 10^{20} nucleons in several different materials, although one group reports the observation of fractional charge at a density of ~ 1 per 10^{20} nucleons in niobium (1).

The bulk of this thesis gives details of a new instrument, called a rotor electrometer, intended for a fractional charge search of the Millikan type. The technique we have chosen to pursue differs from other fractional charge search methods in that it is purely electronic and does not involve the measurement of a small force. We hope that the method will permit measurements on very large samples of arbitrary composition.

The new method involves the detection of a small alternating voltage. Pairs of conducting pads are placed around the perimeter of a high speed insulating rotor. One member of each pair is grounded. The other "signal pads" are coupled to a high impedance JFET preamplifier. As the pads spin past a conducting sample, which hangs from a quartz glass fiber, an alternating voltage proportional to the sample charge appears at the input of the preamplifier. The peak-to-peak voltage

is Q/C, where Q is the sample charge and C is the total capacitance to ground. By using a lock-in amplifier to limit the bandwidth through which noise may pass, a resolution of about $1\,q_e/\sqrt{\mathrm{Hz}}$ may be achieved in principle.

The thesis begins with a discussion of the physics motivations for fractional charge searches, followed by a brief review of the experimental results obtained to date, with emphasis on recent bulk matter searches. Our technique is introduced in chapter 4, and some other possible electronic methods are considered. The rotor electrometer project so far has progressed through three separate instruments: models I, II, and III. The central part of this thesis gives a full description of the most recent instrument, model III, which differs from its predecessors mainly in that it uses an active magnetic bearing. Chapter 5 gives a review of the lessons learned with the earlier ball bearing instruments, models I and II. In chapter 6 the details of the new instrument are presented. Chapter 7 discusses some important electronic design considerations, while chapter 8 deals with the mechanical design, and includes a treatment of the gyrodynamic normal modes of the rotor. In chapter 9 the performance of the instrument is described. The charge resolution achieved so far is shown to be $1/3\,q_e$, and the detection of single electron changes in the sample charge is demonstrated. Chapter 10 considers the prospects for a fractional charge search with the new method.

2. Hadron Structure and Fractional Charge

This chapter gives the basic physics background to fractional charge search experiments. First, we indicate why the fractionally charged quark model has become the accepted description of hadron structure and discuss the rather discouraging implications of Quantum Chromodynamics (the standard theory of quark-quark forces) for quark search experiments. Next some modifications of the standard description that might allow free fractional charge to exist are considered. Finally, it is necessary to admit that there may be viable models in which fractional charge does not exist even *inside* hadrons.

2.1 The Quark Model

The now standard model of hadron structure was introduced independently by Gell-Mann (2) and Zweig (3). All hadrons are described as bound states of spin $\frac{1}{2}$ Dirac particles called quarks which come in three flavors: up, down, and strange or u, d, and s for short*. The quarks have fractional electric charge:

Flavor	Charge
u	$+\frac{2}{3} \times q_e$
d	$-\frac{1}{3}$
s	$-\frac{1}{3}$

The hadrons with integer spin (mesons) are quark-antiquark bound states while those with half integer spin (baryons) are described as bound states of three quarks.

* To describe states above 3 GeV more flavors have been introduced.

The quark charges are chosen so that all $q\bar{q}$ and qqq (or $\bar{q}\bar{q}\bar{q}$) combinations will have integer charge, as is observed for all hadrons. Lone quarks (and combinations other than $q\bar{q}$ and qqq) will have net fractional charge.

The quark model is persuasive because it gives a simple and highly predictive account of hadrons as bound states with excitations. It is found that the states may be adequately described by nonrelativistic wavefunctions

$$\Psi_{hadron} = \Psi_{space} \times \Psi_{flavor,spin} \times \Psi_{color}. \tag{2.1}$$

The final term gives an extra degree of freedom to each quark called color. Each flavor of quark comes in three colors, and the hadrons are required to transform as singlets under $SU(3)_{color}$. Color was introduced originally so that baryon wavefunctions would be antisymmetric according to the Pauli principle, but is now required on other grounds as well. Assuming the force between quarks is to first order independent of flavor and spin, the baryons should fall into multiplets of $SU(3)_{flavor}$ and $SU(2)_{spin}$.

For the mesons the multiplicities are:

$$\begin{aligned} SU(3)_{flavor} \quad & 3 \otimes \bar{3} = 1 \oplus 8, \\ SU(2)_{spin} \quad & 2 \otimes 2 = 1 \oplus 3. \end{aligned} \tag{2.2}$$

A fermion-antifermion state has parity $P = (-)^{L+1}$ and (for neutral states) charge conjugation $C = (-)^{L+S}$, so one expects nine mesons with $J^{PC} = 0^{-+}$ and nine

with $J^{PC} = 1^{--}$ as the lowest lying states*. All these states are observed, as are many excited states, with correct P and C.

For baryons, we must take care to make the wavefunctions totally antisymmetric. The various multiplicities are:

$$\begin{aligned} SU(3)_{color} \quad & 3 \otimes 3 \otimes 3 = 10_S \oplus 8_M \oplus 8_M \oplus 1_A, \\ SU(3)_{flavor} \quad & 3 \otimes 3 \otimes 3 = 10_S \oplus 8_M \oplus 8_M \oplus 1_A, \\ SU(2)_{spin} \quad & 2 \otimes 2 \otimes 2 = 4_S \oplus 2_M \oplus 2_M. \end{aligned} \tag{2.3}$$

The subscripts S, M, and A refer to symmetric, mixed, and antisymmetric permutation symmetry. Since the color singlet is antisymmetric, and we expect the ground state spatial wavefunction to be symmetric, we must choose a symmetric flavor-spin part. Thus we expect a $J^P = \frac{3}{2}^+$ decuplet and a $J^P = \frac{1}{2}^+$ octet (an $SU(3)$ 8_M and an $SU(2)$ 2_M can be combined to make a symmetric function) as the low lying states. All these states are observed and for the nucleon, for example, whose ground state is in the $\frac{1}{2}^+$ octet, at least fifteen excited states with spin as high as $\frac{11}{2}$ have been established (4).

To establish the fractional charge of quarks the flavor symmetric decuplet is of particular interest because it contains the states *uuu*, *ddd*, and *sss*. Since these states are integrally charged, the quark constituents must be fractionally charged.

There is also direct dynamical evidence for fractional quark charge. For example, the neutral pseudovector mesons ρ^0, ω^0, and ϕ decay to an electron and

---

* J, L, and S are the total angular momentum, the orbital angular momentum, and the spin.

a positron via the process shown in Fig. 2.1. If one defines the reduced decay rates $\tilde{\Gamma}_i \equiv M_i^2 \Gamma_i$, where M_i is the pseudovector meson's mass and Γ_i is its rate to decay to e^+e^-, then using quark model wavefunctions one may derive (5):

$$q_u = \frac{1}{2} \frac{\tilde{\Gamma}_{\omega^0}^{1/2} + \tilde{\Gamma}_{\rho^0}^{1/2}}{\tilde{\Gamma}_{\rho^0}^{1/2}},$$
$$q_d = \frac{1}{2} \frac{\tilde{\Gamma}_{\omega^0}^{1/2} - \tilde{\Gamma}_{\rho^0}^{1/2}}{\tilde{\Gamma}_{\rho^0}^{1/2}}, \tag{2.4}$$
$$q_s = -\frac{1}{\sqrt{2}} \frac{\tilde{\Gamma}_{\phi}^{1/2}}{\tilde{\Gamma}_{\rho^0}^{1/2}}.$$

It has been assumed that the wavefunction at the origin is the same for each meson and the scale of charge has been fixed by requiring $q_u - q_d = 1$. Recent measurements of the M_i and Γ_i (6) then imply $q_u = +.655 \pm .018$, $q_d = -.345 \pm .010$, and $q_s = -.403 \pm .011$, in reasonable agreement with the fractional charge assignments.

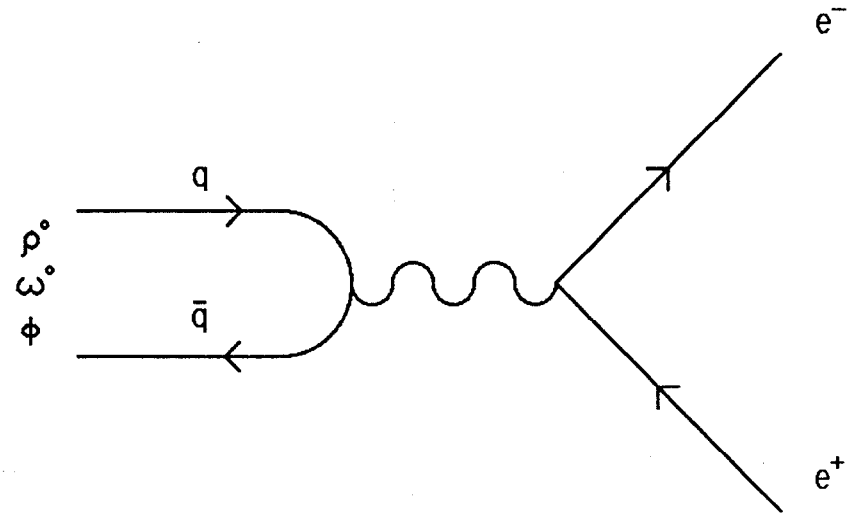

Figure 2.1. Pseudovector Meson $\longrightarrow e^+e^-$

Another example is the magnitude of R :

$$R \equiv \frac{\sigma\left(e^+e^- \longrightarrow \text{hadrons}\right)}{\sigma\left(e^+e^- \longrightarrow \mu^+\mu^-\right)}, \tag{2.5}$$

which equals

$$3 \cdot \sum_{\text{flavors}} q_i^2. \tag{2.6}$$

The factor of three is due to the colors and q_i is the charge of the i^{th} flavor of quark, where the sum runs over all flavors that may be produced at the available energy. In the region just above 10 GeV, for example, one predicts $R = \frac{10}{3}$, in agreement with the data. Other simple consequences of the fractional quark charges and an introduction to the quark model are given in the text by Close (7).

2.2 Quantum Chromodynamics

Nonrelativistic potential models of hadrons are largely phenomenological. Parameters describing the potential, quark masses, coefficients of spin-spin couplings, etc. are adjusted to match the observed spectrum (8). The description is hardly concise since for example the quark masses depend on whether the quark is in a meson or a baryon, and are not simply related to the masses deduced from deep inelastic scattering of leptons off hadrons. It is widely held that ultimately this description will be replaced by one deduced from the gauge field theory of the strong interaction, Quantum Chromodynamics (QCD). Although there are many reasons why QCD is an attractive theory, it has not yet been possible to make *any* precision comparisons with experiment.

The problem does not lie in a lack of data—the hadron spectrum contains many precisely known masses that must be explained. The difficulty is that QCD is not yet amenable to calculation. Only at high energies (above $\sim$ 10 GeV center of mass) are perturbative methods applicable so that definite predictions may be extracted. At energies relevant for quark binding in hadrons, the effective coupling constant becomes large, and no understanding via established field theory techniques is possible.

On the basis of non-rigorous arguments it is widely claimed that QCD is a confining theory, that is, the quarks and their fractional charge are permanently trapped inside hadrons. This is partly responsible for the popularity of the theory, as evidence for free fractional charge is very scarce or perhaps non-existent. The best evidence for confinement comes from numerical simulation of the field theory on a discrete lattice. The protagonists, at least, now consider that the numerical results strongly support quark confinement in QCD (9). However, it has not been clearly demonstrated that the effects of the very small lattices used so far (6^4 sites) are under control.

2.3 ALTERNATIVES TO QCD

Because QCD seems to predict confinement, and because (as will be discussed in the next chapter) there has been some evidence for fractional charge, several alternative theories of the quark-quark force have been suggested. While none of these has any particular experimental support, they serve to demonstrate that, should experiments clearly show the presence of free fractional charge, then the

theoretical framework can be adjusted to suit.

In one model proposed by De Rújula, Giles, and Jaffe (10), and discussed also by Wagoner (11) and Bjorken (12), the eight gluons of QCD (the guage particles that mediate the force between quarks) are given, via the Higgs mechanism, a common mass m_g. It is claimed that this finite mass leads to deconfinement of quarks at some finite energy. The free quark mass is $\propto 1/m_g$ and in the limit $m_g \longrightarrow 0$ the standard confining theory is recovered. A gluon mass of $\sim 20\,\mathrm{MeV}$ leads to a free quark mass of $\sim 10\,\mathrm{GeV}$ and these values are claimed to be consistent with the null results of accelerator free quark searches*, while still allowing free quark production at higher energies. Another model has been proposed by Slansky, Goldman, and Shaw (13), in which only five of the eight gluons gain mass. They suggest that the lowest mass fractionally charged state might be a diquark (qq) and that because of supressed production, it could be much lighter than the free quarks in the De Rújula, Giles, and Jaffe scheme.

2.4 Models with Integer Quark Charges

So far it has been assumed implicitly that the charge of a quark does not depend on its color and this has led to the conclusion that the quarks must be fractionally charged. In fact this constraint may be lifted and, as proposed first by Han and Nambu (14), the quarks may be given integer charges (see Table 2.1).

---

* Up to 1978 when the paper by De Rújula et. al. was written. In any case, m_g may always be taken small enough to be consistent with more recent searches.

Table 2.1. Quark Charges in the Han-Nambu Scheme

$\text{Flavor}_{\text{color}}$	Charge	$\text{Flavor}_{\text{color}}$	Charge	$\text{Flavor}_{\text{color}}$	Charge
u_{red}	$+1$	d_{red}	0	s_{red}	0
u_{yellow}	$+1$	d_{yellow}	0	s_{yellow}	0
u_{blue}	0	d_{blue}	-1	s_{blue}	-1
$\langle u\rangle_{color}$	$+\frac{2}{3}$	$\langle d\rangle_{color}$	$-\frac{1}{3}$	$\langle s\rangle_{color}$	$-\frac{1}{3}$

Note that the charge of each quark, averaged over colors, is the same as in the Gell-Mann Zweig scheme. Since all hadrons are color singlets containing equal mixtures of the three colors, the net charges of hadrons are the same as in the fractionally charged scheme. Moreover, it may be shown that for all processes involving a single photon only the quark charge averaged over color is measured (7). This follows from the $SU(3)_{color}$ symmetry properties of the electromagnetic current for Gell-Mann Zweig (GMZ) and Han Nambu (HN) charge assignments:

$$\begin{aligned} j^{\mu}_{GMZ} &= \frac{2}{3}(\bar{u}_r\gamma^{\mu}u_r + \bar{u}_y\gamma^{\mu}u_y + \bar{u}_b\gamma^{\mu}u_b) - \frac{1}{3}(\bar{d}_r\gamma^{\mu}d_r + \bar{d}_y\gamma^{\mu}d_y + \bar{d}_b\gamma^{\mu}d_b) \\ &\quad - \frac{1}{3}(\bar{s}_r\gamma^{\mu}s_r + \bar{s}_y\gamma^{\mu}s_y + \bar{s}_b\gamma^{\mu}s_b) \\ &= (+\frac{2}{3}\bar{u}\gamma^{\mu}u - \frac{1}{3}\bar{d}\gamma^{\mu}d - \frac{1}{3}\bar{s}\gamma^{\mu}s)\underbrace{(\bar{r}r + \bar{y}y + \bar{b}b)}_{1 \text{ of } SU(3)_{color}}, \\ j^{\mu}_{HN} &= \bar{u}_r\gamma^{\mu}u_r + \bar{u}_y\gamma^{\mu}u_y - \bar{d}_b\gamma^{\mu}d_b - \bar{s}_b\gamma^{\mu}s_b \\ &= j^{\mu}_{GMZ} + (\bar{u}\gamma^{\mu}u + \bar{d}\gamma^{\mu}d + \bar{s}\gamma^{\mu}s)\underbrace{(+\frac{1}{3}\bar{r}r + \frac{1}{3}\bar{y}y - \frac{2}{3}\bar{b}b)}_{8 \text{ of } SU(3)_{color}}. \end{aligned} \tag{2.7}$$

One sees that the color singlet part of the current is identical in both the integer and fractional charge schemes. Thus the dynamical evidence mentioned earlier for

fractional quark charge—all of which involves first order electromagnetic transitions between color singlet states—cannot in fact distinguish between the integer and fractional charge alternatives.

There are, however, several measurements of processes involving two photons which may be able to decide the case. For example, in e^+e^- collisions one may measure a two photon analog of R (see Fig. 2.2)

$$R_{\gamma\gamma} \equiv \frac{\sigma\left(e^+e^- \longrightarrow e^+e^- + \text{hadrons}\right)}{\sigma\left(e^+e^- \longrightarrow e^+e^-\mu^+\mu^-\right)}. \tag{2.8}$$

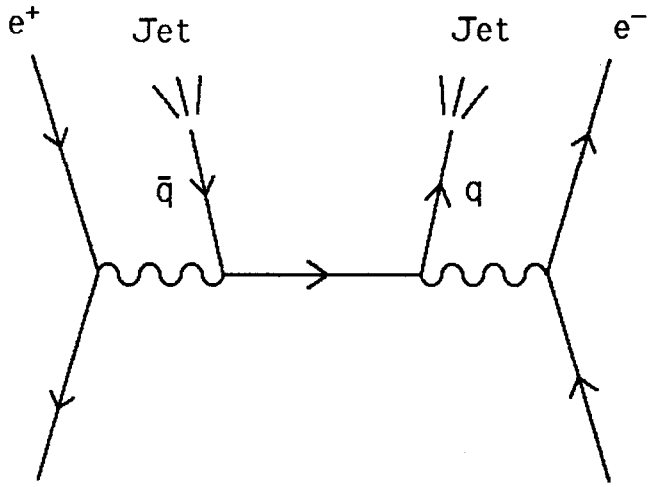

Figure 2.2. $e^+e^- \longrightarrow e^+e^-$ + Hadrons

Since the virtual quark state between the quark-photon vertices may contain a color octet part, the color octet part of the current may now give a contribution.

The predictions (for four flavors) are (15):

$$\begin{aligned} &\text{Fractional Charges} \quad R_{\gamma\gamma} = \frac{34}{27}, \\ &\text{Integer Charges} \quad\quad R_{\gamma\gamma} = \frac{10}{3}. \end{aligned} \tag{2.9}$$

Data from the PLUTO collaboration (16) clearly favors fractional charges, as does a recent measurement by the MAC collaboration of another similar two photon process (17).

Lipkin (18) and others have argued, however, that the two photon experiments may give the fractional charge result even if quarks have integer charge. It is claimed that soft gluons cause very rapid color oscillations so that even the virtual quark part in Fig. 2.2 must be a color singlet. Thus the quark charge should be averaged over colors at each vertex, and the integer and fractional charge models are not distinguishable. The situation has been further complicated by Pati and Salam (19) who point out that the combination of Han Nambu charges and QCD is not a renormalizable theory and hence cannot be fundamental. They introduce a gauged theory in which the quarks have integer charges and four of the eight gluons are massive and charged. The predictions of this theory are not the same as those of the naive Han Nambu theory and the proponents claim to be able to fit the two photon data and also single photon tests of the quark charge. There are predictions of this gauged integer charge quark model which do differ from the standard fractional charge model. In recent brief discussions of the situation Zerwas (15) indicates that the data disfavors integer charges while Field (20) concludes that the data do not

yet permit a clear test. Both authors note that the argument of Lipkin still applies and could cause the gauged integer charge model to mimic fractional charges.

2.5 SUMMARY

For the purposes of fractional charge searches at least five different possibilities may be considered:

- The quarks have fractional charge and are confined by QCD.
- The quarks are integrally charged.
- The quarks are fractionally charged but QCD does not imply perfect confinement.
- The quarks are fractionally charged but QCD is not the correct theory of the quark-quark force.
- There is something else besides a quark that is fractionally charged.

Largely because of the many negative results of fractional charge searches so far, the first possibility seems very likely to be true. Integer charge models are not very popular, but would also explain the scarcity of fractional charge. Hopes for the detection of free fractional charge rest in the last three possibilities, none of which can be excluded at present.

3. Fractional Charge Searches

An enormous amount of effort has gone into the search for fractional charge since the quark model was introduced in 1964. The cosmic ray, accelerator, and bulk matter searches done before 1977 have been reviewed by Jones (21). A general update was given by Lyons in 1981 (22), and an update emphasizing accelerator work was presented by Susinno in 1982 (23).

Searches for fractionally charged particles in cosmic rays rely on the anomalously low ionization of charge $1/3\,q_e$ and $2/3\,q_e$ particles. The early experiments used several layers of unsegmented scintillator and set flux limits around 1 to $10 \cdot 10^{-10}\,\mathrm{cm}^{-2}\,\mathrm{sterad}^{-1}\,\mathrm{sec}^{-1}$. These devices could not tolerate more than one particle traversing a layer at a time, and so could not detect fractionally charged particles that might be associated with air showers. Experiments with cloud chambers and other tracking devices have now covered this possibility. There have been no reproducible observations of fractional charge in cosmic rays. The largest experiments show that the flux of fractionally charged particles at the earth's surface is less than about $1 \cdot 10^{-11}\,\mathrm{cm}^{-2}\,\mathrm{sterad}^{-1}\,\mathrm{sec}^{-1}$ (21).

Accelerator searches have also been unsuccessful. The reviews referenced above describe results of proton fixed target experiments at energies up to 400 GeV, pp colliding beam experiments at up to 60 GeV center of mass, e^+e^- colliding beam experiments at up to 35 GeV center of mass, and an experiment in a broad band neutrino beam. Very recently new results have been published by the TPC collaboration working at PEP (e^+e^- at 29 GeV center of mass) (24), by the UA2

collaboration at CERN ($\bar{p}p$ at 540 GeV center of mass) (25), and by a group working at a heavy ion facility (^{40}Ar at 1.8 GeV/nucleon) (26).

Our main interest is in the bulk matter experiments, since these suggest some goals for the rotor electrometer project. The experiments come in two types, those involving enrichment schemes to concentrate the fractional charges, and those which do not. The enrichment experiments sometimes claim to have searched very large amounts of matter, as much as 20 kg. Since the results are all null the interpretation is uncertain, either the fractional charges are not present, or their behavior in matter is not as required by the enrichment scheme. Apparently no new enrichment experiments have been done since the reviews of Jones and Lyons, so the reader may look there for details.

Direct measurements of the net charge of samples of bulk matter are an unambiguous way to search for fractional charge. Figure 3.1 lists all experiments to date that have searched more than 100 μg. Excluding experiments that searched smaller quantities of the same materials, these are nearly all the results. The only other materials that have been investigated are oil (73 ng) (27), graphite (38 μg) (28), and water (51 μg) (29).

Only the experiment of LaRue, Phillips, Fairbank, and Hebard (1) claims unambiguous detection of fractional charge. The group has made 39 measurements on 13 different 100 μg niobium spheres and has observed net charges of $\pm 1/3\, q_e$ 14 different times. The experiment exploits the fact that a superconducting sample may be stably levitated in a properly shaped magnetic field. An alternating

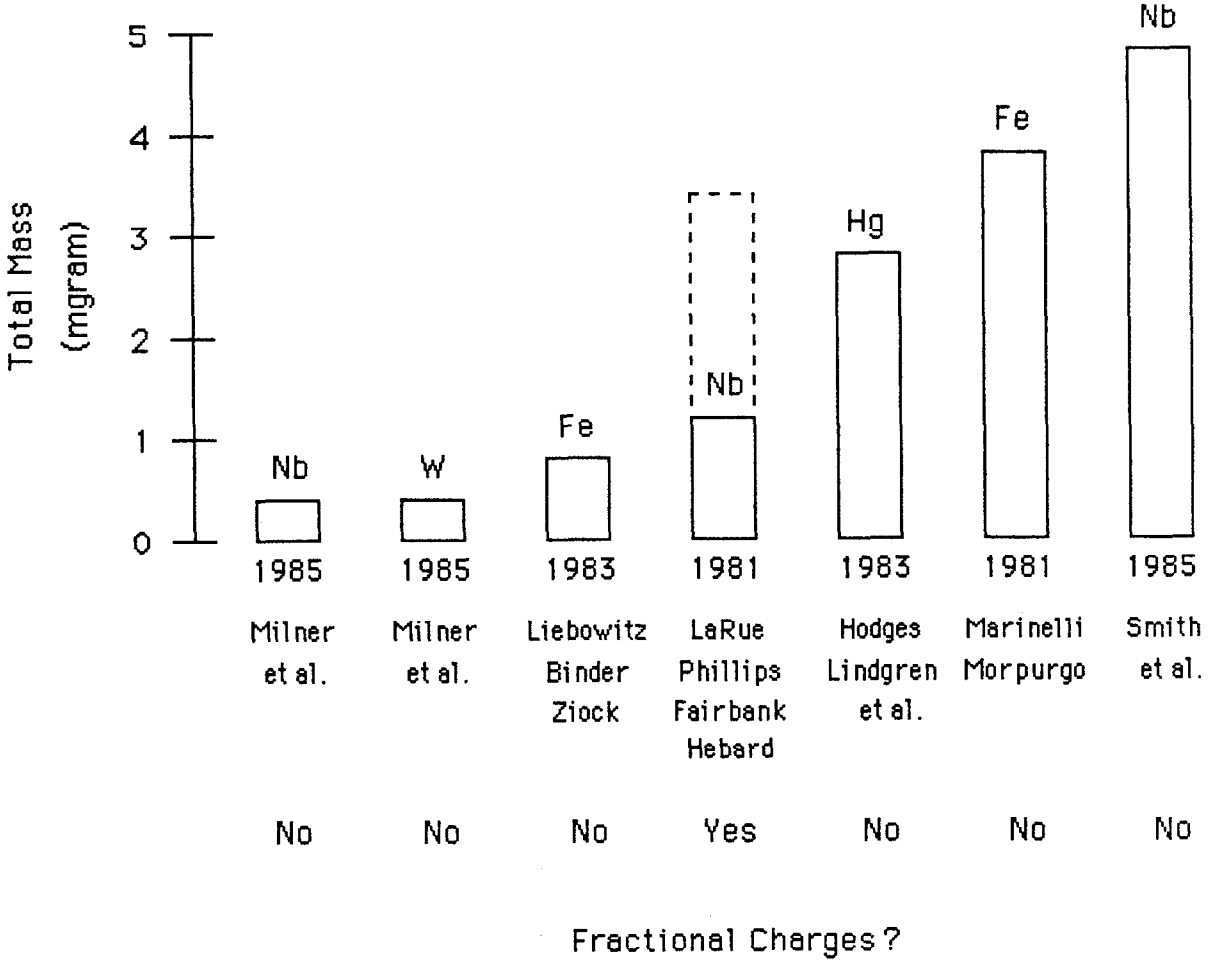

Figure 3.1. Results of Bulk Matter Searches. The dotted bar for the LaRue experiment gives the mass of the individual samples times the number of measurements. The Milner results are sensitive only to positive fractional charge.

electric field is applied to the levitated spheres, and from their motion the charge is determined.

Because the result is positive it has generated a great deal of discussion. The fractional part of the samples' charge sometimes changes if the sample is handled. This suggests that the fractional charges may be on the surface. The samples are heat treated on a tungsten substrate to improve the mechanical Q, so it may be that the fractional charges come from tungsten. Several experiments have tested specialized hypotheses regarding the LaRue *et al.* experiment (30), all with null results, but no definite conclusion can be drawn from this. No workers have undertaken to repeat this difficult experiment, but very recently one group has searched a similar quantity of niobium, as will be discussed shortly.

The experiment of Milner *et al.* (31) is perhaps not strictly speaking a bulk matter search, since the niobium and tungsten samples were sputtered to form negative ions and then electrostatically accelerated and analyzed. The experiment is sensitive at the level indicated only for fractional charges of $+1/3\,q_e$, and in the mass range $.2 - 250\,\mathrm{GeV}$. The sensitivity is about a factor of 20 less for $+2/3\,q_e$ particles, and the experiment is blind to negative fractional charges. No fractional charges were seen.

Liebowitz, Binder, and Ziock (32) have searched 24 $30\,\mu\mathrm{g}$ steel balls using a room temperature ferromagnetic levitation system. A magnetic servo system is required for stability, and the spheres are spun about a vertical axis to reduce the effects of multipole moments. No fractional charge has been seen.

Hodges and Lindgren *et al.* (33) have searched mercury with an automated Millikan technique. The individual measurements are made on small drops (~ 5 ng) but the instrument can measure one per second, so in a few days of continuous running the milligram level may be reached. The experiment has so far been limited by reliability problems with the dropper, but it is very intriguing that if these could be solved it might be possible to measure a hundred times more material that has been processed so far. No fractional charges have yet been seen.

Marinelli and Morpurgo used a ferromagnetic levitation technique to search 3.7 mg of steel with null results (34).

Very recently Smith *et al.* have published an important new result (35). The experiment uses the ferromagnetic levitation method, but the samples are of non-ferromagnetic niobium plated with iron, so the restriction to ferromagnetic materials has been avoided. This is the first experiment since the LaRue *et al.* results to search a similar quantity of niobium. No fractional charges have been seen in a total of 4.7 mg, so there is an apparent conflict with the LaRue *et al.* data.

Several caveats may be mentioned. In an early run four measurements gave results near $\pm 1/3\, q_e$, but the authors believe this was due to a high voltage fault. Monitoring of the high voltage was added to the instrument and no further fractional results were seen. The samples used are not identical to the LaRue samples, in particular they were not heat treated on tungsten. Finally it has been suggested by Schiffer (36) that the fractionally charged species might freely diffuse through samples at room temperature but be trapped in cryogenic samples. This might

make it impossible to detect fractional charge at room temperature. None of this is very satisfying, so one eagerly awaits further results from both groups.

The present day bulk matter experiments can search about a milligram, which is $\sim 10^6$ times more material that was measured by Millikan. For the future there are two goals, to investigate a larger variety of materials, and to search larger quantities. The electrostatic accelerator technique of Milner *et al.* is limited to $\sim 100\,\mu$g by backgrounds but could profitably be used to search other materials. The magnetic levitation techniques seem to have reached their limits as far as sample size is concerned (34), but the new results of Smith *et al.* suggest that perhaps many more materials could be searched. The automated Millikan technique seems to hold promise for measuring larger quantities, and could perhaps explore other liquids.

Besides our own project, several new experiments are under way that hope to search large quantities of bulk matter for fractional charge. In 1979 Hirsch, Hagstrom, and Hendricks proposed a new technique in which a stream of droplets is shot downwards in vacuum and is deflected by a horizontal electric field (37). The flight path of the drops has to be rather long to get a measurable deflection, at least several meters. The original suggestion was that the drops would weigh 65 ng and be processed at a 10 kHz rate, so that as much as 65 g could be measured in a single day. Two separate efforts are under way to implement the idea, one at the Argonne laboratory and the other at Livermore. The Argonne group has a tower 25 meters tall (!), and in a recent discussion they propose measuring 30 ng drops at a 300 Hz rate, or about 1 g/day (38).

Williams and Gillies have proposed and begun development of an electronic fractional charge search technique (39). They hope to measure single samples weighing several grams. This method resembles our own somewhat, and will be discussed in the next chapter.

For our own experiment a sample mass of 10 mg seems like a worthwhile goal. Even a single measurement of this much material would be of interest. A measurement is expected to take 100 to 1000 seconds, so conceivably a gram or more could be searched in a day. An important advantage of our technique is that any material could be searched.

4. Electronic Charge Measurement

All of the stable matter fractional charge searches that have been done so far are force measuring experiments. In each case the sample is subject to a force equal to the product of its charge times the imposed electric field, and the resulting motion is observed. So far experiments of this type have been limited to a sensitivity of about 1×10^{-21} fractionally charged particles per nucleon. The newer force measuring techniques, the automated Millikan and dropper-tower methods, may ultimately be able to do better, while the older magnetic levitation method seems to be nearing its limits. In hopes of providing an alternative to these methods we have developed a different technique, involving the detection of a voltage rather than a force. In this chapter our design is introduced and several other electronic methods are considered. A relevant review of electrometers has been given by Barker (40).

4.1 Basic Circuits

The simplest method one might consider is illustrated in Fig. 4.1. A sample of charge Q is placed inside a Faraday cup with a capacitance C to ground, and the resulting voltage $V = Q/C$ is measured by a high impedance amplifier. The best available amplifier for this arrangement is a MOSFET. C should be made as small as possible, limited by the amplifier's input capacitance. Modern commercial electrometers are of this design and the best available instruments have a charge resolution of about 1 fC or $10^4\, q_e$ (41). Although a specialized instrument might do better, the high noise levels of amplifiers near dc are prohibitive for a charge resolution of $< q_e$, as needed here.

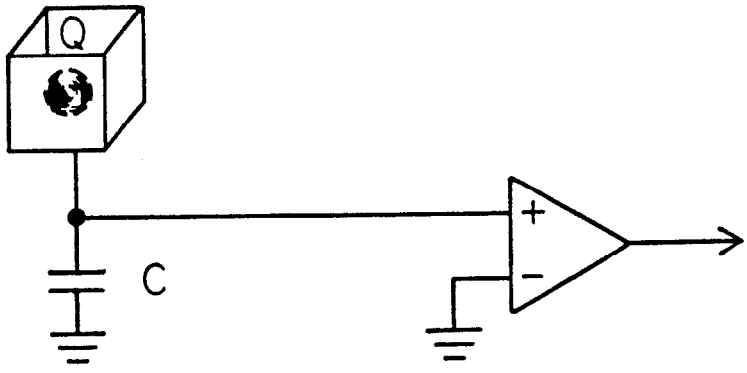

Figure 4.1. A dc Electrometer Circuit

A better approach is to periodically modulate the signal; Fig. 4.2 shows two arrangements. In Fig. 4.2(a) the charge Q is moved back and forth between two Faraday cups so that a voltage of peak-to-peak amplitude Q/C appears at the amplifier's input. The capacitance C should again be made as small as possible and will be limited by the amplifier's input capacitance. The second grounded cup is required to shield the charge from the first cup. Electrically, our rotor electrometer implements this circuit, but the geometry is completely different.

Another technique is illustrated in Fig. 4.2(b). It may be familiar as the operating principle of vibrating reed electrometers. Here the capacitance ideally varies from infinity to a minimum value C limited by the amplifier's input

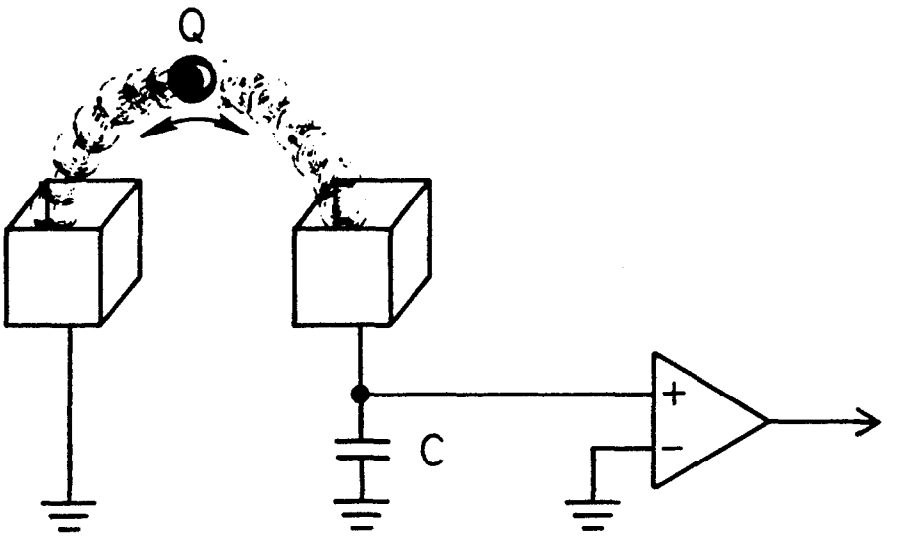

a) Our Method

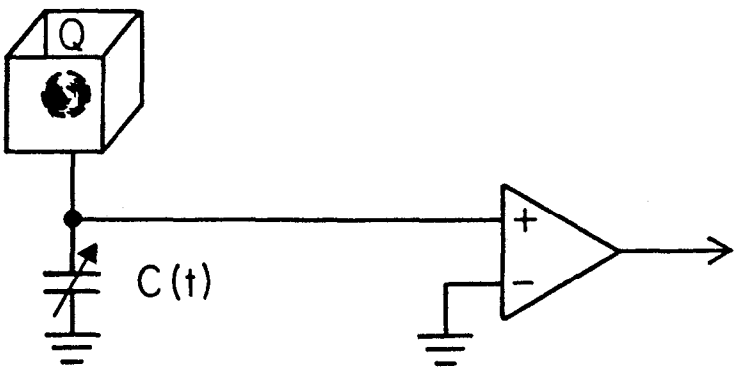

b) Vibrating Reed Method

Figure 4.2. Two ac Electrometer Circuits

capacitance. Again a voltage of peak-to-peak amplitude Q/C is generated.

Before discussing details of our device and other possibilities it may be useful to indicate the level of performance that can be achieved. The rms voltage generated for either circuit per electron charge is

$$v_e = \frac{1}{2\sqrt{2}} \frac{q_e}{C}. \tag{4.1}$$

To get the best signal to noise ratio it is important to limit the bandwidth through which noise may pass. A lock-in amplifier may be used at the operation frequency of our device and will provide a bandwidth of $1/2T$ if the detected output is averaged for a time T. Since the signal is strictly periodic the bandwidth may be narrowed indefinitely if one has patience, although in practice there may be long term drifts of the signal amplitude which limit the measurement time. If the amplifier has a total noise spectral density of S_n (V^2/Hz referred to the input) then the rms noise voltage after bandwidth limiting will be

$$v_n = \sqrt{\frac{S_n}{2T}}, \tag{4.2}$$

and so the standard deviation of the measurement error in units of the electron charge will be

$$\sigma_e = \frac{v_n}{v_e} = \frac{2C}{q_e} \sqrt{\frac{S_n}{T}}. \tag{4.3}$$

The parameters for the rotor electrometer are $C = 4.3\,\mathrm{pF}$ and $\sqrt{S_n} =$

$8.8\,\mathrm{nV}/\sqrt{\mathrm{Hz}}$ (at the 7.2 kHz signal frequency) which gives

$$\sigma_e = .47 \times \sqrt{\frac{1\,\mathrm{sec}}{T}}. \tag{4.4}$$

In practice we lose a factor of three in signal due to electrostatic inefficiencies and the noise is a factor of two higher due to disturbing effects above the amplifier noise. We are able to average the output for 200 seconds before and after a change of the sample's charge and have thus achieved a charge resolution of $\sim .3\,q_e$. These results are the best charge resolution achieved with an electronic method so far (by about three orders of magnitude), but do not yet make a fractional charge search possible.

4.2 Spinning Faraday Cups

We implement the circuit of Fig. 4.2(a) with a high speed rotor. Instead of moving the sample back and forth between two Faraday cups we leave the sample stationary and move the Faraday cups. As shown in Fig. 4.3, pairs of U-shaped cups are mounted on the perimeter of a rotor. The cups are conducting but the rotor body is insulating. Every other cup is connected via a large coupling capacitance to ground while the remaining cups are coupled through another large capacitance to the amplifier. The conducting sample hangs from an insulating quartz glass fiber. The geometry shown in Fig. 4.3, with the axis of rotation horizontal, was used for our first two instruments, models I and II.

The geometry of our current device (model III) is shown in Fig. 6.1. The Faraday cups have been reduced to copper pads plated onto the 3 cm diameter

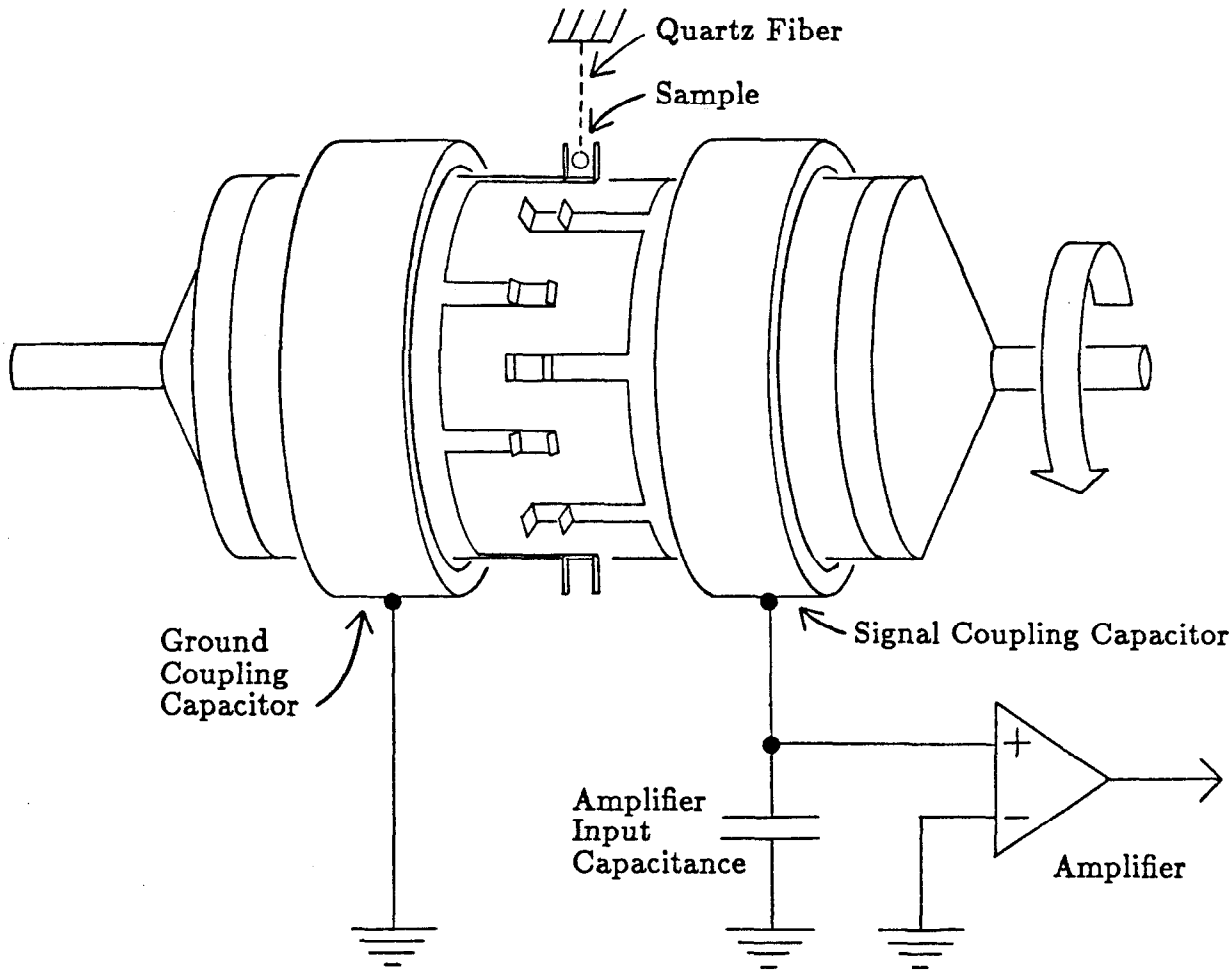

Figure 4.3. Spinning Faraday Cups

polystyrene rotor body. This is to reduce the important cup to cup capacitance which adds in parallel with the amplifier input capacitance (forming the total capacitance $C = 4.3\,\mathrm{pF}$) and limits the available signal. The device has eight pairs of pads and a rotation frequency of 900 Hz (54,000 rpm) providing a signal frequency of 7200 Hz. The rotor spins on an active magnetic bearing (instead of the ball bearings used in models I and II) for low vibration and a 10^{-7} Torr vacuum is maintained to reduce gas drag and eliminate wind on the sample. Full design details are given in chapters 6–9.

It may occur to the reader that the arrangement shown in Fig. 4.3 cannot actually be used in a fractional charge search since an unknown background signal will be generated by charges in and on the quartz fiber*. While the sensitivity to charges on the conducting sample may be directly measured (by ejecting photoelectrons, for example), charges on the fiber will be coupled to the instrument with an unknown efficiency and can mimic fractional charge.

A solution to this problem, discussed in more detail in section 7.3, is shown in Fig. 4.4. A small conducting sample container is suspended by quartz fibers and the sample itself is placed deep inside the sample container. The sample is then removed and the background signal generated by the sample container and fibers alone is measured. If the sample container is deep enough so that it forms a very good Faraday cup, then the sample-in signal minus the sample-out signal gives a measure of the net sample charge.

* There are also other backgrounds, see section 7.1.

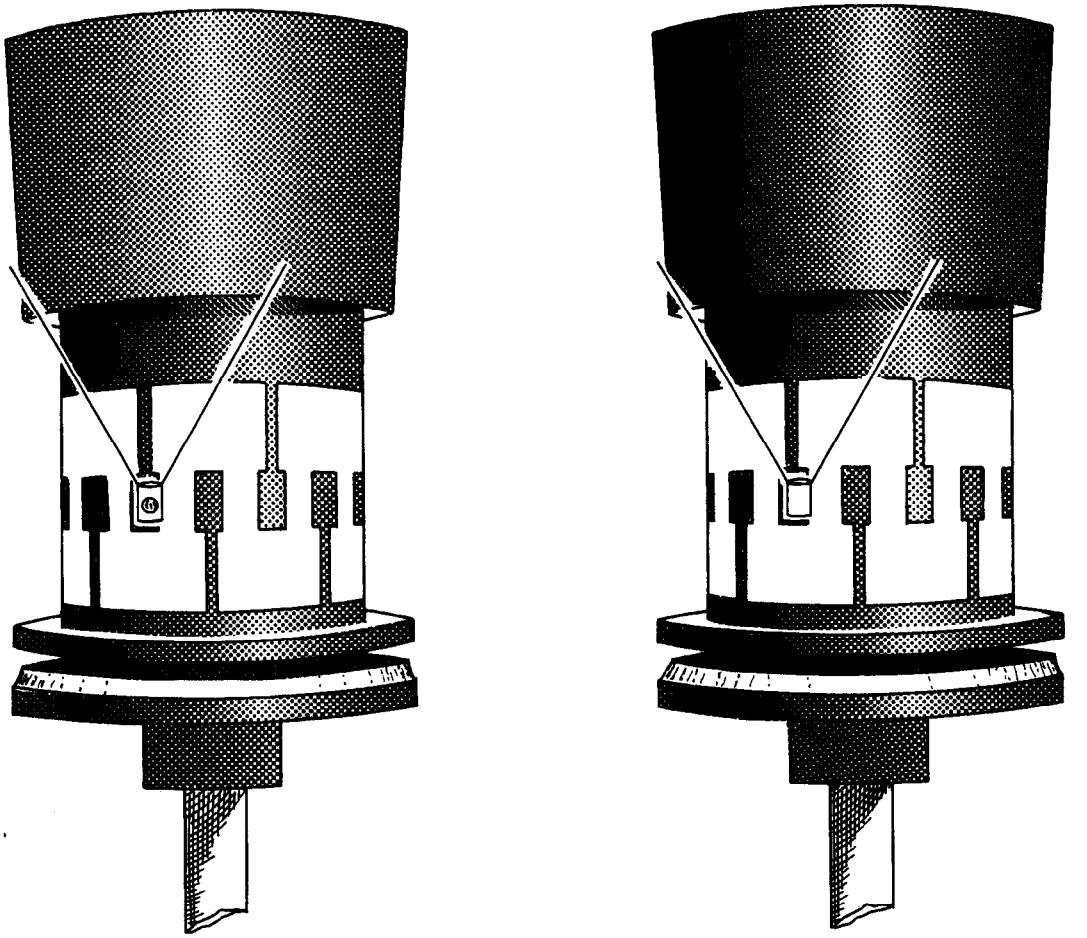

Figure 4.4. Background Subtraction

4.3 Other Implementations

The electronic method we have chosen to pursue is not the only one which may be capable of very high resolution charge measurement. Several other implementations of the circuits shown in Fig. 4.2 might also be considered. Before low noise MOSFETs became available the most sensitive electronic charge measuring instrument was the vibrating reed electrometer. Here the circuit of Fig. 4.2(b) is implemented with a parallel plate capacitor in which a vibration of one plate periodically varies the plate spacing and hence the capacitance. There seems to have been little work done on these instruments recently, but as early as 1946 Palevsky, Swank, and Grenchik achieved a charge sensitivity of $\sim 1\,\mathrm{fC}$ (42).

In principle Eqn. 4.3 above is approximately correct for the vibrating reed arrangement (with $C(t)$ periodically varying from C to a value $\gg C$), and so one should with this method also be able to achieve a resolution of order q_e or better. However, several problems can be anticipated which may make the method difficult. First of all, in real vibrating reed designs the capacitance variation $\Delta C/C$ is $\sim .1$ rather than $\gg 1$, so the instruments are inefficient. Secondly, the capacitance seen at the input of the amplifier varies periodically at the signal frequency. This has several unfortunate consequences.

First, the instrument will measure the charge that flows out of the amplifier input in the same way that it measures the sample charge. Thus the dc stability of the amplifier leakage current and of any resistor used to shunt it are a concern. In addition, the instrument will up-convert the low frequency shot noise of the amplifier

leakage current up to the signal frequency, unless the amplifier is decoupled from the varying capacitor at low frequencies. Any resistors used will generate Johnson noise near dc which also will be up-converted. Up-conversion problems are greatly reduced in the rotor electrometer arrangement since to a first approximation the capacitance seen at the amplifier's input does not vary at the signal frequency.

A final difficulty with the vibrating reed arrangement is due to the surface potentials of the conductors used to form the varying capacitance. These dc potentials will be up-converted with the full efficiency of the device and although their dc value may be nulled their drifts may not. Palevsky *et. al.* (42) observed surface potential drifts of $\sim 1\,\mathrm{nV/sec}$ in their instruments, which would correspond to $\sim .1\,q_e/\mathrm{sec}$ in an instrument with the same total capacitance as the rotor electrometer. This would be intolerable for a fractional charge search, but the problem might be solved with modern surface preparation and vacuum techniques. In the rotor electrometer arrangement surface potential effects appear also but at a reduced level, as will be discussed in section 7.1.

A variation on the vibrating reed technique has been proposed and explored by Williams and Gillies (43). These authors are the only group I am aware of other than our own working on an electronic fractional charge search technique. They implement the vibrating reed circuit of Fig. 4.2(b) but use a toothed rotor and stator arrangement as the varying capacitance. In addition the authors propose a double lock-in detection technique in which the sample is moved in and out of the Faraday cup at $\sim 1\,\mathrm{Hz}$, modulating the several kHz signal otherwise generated

by the varying capacitance. This may help to alleviate some of the difficulties mentioned above for the vibrating reed devices, which otherwise still apply. A new difficulty arises however, because the varying capacitance involves metal surfaces moving past one another. Now the *spatial* variations of the surface potentials will generate a large signal, typically $\sim 10\,\mathrm{mV}$ rms if the efficiency is high. Such a large signal will be difficult to handle, but perhaps is not a disaster since the double modulation technique moves the charge measuring signal $\sim 1\,\mathrm{Hz}$ away from the surface potential generated signal.

The method of Williams and Gillies permits all rotating parts to be grounded and conducting, which may be an important advantage in reducing sensitivity to vibrations. The authors envision that the sample would be moved in and out of the Faraday cup (without touching its sides) by magnetic levitation. This may also be an advantage, since it eliminates the quartz fibers used to suspend the sample or sample container in our scheme*.

One final method for electronic charge measurement to be considered is in some ways the most attractive—to implement the varying capacitance with solid state varactor diodes. Quite a bit of work has been done on semiconductor varactor electrometers (44) (not with fractional charge searches in mind, of course) but so far the performance of modern dc MOSFET instruments has not been equaled. The typically low conversion efficiency ($\Delta C/C \sim .1$) and up-conversion of low frequency

* With some changes in the rotor design, it might be possible to magnetically levitate our sample container. We have not pursued this.

noise are serious problems, but the very much higher frequencies now possible for the capacitance variation are a great advantage, allowing $L-C$ resonant arrangements and quieter following amplifiers. Since no clear fundamental limitations on these devices are apparent from the literature a serious study is warranted, but is outside the scope of this thesis.

5. History of the Project

The rotor electrometer fractional charge search project was conceived by Walter Innes and Martin Perl at SLAC in the Spring of 1980*. At about the same time, several other workers independently recognized that modern junction field effect transistors (JFETs) combined with lock-in amplifier noise reduction can provide sufficient charge resolution for a fractional charge search. Already mentioned are the efforts of Williams and Gillies at the National Bureau of Standards. George LaRue at Stanford did preliminary work with an instrument bearing some resemblance to ours, and Jerry Van Polen at U.C. Berkeley also conceived of a rotor technique (45).

Although unknown to us at the start, there is historical precedence for the rotor electrometer. In 1910 A. Einstein published an idea for an instrument involving rotating vanes and fixed brushes that implements a voltage multiplier circuit (46). This is quite different from the design of our device since it generates a dc rather than an ac potential. Nonetheless it encountered some of the same effects. When a prototype device was constructed by the brothers Habicht (47) it was found necessary to include a circuit to null the signal generated by surface potentials. The instrument apparently had a charge resolution of about 3 fC.

Another precursor was a rotating device published in 1932 by Gunn of the Naval Research Laboratory (48). The device achieved a charge sensitivity of about

---

* The author joined the group in April 1981 after the original prototype (model I) was built but before it was studied in the lab. Spencer Klein has also been involved in the work.

4 fC with a circuit that is a hybrid of the two discussed in the previous chapter. The instrument generated an ac signal and included a synchronous detector implemented by a mechanical commutator—an arrangement equivalent to a lock-in amplifier but 14 years prior to Dicke's classic paper (49), often cited as the source of the technique.

Our own project has progressed through three separate devices, models I, II, and III. Except in this chapter, all reference to the rotor electrometer in this thesis is to model III, the most recent instrument. All three instruments have used the same spinning Faraday cup method described in chapter 4.

Below I give an account of some of the main features of the first two instruments and of the lessons learned with them. No attempt will be made to give a detailed quantitative discussion of all the effects since many are now irrelevant, and those which are still important will be presented in the full description of model III given in the following chapters. Hopefully a brief discussion of the earlier instruments will be valuable as a list of warnings to other workers, and to more fully justify the design decisions made for model III.

5.1 MODEL I

Construction of this instrument was begun in September of 1980 and completed in April 1981, after which the instrument was studied in the lab until September 1982. A short description has been given already (50). Figure 5.1 is a photograph of the rotor from model I together with the rotor from model II and a prototype of the rotor from model III. The model I rotor was spun in vacuum ($\sim 2 \times 10^{-5}$ Torr) on a shaft supported by two ball bearings. The 53 cm long horizontal stainless steel

shaft extended through oil seals in the walls of the vacuum chamber so that the ball bearings could be located in air where lubrication is simplest. The shaft was belt driven by an electric motor. 16 pairs of Faraday cups spinning at 8000 rpm provided a signal frequency of 2.1 kHz. The machined aluminum rotor was mounted on the shaft via a G-10 insulator. The 10 cm diameter rotor was fabricated in two interleaved halves, one containing the grounded Faraday cups and the other containing the signal Faraday cups, the ones capacitively coupled to the amplifier. The signal coupling capacitor is visible in the photograph, its inner surface is cylindrical and coaxial with the shaft. The ground Faraday cups, instead of being capacitively grounded (as for model III and as shown in Fig. 4.3), were connected directly to the shaft which was in turn grounded via a fine gold plated beryllium-copper wire attached to the end of the shaft along its axis. This wire was guided into a pool of grounded mercury to which it made a low resistance contact (51). The total capacitance of the instrument, measured at the amplifier input, was about 40 pF.

The high total capacitance, discovered after the instrument was completed, was the result of underestimating the cup to cup capacitance, still an important factor in the present device. Another early discovery was the importance of dielectric loss. The lossy G-10 insulators contributed noise, disqualifying G-10 as a rotor construction material for later designs. Friction in the oil seals where the shaft passed through the vacuum walls caused a $\sim 20°C$ temperature rise of the shaft during operation, which in turn caused a large ($\sim 1\, q_e$/sec) signal drift

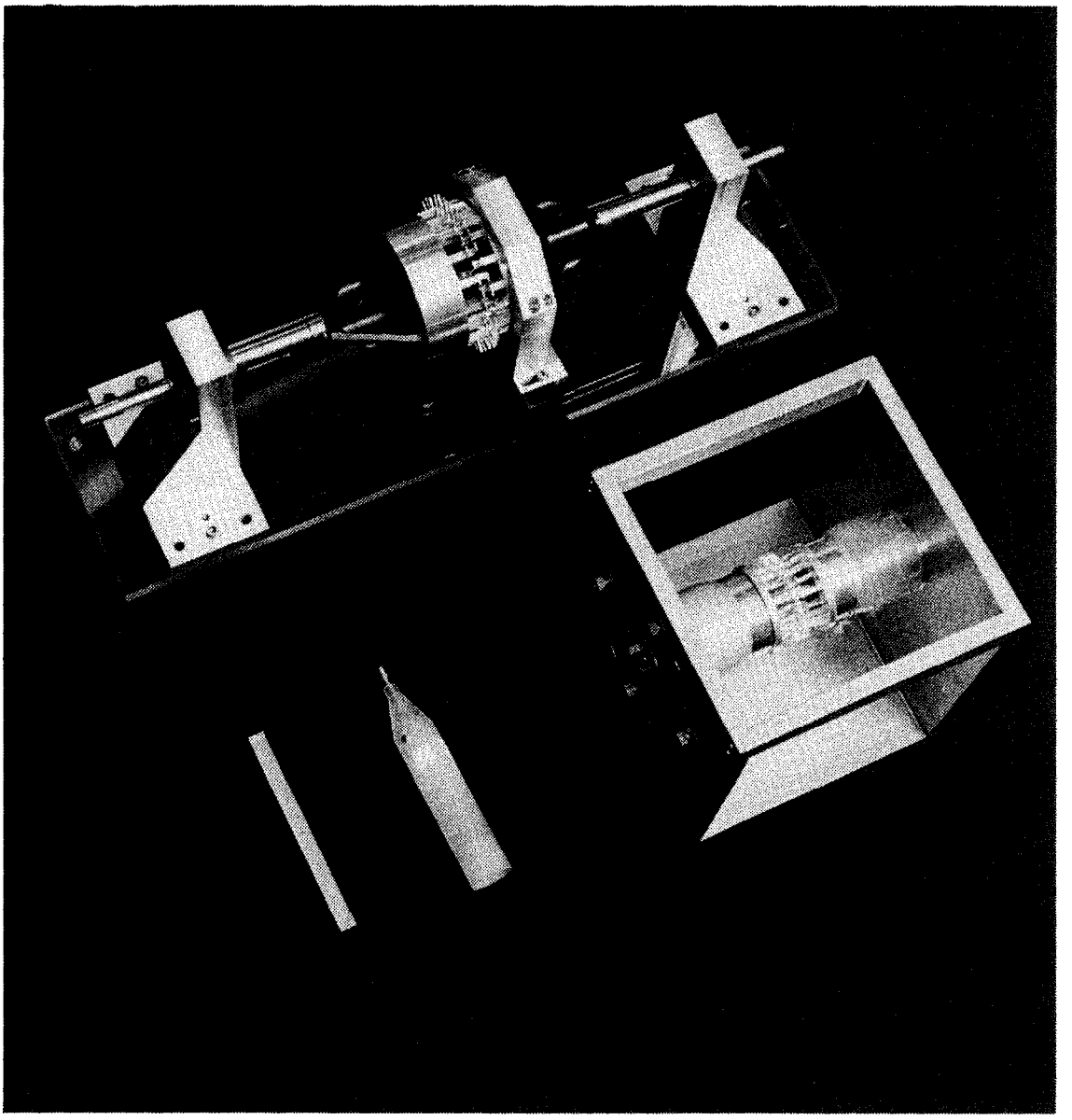

Figure 5.1. Model I Rotor (top), Model II Rotor (right), Model III Rotor Prototype (bottom, with 6 inch rule)

because of a 1 mV/°C thermoelectric coefficient in a $10^{11}\,\Omega$ resistor used to keep the rotor discharged. Another problem encountered with model I was spurious signals generated by surface potentials on metal surfaces near the spinning Faraday cups. Electric fields from the surface potentials of stationary parts not cylindrically symmetric with the shaft axis generated $\sim 100\,\mu$V rms signals.

In retrospect, we know that several other defects were present in model I, but, because they were masked by worse effects, they were not discovered until an improved device, model II, was studied. The best charge resolution achieved with model I was about $100\,q_e$.

5.2 Model II

The ball bearings and shaft of model II were completely inside the vacuum volume. Drive torque was provided by an air motor outside the vacuum and a magnetic coupling through the vacuum wall. These changes eliminated the heating problem present in model I.

The rotor and cup structure was scaled down a factor of two from model I, lowering the diameter to 5 cm and the total capacitance to about 20 pF. The rotor speed was increased considerably to $\sim 20,000$ rpm for a 5.7 kHz signal frequency, still with 16 pairs of Faraday cups. Polystyrene was used for the rotor insulator, eliminating dielectric loss as a noise source. These three changes improved the signal to noise ratio available in principle.

Curing the worst defects of model I allowed us to study a new set of limiting factors in model II. A first difficulty was the observation of excess noise above the

amplifier noise even with the rotor stationary. The source turned out to be the resistive ink used to keep the rotor and the surfaces of the polystyrene insulators discharged (52). Although the dc value of these resistors ($10^{11} - 10^{12}\,\Omega$) was sufficiently high to make their Johnson noise negligible, it was found that the real part of their impedance at the signal frequency was lower than at dc. This effect, sometimes called the Bollela effect in the literature, is commonly observed at radio frequencies but will occur at lower frequencies in very high value resistors (53).

It was necessary to abandon coating the polystyrene surfaces with resistive ink. Instead it was found possible to discharge the surfaces by soaking them in water or alcohol, and to keep them discharged by never touching them. To keep the rotor and signal coupling capacitor discharged a very narrow strip of resistive ink was used. For long narrow resistors the Bollela effect was found to be small enough.

A long time was spent studying microphonic signal generation in model II. It was found that even with the polystyrene surfaces discharged large signals could be generated by small amplitude vibrations and it was deduced that electric fields of magnitude $10^2 - 10^3\,\mathrm{V/cm}$ were present inside the polystyrene. These were apparently due to charges trapped on the polystyrene surfaces in the cracks between the metal parts and the polystyrene, and shielded from the beneficial effects of soaking by glue fillets. The device was rebuilt with carefully discharged polystyrene parts and microphonic sensitivity was thereby reduced by a factor of 100. Thus improved the device showed only amplifier noise at the signal frequency with the rotor spinning, if no sample was installed. Passing this "no sample noise test" was

an important milestone. The instrument was unfortunately unreliable, behaving well only when the bearings were at their best.

Bearing problems were a major headache with model II. Reliable operation at high speed in vacuum was never achieved with the lubrication methods tried: occasional application of a perfluoropolyether oil (54) and vacuum impregnation of the phenolic retainers (55). Bearing lifetime was limited to about 30 hours before vibrations became intolerable. It must be noted that modern turbomolecular vacuum pumps are similar systems which operate reliably, but their lubrication systems do generate significant drag and therefore heat the rotors.

In addition to vibration, the bearings were also found to generate electrical noise (most of the time), perhaps due to varying contact potentials on different parts of the balls and races. The rapidly switching signal generated by the bearings could not be completely shorted by the mercury shaft ground because of the finite inductance of the shaft and ground wire, and consequently sharp spikes contaminated the signal, growing worse as the bearings aged. The mercury shaft ground was the same as for model I except that now it had to be inside the vacuum. This made service difficult and occasional failures of the fine wire and its guides were an annoyance.

With the sample installed, the noise at the signal frequency was always several times larger than the amplifier noise, and seemed to be related to the instrument's level of vibration. At the time no quantitative understanding was achieved. We now know that it is necessary to keep the relative sample to rotor position constant

to less than 1 μm during the measurement period—perhaps this degree of stability is unattainable with ball bearings.

Model II was retired in September of 1984. The best resolution achieved with it was about 5 q_e.

5.3 MODEL III

The decision was made to abandon ball bearings and switch to an active magnetic bearing of the sort developed by J. W. Beams and co-workers (56). Although this would entail many changes in the design, significant benefits could be hoped for:

- Very low vibration due to the bearing's high compliance.
- Negligible drag and therefore negligible heating.
- No bearing electrical noise and therefore no need for a mercury shaft ground.
- Very high speeds possible.
- No possibility of oil contaminating the quartz glass surfaces of the sample suspension.
- No wear.
- Highly stable spin speed.

In redesigning the instrument to accommodate a vertical shaft (required by the magnetic bearing design) the Faraday cup structure and coupling capacitor arrangement was reconsidered. The scale was reduced still farther to a 3 cm rotor diameter with eight pairs of cups, now modified to copper pads plated onto a polystyrene body (see Fig. 6.1). The signal coupling capacitor was changed to

a disk below the lower surface of the rotor while the ground pads (née cups) were capacitively coupled to ground by a cylindrical capacitor above the pad region. These changes, especially the change from cups to pads, reduced the total capacitance to 4.3 pF, now about evenly divided between the FET input capacitance and the rotor pad to pad capacitance. As will be discussed in chapter 7, the change from cups to pads does not greatly reduce the sample coupling efficiency.

Facility was included for precise calibrated translation of the rotor and sample so that motion effects could be quantitatively studied. The rotation speed was increased to 54,000 rpm for a signal frequency of 7.2 kHz and a new vacuum system was constructed to reduce the pressure below 10^{-6} Torr. This is required to reduce gas drag so that the instrument can be used with the rotor coasting.

The expected benefits of the magnetic bearing have for the most part been realized. In the following chapters a detailed discussion of the design, construction, and performance of the new instrument is given. As in the past, study of the new instrument has uncovered a new, more subtle, set of problems, so far limiting the charge resolution to $.3\,q_e$, about 15 times better than model II and about 300 times better than model I.

6. Description of the Rotor Electrometer

A presentation of the design of the rotor electrometer (model III) begins here. For the most part this chapter is restricted to a description, while in the following two chapters a number of arguments and calculations are presented to explain how the instrument works and why certain design choices were made. We first give an overview and then proceed with details.

6.1 OVERVIEW

The main features of the device are shown in Fig. 6.1 and in the photograph Fig. 6.2. Figure 6.3 is a functional block diagram of the system.

The components of the magnetic bearing are shown in the upper left of the block diagram. A permanent magnet is used to generate a solenoidal magnetic field which supports the weight of the rotor. The arrangement is stable horizontally so that the rotation axis is drawn to the magnetic axis, but the vertical equilibrium point where the upwards magnetic force equals the downwards force of gravity is unstable, so a servo system must be used to control the vertical motion. The LED, lenses, photodiode, and associated electronics work together to measure the vertical position of the rotor. This information is used to produce a correction current in the servo coil, which generates a trim magnetic field that pushes on the rotor to make its vertical motions about the equilibrium position stable and damped. To provide damping of horizontal motions, the permanent magnet is hung as a pendulum and is allowed to move in a viscous oil bath.

The rotor itself (Fig. 6.4 and 6.12) is 18 cm long and 3 cm in diameter, and

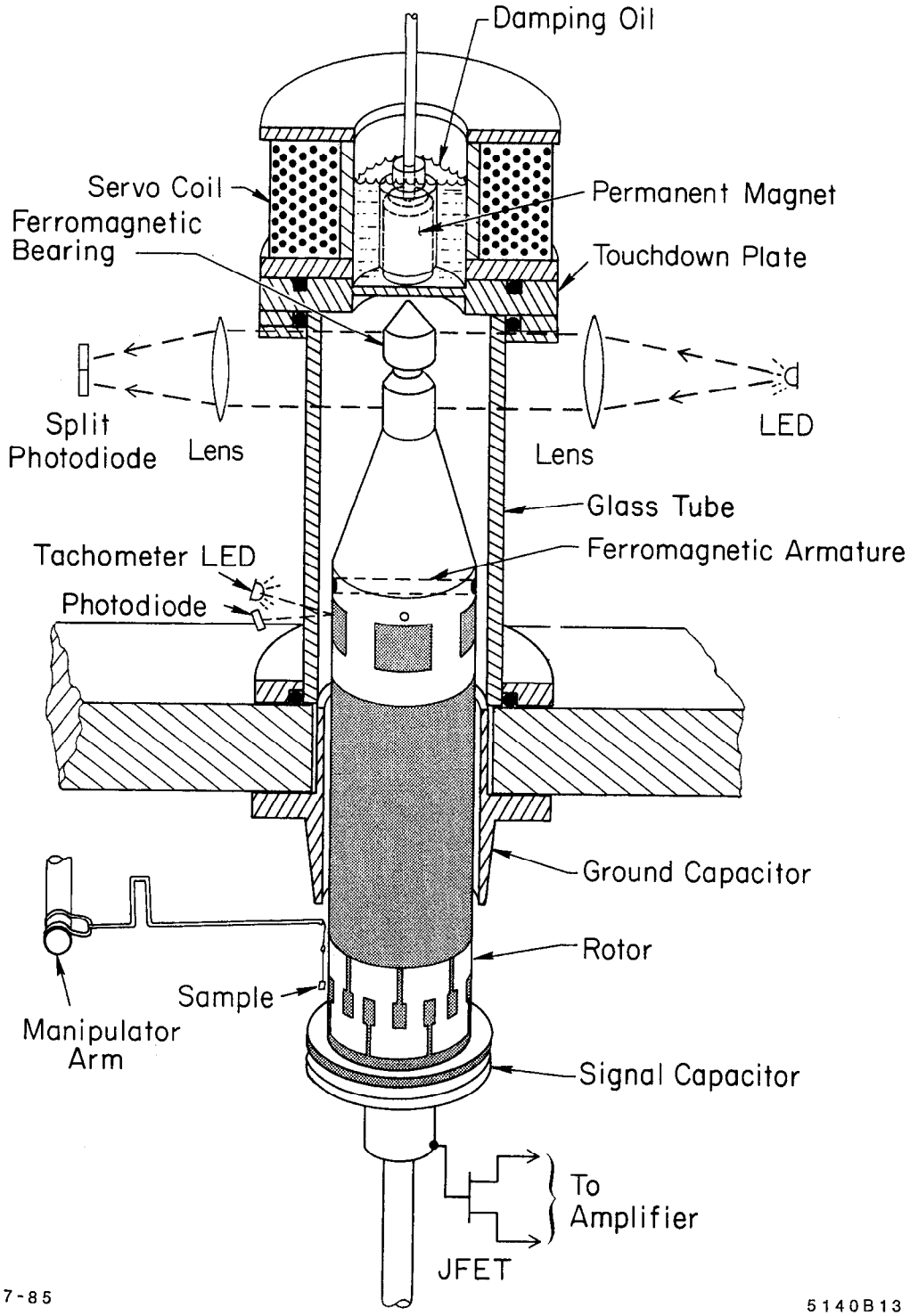

Figure 6.1. Cutaway Close-up View

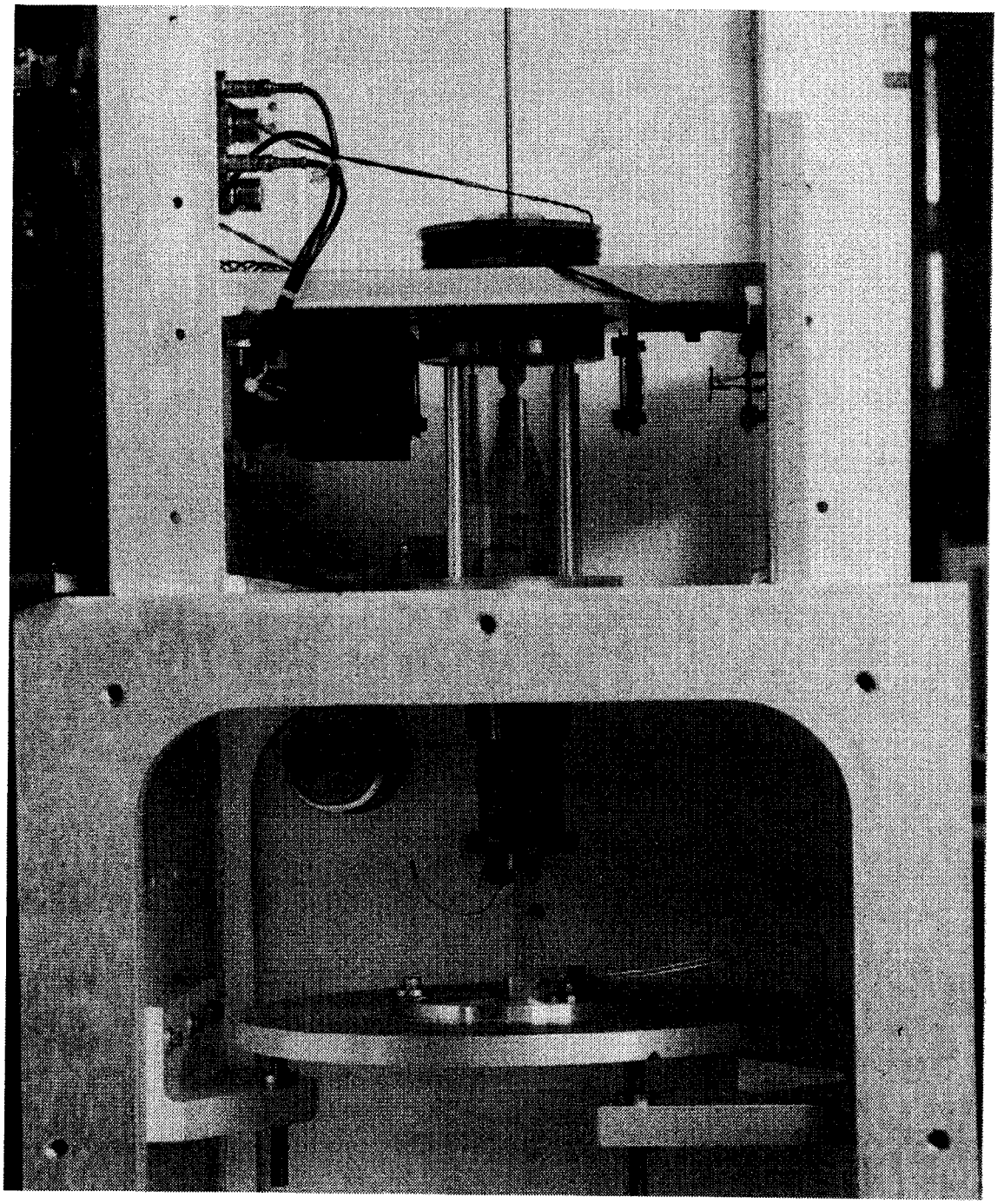

Figure 6.2. Photograph of the Rotor Electrometer (rotor drive coils, vacuum chamber cover, and Lucite shields have been removed)

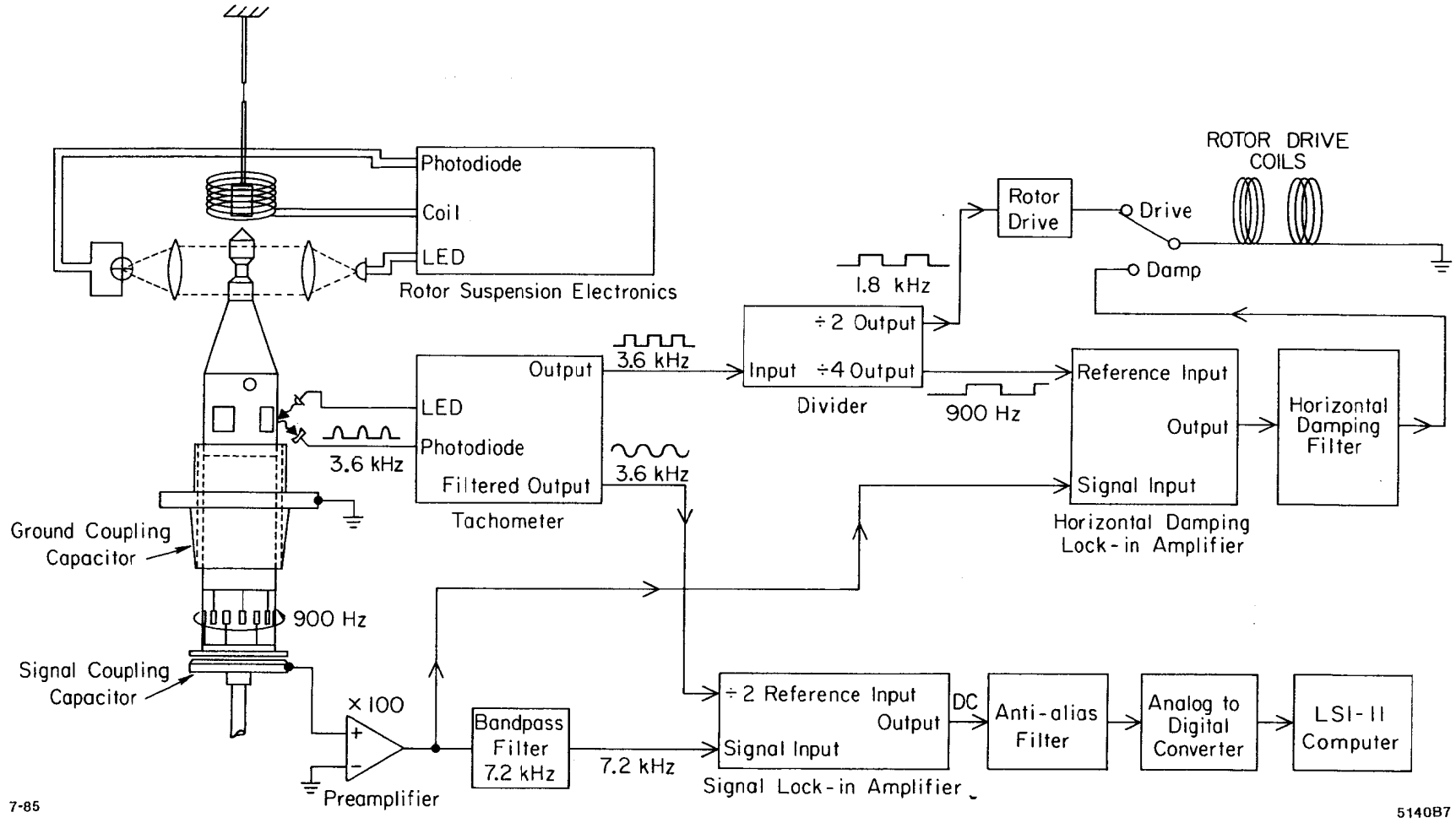

Figure 6.3. Block Diagram

is made mainly of a single piece of polystyrene. At the top is a ferromagnetic piece (called the bearing) of alloy 4750 nickel iron which supports the rotor by its attraction to the permanent magnet. The signal pads, ground pads, the surfaces that form the rotating parts of the signal and ground coupling capacitors, and four reflective squares used for the tachometer, are all copper plated onto the polystyrene rotor body. Copper traces that connect the pads to their coupling capacitors are visible in the photograph. A ferromagnetic armature, necessary to drive the rotor, is mounted along a diameter. The end of the armature is visible in the photograph as a small dark circle just above one of the tachometer squares. The dark line painted onto the rotor is resistive ink used to keep the isolated copper regions discharged. In operation the rotor spins at 900 Hz and the drag is very low so that the rotor loses only about .3 Hz/hour when coasting.

The stationary halves of the signal and ground coupling capacitor are shown in Fig. 6.1 and in the close-up photograph Fig. 6.5. Their surfaces are also copper plated. The ground coupling capacitor is bolted to the ceiling of the aluminum vacuum chamber and extends up inside a hole in the ceiling. The walls of the vacuum chamber define ground and serve as electrostatic shield. The stationary half of the signal coupling capacitor is mounted on a quartz glass insulator. The insulator is mounted on a plate supported by three fine pitch screws to allow adjustment of the capacitor gap.

Visible in the close-up photograph Fig. 6.5 next to the quartz glass insulator is the N-channel junction field effect transistor which is connected to the signal

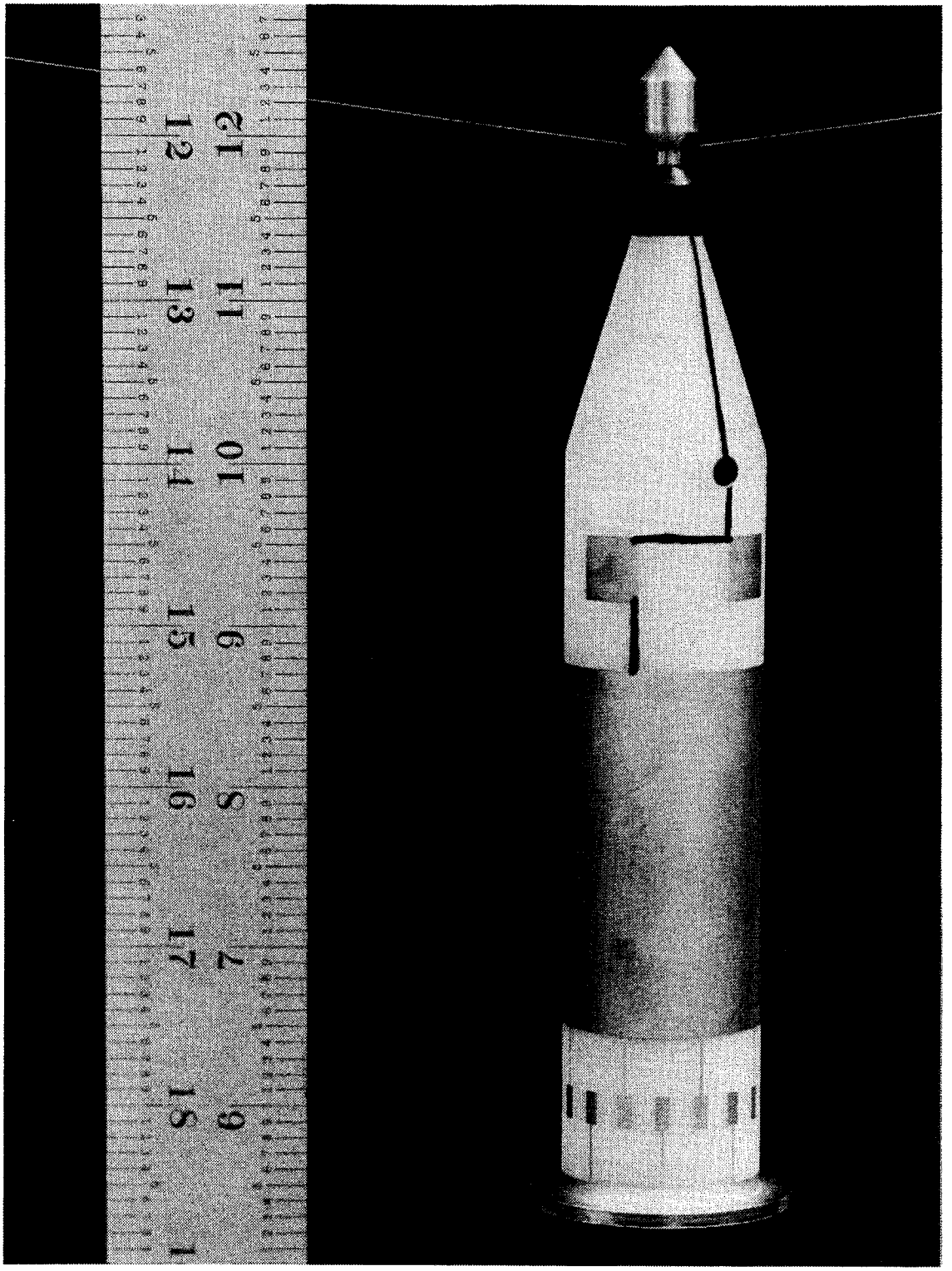

Figure 6.4. Photograph of the Rotor

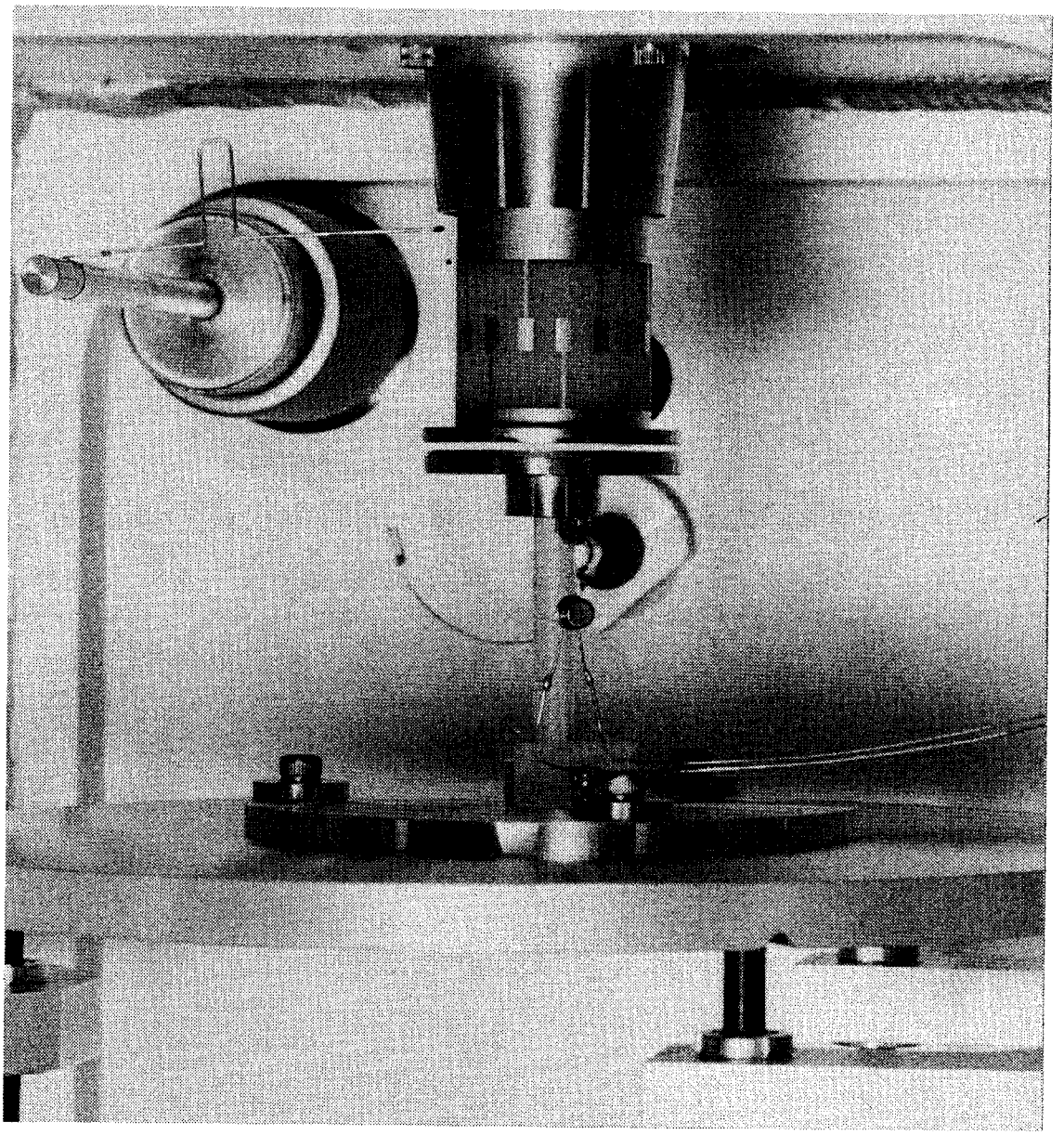

Figure 6.5. Close-up Photograph of the Rotor Electrometer

coupling capacitor. It forms the front end of the low noise preamplifier, which has a voltage gain of 100 from 100 Hz to 20 kHz. Although the charge measuring signal is always at $8 \times 900\,\text{Hz} = 7.2\,\text{kHz}$ (there are eight pairs of pads), the preamplifier is made broadband for diagnostic purposes and because the signal at 900 Hz provides a useful measure of the horizontal position of the rotor.

A conventional chain of signal processing components follows the $\times 100$ preamplifier and is shown the system block diagram Fig. 6.3. First comes a bandpass filter centered about the 7.2 kHz signal frequency, followed by the main lock-in amplifier. The nearly dc output of the lock-in is lowpass filtered to prevent aliasing and is then sampled at 1 Hz by an analog to digital converter interfaced to an LSI–11 computer.

Also shown on the block diagram are several other pieces of electronics required by the instrument. A photoelectric tachometer provides a phase reference signal for the main lock-in amplifier, and its output is divided by two to provide a signal for the rotor drive. The rotor drive supplies a unipolar 50% duty cycle current to the rotor drive coils, which apply torque to the rotor's armature. (The true placement of the coils is shown in Fig. 6.6.) An arrangement is shown in the block diagram for damping the slow (6 second period) gravitational precession of the rotor which is not well damped by the viscous oil and has a several hour time constant in the absence active damping. The horizontal damping lock-in demodulates the 900 Hz signal output by the preamplifier. As will be explained below, the dc output of the damping lock-in then provides a measure of the horizontal position of the rotor.

After spin-up the damping lock-in output is applied through a filter to the rotor drive coils, and if the lock-in phase is set correctly, the precession can be damped.

Samples are hung along the left edge of the rotor, as shown in the close-up photograph Fig. 6.5 and in Fig. 6.1. The arm from which the sample is hung enters the chamber through a stainless steel bellows. Outside the chamber the arm is attached to a precision manipulator so that the sample position may be adjusted. Various samples have been used; the one visible in the photograph is a small square of indium ($\sim 1\,\mathrm{mm} \times .5\,\mathrm{mm} \times .2\,\mathrm{mm}$) pinched onto a $3\,\mu\mathrm{m}$ diameter quartz glass fiber. The fiber is attached to the manipulator arm via a short strip of latex rubber to provide damping of the sample's pendular and torsional motions.

High vacuum is required to reduce gas drag on the rotor and to eliminate wind forces on the sample. A conventional 6 inch oil diffusion pump with a liquid nitrogen trap provides a pressure of about 2×10^{-7} Torr as measured by a cold cathode guage. The evacuated volume includes the region inside the glass tube that houses the upper part of the rotor and ends just above the rotor. Only the rotor, coupling capacitors, FET, and sample are inside the vacuum.

Figure 6.6 is a view of the entire vacuum chamber. It is mounted on a 1/2 inch thick steel plate (not shown) that overhangs from a large concrete block. A hole in the plate allows clearance for the pumping stack below the chamber. An aluminum frame above the chamber supports a three axis translation stage from which the suspension magnet hangs. Lucite shields are provided as a safety measure in the event of a rotor crash, and also to shield the device from air currents in the room.

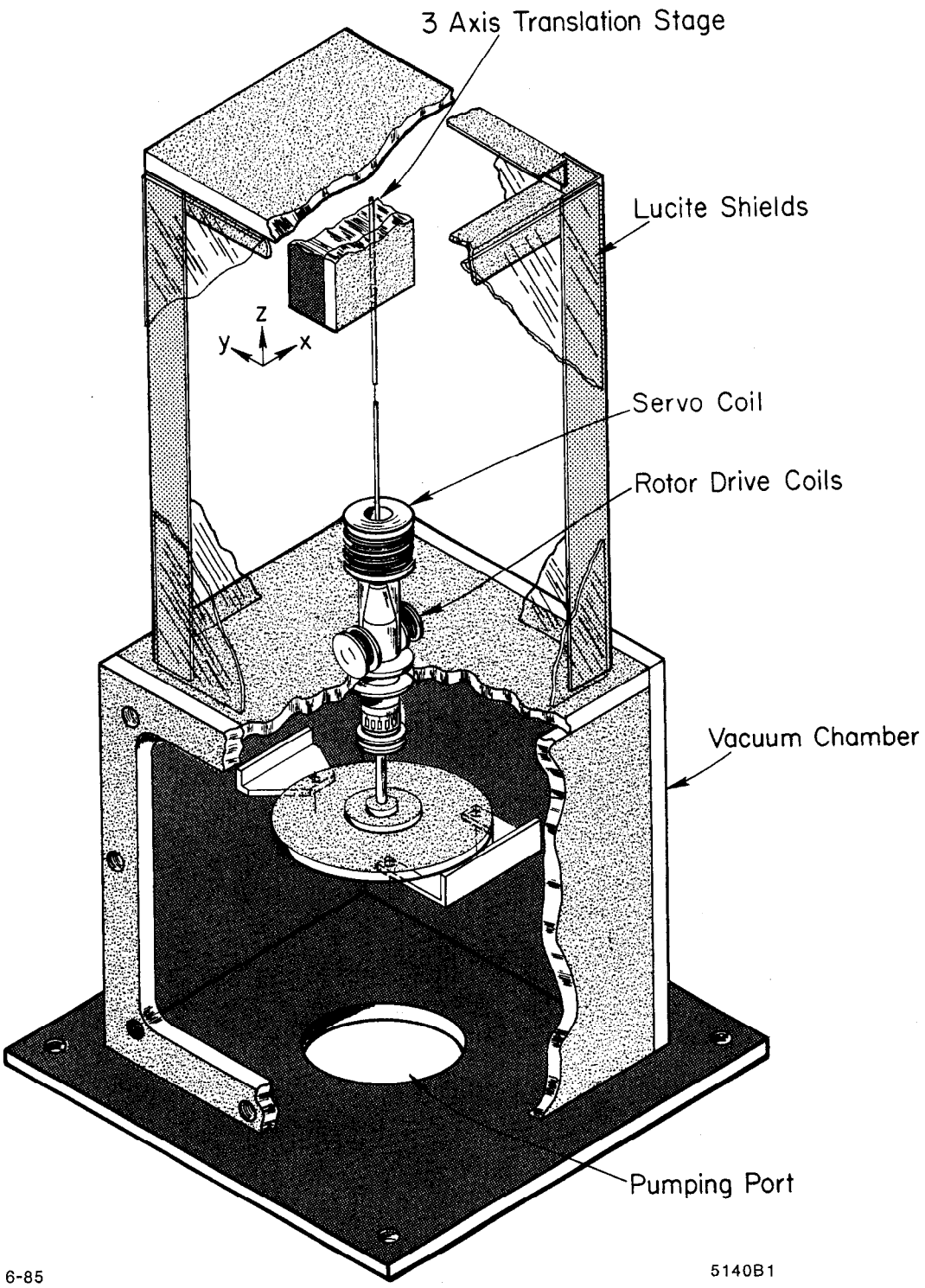

Figure 6.6. Cutaway View of the Instrument

6.2 Magnetic Bearing

Figure 6.7 shows the measured force applied to the bearing by the permanent magnet. A sufficient approximation for an analysis of the servo system is to linearize the magnet force about the unstable equilibrium that occurs when the magnet force is equal to mg, the force of gravity on the rotor. From the figure we see that this occurs at a gap of about 7 mm and the slope is

$$A = 2.3 \cdot 10^5 \text{ dyne/cm.} \tag{6.1}$$

Near the equilibrium point one may imagine that the vertical force on the rotor is due to a spring with negative spring constant equal to $-A$. As was already noted, the horizontal forces of the magnet on the bearing are stable. They may be described by a (positive) spring constant which has the measured value

$$k_x = 3.7 \cdot 10^4 \text{ dyne/cm.} \tag{6.2}$$

Samarium cobalt is chosen for the magnet material since it allows the lowest magnet mass for a given magnetic field*. Lowering the magnet mass improves the damping of the forward whirl, as will be discussed later. One should not, however, make the magnet smaller in an effort to decrease its mass since the instability force A will get larger for a given rotor mass if the magnet size is decreased. A large

* The magnet was obtained from Electron Energy Corporation, 333 Main Street, Landisville, Pa. 17538.

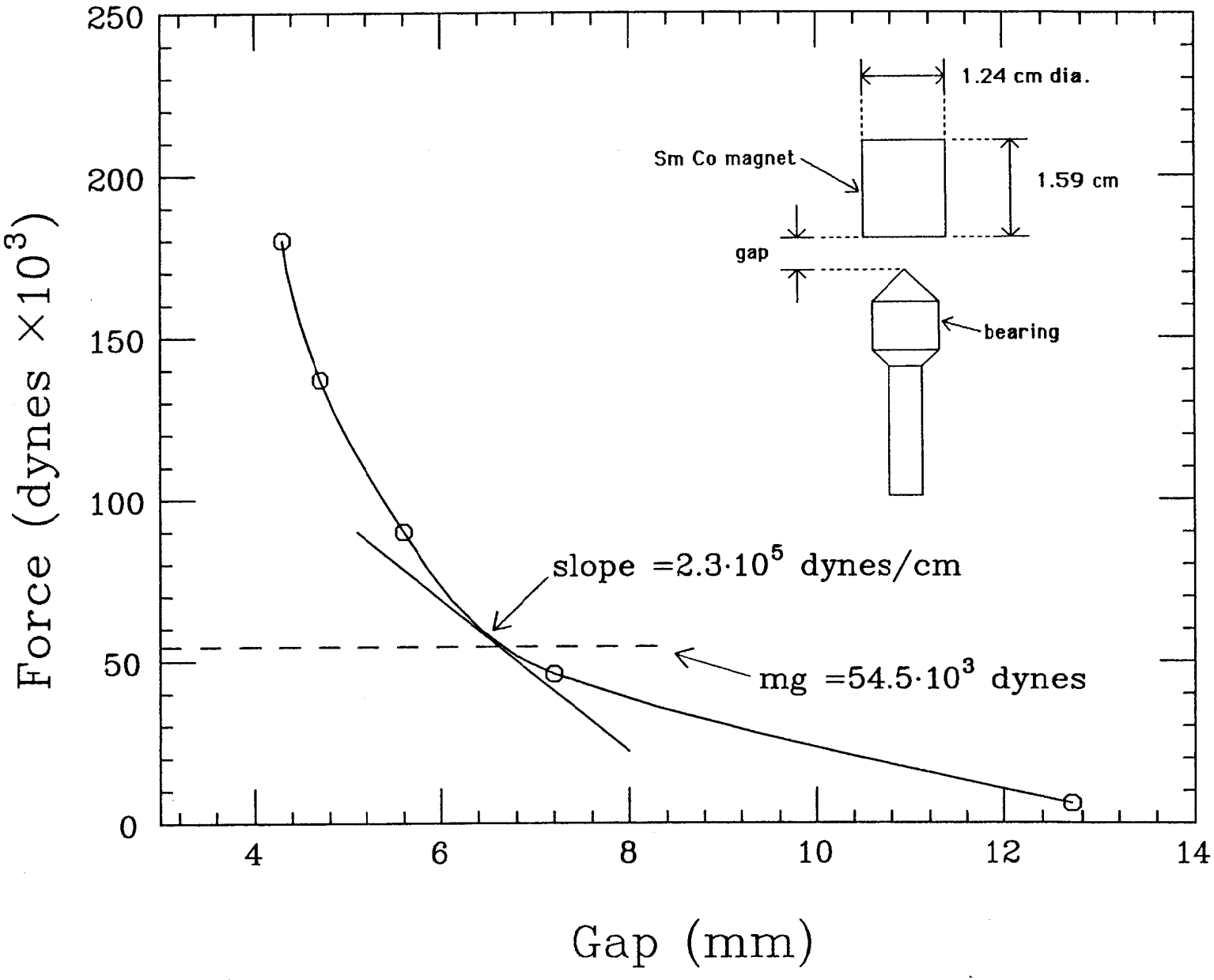

Figure 6.7. Magnet Force Versus Gap

value for A implies a small stable region for a given servo coil current range, and if the stable region is too small the system will be difficult to set up. It is not claimed that the parameters chosen here are optimal, but they have served adequately.

The purpose of the electronic servo loop, shown in Fig. 6.8, is to change the magnetic spring constant $-A$ to a positive spring constant k_z, and to provide damping for the vertical motion. Power is supplied to the servo loop by wet cells so that the rotor will not be destroyed in the event of a utility power failure. Schematics of the elements of the servo loop are given in Fig. 6.9 and Fig. 6.10. An improvement over the designs of Beams is that the light source is modulated at 7 kHz instead of being at dc. This technique (also used by Cheung *et al.* (57)) makes the system immune to room lights, which is a convenience, and makes dc stability easy to achieve.

We now describe the servo loop, starting at the lower right of Fig. 6.8. The red emitting LED approximates a point source* and a 2.5 cm diameter, 2 cm focal length, convex lens forms parallel rays. A second similar lens focuses a shadow of the constriction in the rotor onto a split photodiode; the shape of the shadow is shown in the figure. The photodiode is a 1 cm diameter quadrant† with the two upper and two lower quadrants connected together. It is mounted on a vertical translation stage so that the magnetic and optical neutral points may be aligned together. A

---

* The plastic lens of the LED was ground flat and polished.

† Model #SD-380-23-21-051 from Silicon Detector Corp., 885 Lawrence Drive, Newbury Park, CA 91320.

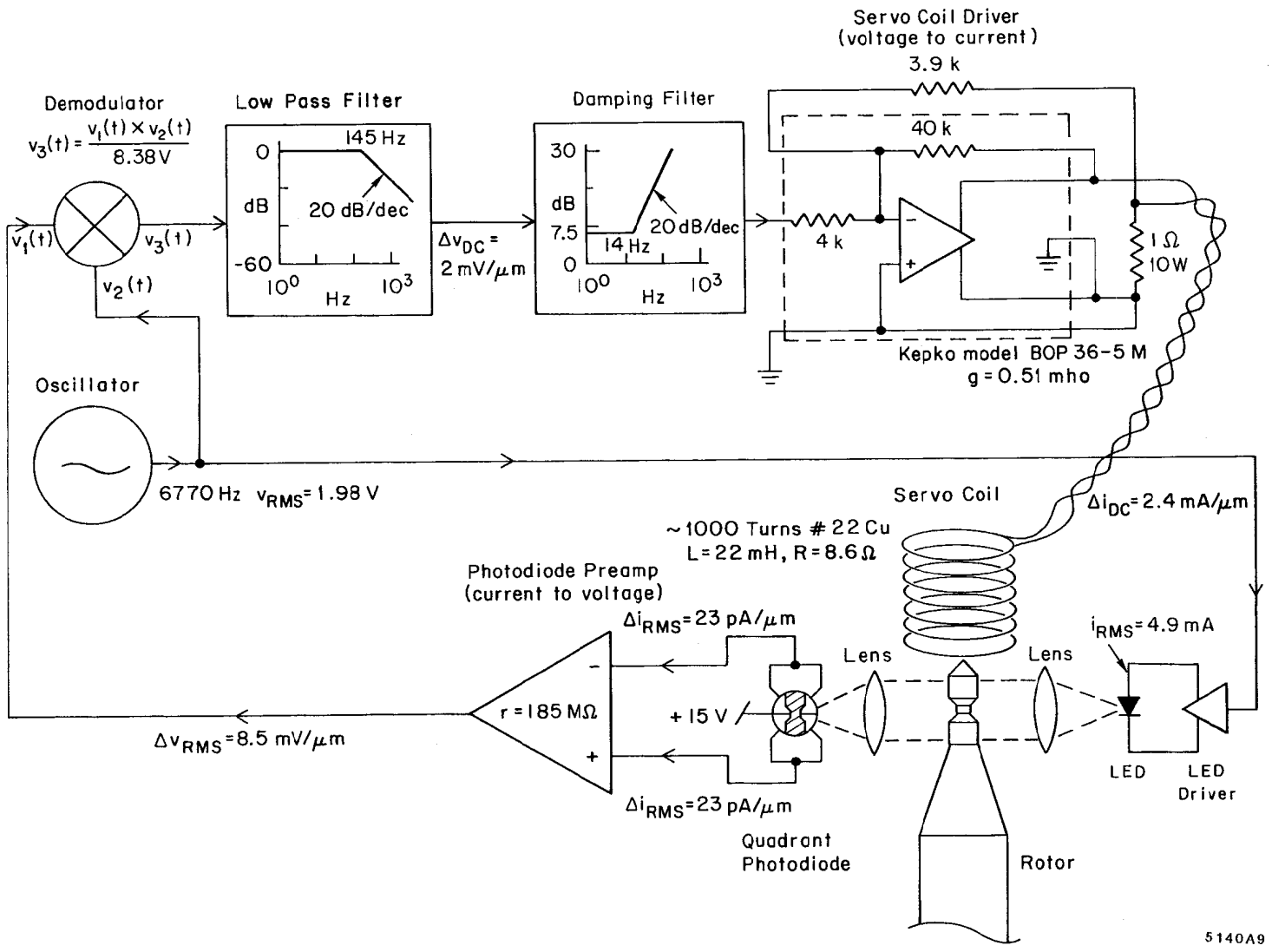

Figure 6.8. Magnetic Bearing Servo Loop

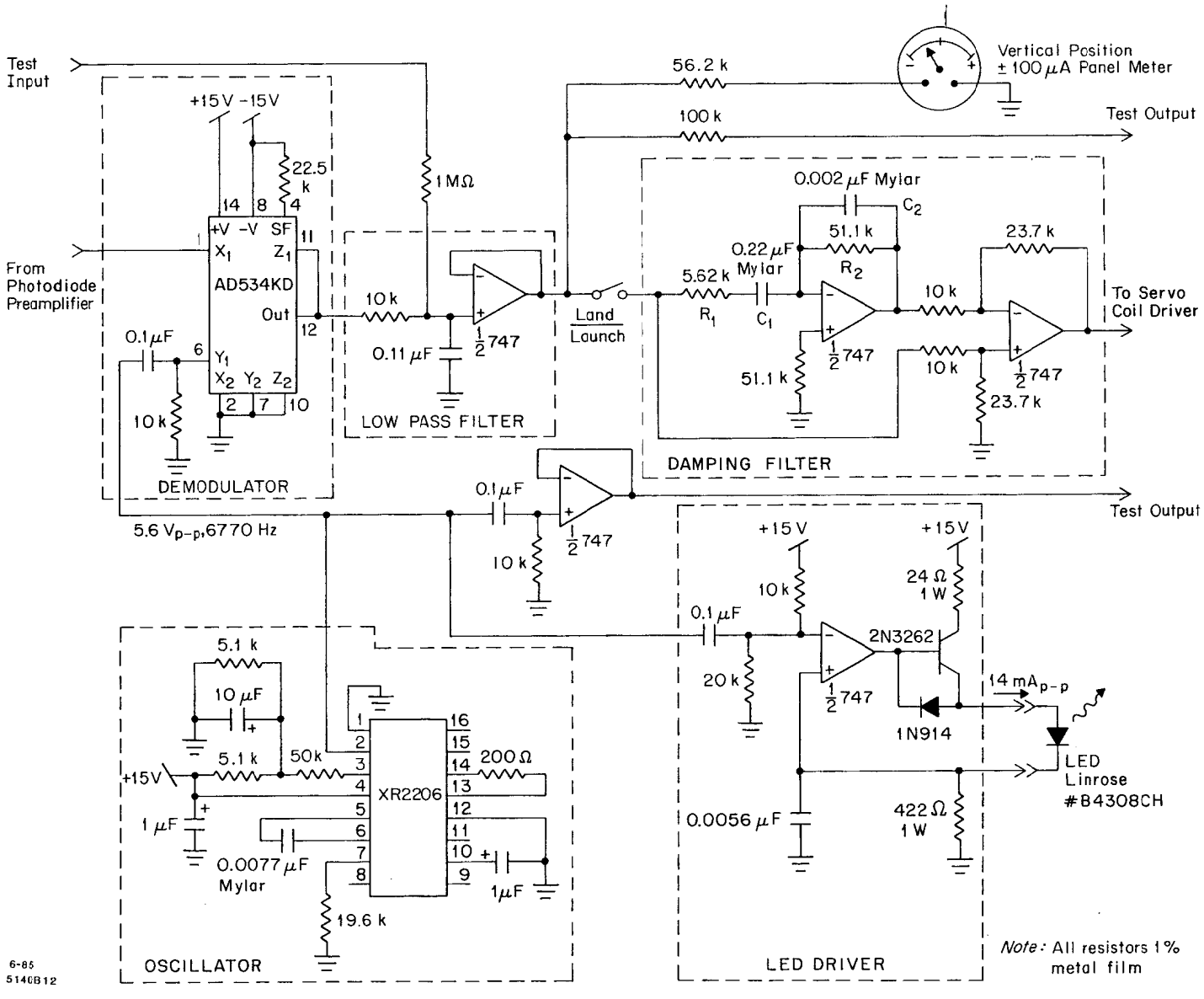

Figure 6.9. Demodulator, Filters, Oscillator, LED Driver

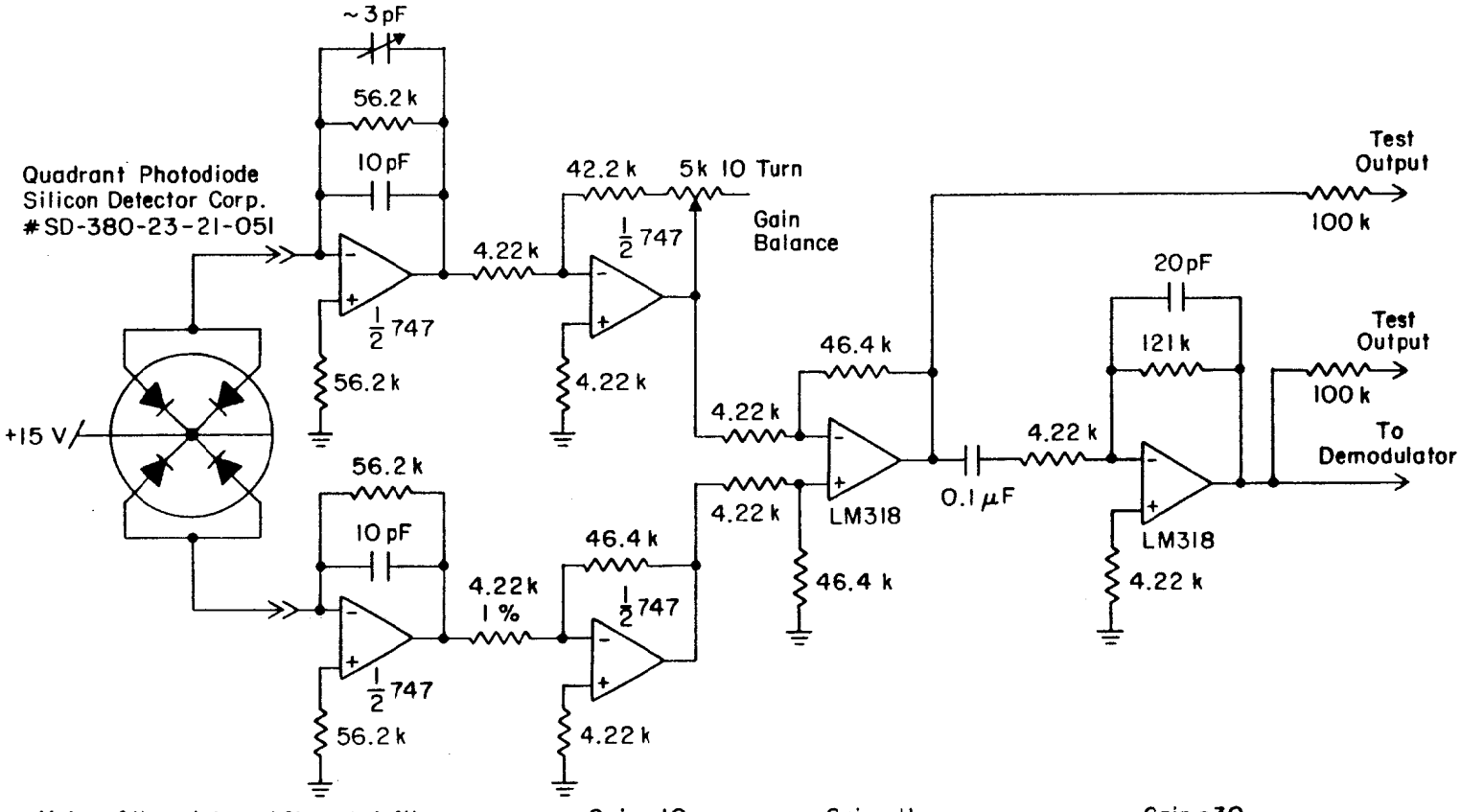

Figure 6.10. Photodiode Preamplifier

conventional preamplifier follows the photodiode. The transfer function of the entire photodiode preamplifier may be described by the transresistance $r = 185\,\mathrm{M}\Omega$. A small trim capacitor in the first stage is necessary to equalize the phase shift in the two channels; otherwise an out of phase component which cannot be nulled by the difference amplifier (3^{rd} stage) will saturate later stages.

The 6770 Hz output of the photodiode preamp is demodulated by an AD534KD (Analog Devices) analog multiplier chip. The dc output is low pass filtered to remove residual carrier and its harmonics. At this point in the loop the voltage gives a direct measure of the rotor position with a sensitivity of $2\,\mathrm{mV}/\mu\mathrm{m}$. The frequency response at this point is flat from dc to 145 Hz, the low pass filter's 3 dB point.

To make the loop damped a signal proportional to the velocity must be added in; this is done by the damping filter. Its frequency response is indicated in Fig. 6.8.

The servo coil is driven by a Kepko model BOP 36-5M bipolar power operational amplifier which can deliver 5 Amps at 36 Volts. The peculiar feedback arrangement shown is required by the internal components; it provides a forward transconductance (current out/voltage in) of .51 mho. The total dc gain of the servo loop to this point is called β and has the measured value

$$\beta = 2.4\,\mathrm{mA}/\mu\mathrm{m}. \tag{6.3}$$

The frequency response of the coil driver is flat from dc to 140 Hz where the gain begins to roll off because of the inductance of the servo coil.

The parameters of the servo coil, given in Fig. 6.8, are chosen to satisfy several criteria. The resistance should be a good match to the output impedance of the driver, the inductance should be low enough for sufficient bandwidth, and the magnetic field that can be generated should be enough to provide a large stable region. The force applied by the coil to the rotor per unit current flowing through it will be called B. A simple estimate made in the design phase indicated that the coil would provide a force of

$$B = 40\,\text{dyne/mA} \qquad \text{(design estimate)}. \tag{6.4}$$

Thus the peak force would be $\sim 40\,\text{dyne/mA} \cdot 5\,\text{A} \sim 2 \cdot 10^5\,\text{dyne}$, implying a stable region of 1 cm since the magnet force gradient A is $\sim 2 \cdot 10^5\,\text{dyne/cm}$. We will show below how the parameter B is measured in the completed device and will also show that the 140 Hz bandwidth limit due to the coil inductance is tolerable.

In operation the system is adjusted so that the rotor floats about 100 μm above the magnetic neutral point (where gravity and the permanent magnet force are in equilibrium) so the servo coil is pushing slightly down on the rotor. This insures that when the land/launch switch (see Fig. 6.9) is opened the rotor will move up and stop against the brass touchdown plate (see Fig. 6.1) that forms the uppermost surface of the vacuum volume. The rotor will launch again when the switch is closed even if the landed position is as much as a few mm above the launched position. When the rotor is floating a dc current of about 240 mA flows in the servo coil leading to a power dissipation of about 500 mW, low enough so that no cooling

system is required. In this respect the design is an improvement over earlier ones by Beams in which there was no permanent magnet and so the servo coil had to support the full weight of the rotor. In those designs power dissipation was much higher.

If we ignore the finite bandwidth of the various elements in the servo loop, then the stability of the system may be discussed very simply. As long as the electronically generated spring constant βB (=force applied by servo coil per unit displacement of rotor) is stronger than the anti-spring constant, $-A$, due to the permanent magnet, the rotor will be confined in a harmonic potential and execute simple harmonic oscillations at the frequency

$$\omega_z = \left(\frac{k_z}{m}\right)^{1/2}, \tag{6.5}$$

where m is the rotor mass and k_z is the net spring constant $k_z \equiv (\beta B - A)$. The addition of any amount of derivative signal will damp the motion.

In practice each element of the loop has finite bandwidth and will therefore cause lagging phase shifts which may make the system unstable. To study the system we will imagine that the servo loop is broken. Suppose that there are two rotors; one has vertical coordinate z and its position is measured by the photodiode and thus controls the coil current. This rotor's position is not governed by magnetic forces but may be controlled at will. The other rotor has vertical coordinate z' and it is acted upon by the magnet, the coil, and gravity. When the first rotor is at $z = 0$ the coil current generated is zero, and when the second is at $z' = 0$ the permanent

magnet force and gravity are in equilibrium. The open loop transfer function will relate z and z'.

The electronic part of the transfer function $T(\omega)$ relates z to the coil current i

$$i = z \cdot T(\omega). \tag{6.6}$$

Using the $e^{+j\omega t}$ time dependence convention ($j = \sqrt{-1}$) it is given by

$$T(\omega) = \beta \left(\frac{\omega_1}{\omega_1 + j\omega}\right) \left(1 + \frac{j\omega}{\omega_d} \cdot \frac{\omega_2}{\omega_2 + j\omega} \cdot \frac{\omega_3}{\omega_3 + j\omega}\right) \left(\frac{\omega_4}{\omega_4 + j\omega}\right). \tag{6.7}$$

The parameters are all easily measured:

$$\begin{aligned} \beta &= 2.4 \cdot 10^4 \,\mathrm{mA/cm}, \\ \omega_1 &= 2\pi \cdot 145 \,\mathrm{Hz}, \\ \omega_2 &= 2\pi \cdot 1560 \,\mathrm{Hz} = 1/R_2C_2, \\ \omega_3 &= 2\pi \cdot 130 \,\mathrm{Hz} = 1/R_1C_1, \\ \omega_d &= 2\pi \cdot 14 \,\mathrm{Hz} = 1/R_2C_1, \\ \omega_4 &= 2\pi \cdot 140 \,\mathrm{Hz}. \end{aligned} \tag{6.8}$$

β is the electronic gain at dc; the other three factors in T are all equal to 1 at dc. The first factor containing ω_1 is the transfer function of the lowpass filter. The next factor is the damping filter. $1/\omega_d$ is the differentiating time constant and ω_2 and ω_3 are finite to keep the differentiator stable. (See the schematic Fig. 6.9 for definitions of R_1, *etc.*) The final factor is the transfer function of the servo coil

driver and would not be present if the coil inductance were zero. There are of course other poles at much higher frequencies that are not included in $T(\omega)$, but these are irrelevant.

To write the full open loop transfer function we need the equation of motion of the coordinate z':

$$Az' - Bi = -m\omega^2 z'. \tag{6.9}$$

The first term on the left side is the magnet force (upwards for an upwards displacement of z') and the second term is the force due to the coil (downwards for an upwards displacement of z). The right side is the mass times the acceleration. The open loop transfer function is defined by

$$z' = z \cdot R(\omega), \tag{6.10}$$

and may be obtained by combining the previous four expressions

$$R(\omega) = g\left(\frac{\omega_m^2}{\omega_m^2+\omega^2}\right)\left(\frac{\omega_1}{\omega_1+j\omega}\right)\left(1+\frac{j\omega}{\omega_d}\cdot\frac{\omega_2}{\omega_2+j\omega}\cdot\frac{\omega_3}{\omega_3+j\omega}\right)\left(\frac{\omega_4}{\omega_4+j\omega}\right), \tag{6.11}$$

where we define the new parameters in terms of the old:

$$\begin{aligned} g &\equiv \beta B/A, \\ \omega_m^2 &\equiv A/m. \end{aligned} \tag{6.12}$$

g is the open loop gain at dc and is simply the ratio of the electronically generated spring constant to the permanent magnet anti-spring constant. ω_m is the resonant

frequency that the rotor mass would have with the permanent magnet spring constant if it were positive. From Eqn. 6.5 we also have

$$\omega_z^2 = \omega_m^2(g-1). \tag{6.13}$$

Both ω_z and g are easily measured in the actual device closed loop. ω_z is the resonant frequency and may be observed with the loop lightly damped, while g may be measured by injecting a signal into the loop. We find:

$$\begin{aligned} \omega_z &= 2\pi \cdot 11.1\,\text{Hz}, \\ g &= 2.0\,. \end{aligned} \tag{6.14}$$

Knowing these we may use the above expressions to calculate ω_m, A, and B:

$$\begin{aligned} \omega_m &= 2\pi \cdot 11.1\,\text{Hz}, \\ A &= 2.7 \cdot 10^5\,\text{dyne/cm}, \\ B &= 23\,\text{dyne/mA} \qquad \text{(measured)}. \end{aligned} \tag{6.15}$$

The value obtained in this way for A is in good agreement with the data in Fig. 6.7, while the value for B agrees roughly with the design estimate.

To investigate the stability of the system we close the loop by setting $z = z'$. The characteristic function is then given by

$$C(\omega) \equiv 1 - R(\omega). \tag{6.16}$$

If $C(\omega)$ has no zeros in the lower half plane then the system will be stable. A way to check this is to make a Nyquist plot, a plot of $-R(\omega)$ in the complex plane as ω runs around a contour that goes from 0 to $+\infty$ along the real axis, closes around the lower half plane, and then goes from $-\infty$ to 0 along the real axis. The Nyquist plot is useful because the number of times the curve loops around the point $(-1,0)$ (clockwise considered positive) counts the number of zeros minus the number of poles of $C(\omega)$ in the lower half plane. For our example we can see by inspection that $R(\omega)$ (and therefore $C(\omega)$) has one pole in the lower half plane; it is at $\omega = -j\omega_m$. The Nyquist plot (using measured values for the parameters) is given by the solid line in Fig. 6.11. Since the curve loops around the point $(-1,0)$ minus one times, we may conclude that there are no zeros in the lower half plane and the system is stable. The phase margin is seen to be about 30° and the gain could evidently be increased by a factor of four or decreased by a factor of two before the system would become unstable. The dotted line shows the Nyquist plot if $\omega_1, \omega_2, \omega_3, \omega_4 = \infty$, as would be the case if all the elements in the loop had infinite bandwidth.

6.3 Rotor

A mechanical drawing of the rotor is given in Fig. 6.12. The Rexolite 1422 polystyrene* body was fabricated in three steps. First the inside was drilled and bored to size on a lathe. Then the part was removed from the lathe, the hole

* Material manufactured by C-LEC Plastics, 1717 Bridgeborough Road, Beverley NJ 08010.

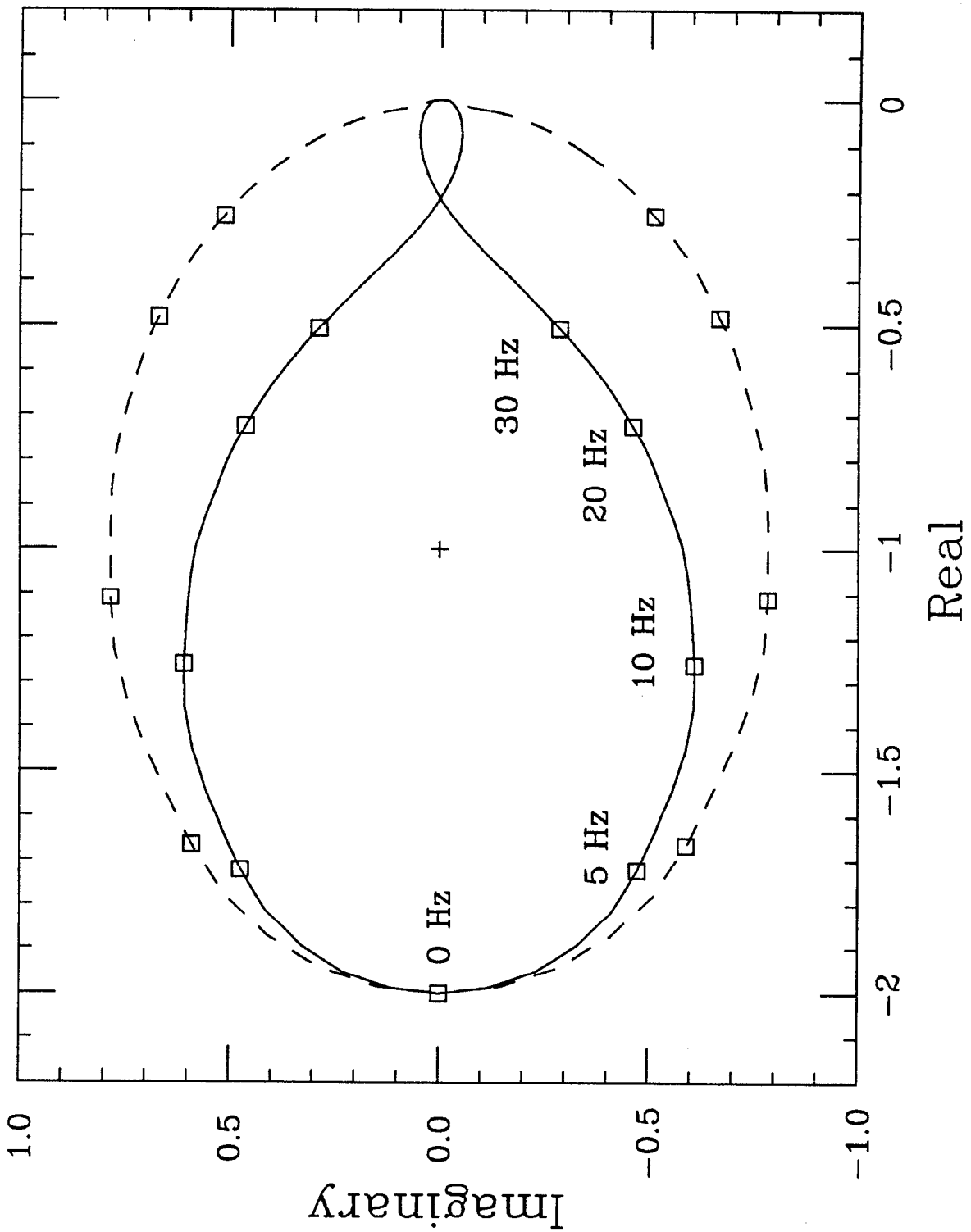

Figure 6.11. Nyquist Plot

for the armature was drilled, and an aluminum mandrel was made to fit the bore. Finally the part was mounted on the mandrel and the outside was turned to size. The alloy 4750 nickel iron* armature and bearing pieces were cemented into the rotor body with a small amount of epoxy while the body was still on the lathe. This made it possible to check the concentricity and roundness of the assembly—no dimension was out by more than 15 μm. The polystyrene cap that covers the bottom of the rotor had to be glued on after removing the body from the lathe. A 50 μm interference fit was used to ensure good centering.

The copper metalization was applied to the rotor body using printed circuit board fabrication techniques. First the outer surface of the plastic body was roughened slightly by wet honing with cerium oxide to ensure good adhesion of the copper†. Then the whole outer surface was electroless plated with copper to a thickness of 5 μm. A photomask was prepared according to the metalization pattern shown in Fig. 6.12. The rotor was dipped in a positive acting photoresist‡, wrapped in the photomask, and exposed to ultraviolet light. After the resist was the developed§ the unwanted copper was etched off in a chrom-sulfuric bath. The positive acting process was chosen because after the etching step is completed the

* Material obtained from AeroMet Inc., 41 Smith Street, Englewood NJ 07631.

† We thank Jim Pope of the SLAC plating shop for his help with the electroless plating.

‡ 35 parts KTI 1350 and 25 parts acetone. Resist obtained from KTI Chemicals Inc., 1170 Sonora Court, Sunnyvale CA 94086.

§ KTI 351 developer was used.

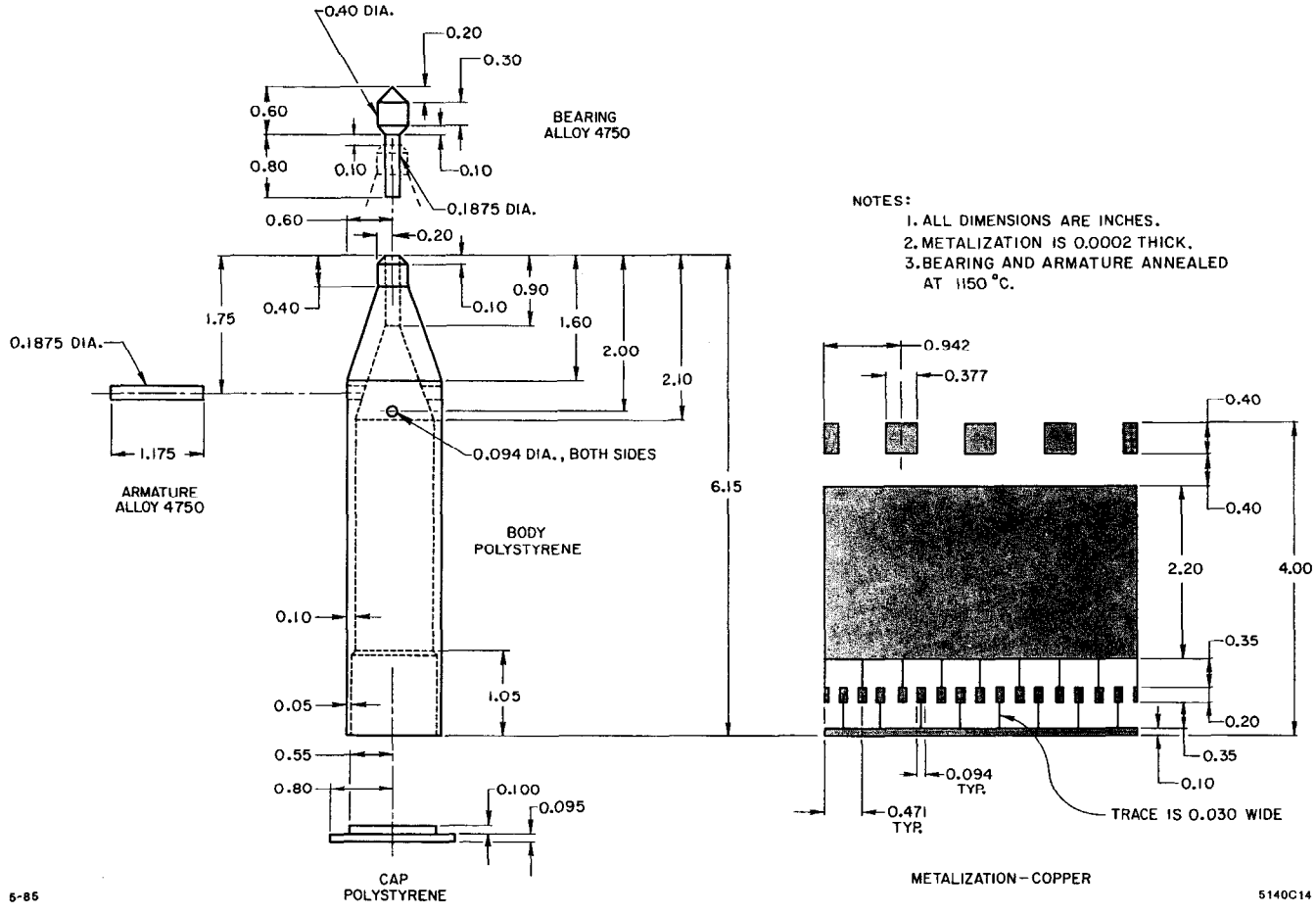

Figure 6.12. Mechanical Drawing of the Rotor

remaining resist may be removed in a weak alkali solution that does not damage the polystyrene surface. Negative acting processes require an organic solvent to remove the photoresist.

Because polystyrene is an excellent insulator, some means must be provided to discharge the isolated metallic parts of the rotor. For this purpose a thin line of resistive ink (52) (visible in Fig. 6.4) connects the bearing, the four tachometer squares, the ground capacitor, and one of the signal pads to an adjacent ground pad. The resistors are each about $10^{11}\,\Omega$, high enough to make their Johnson noise negligible. When the rotor is landed, the point of the bearing piece rests against the brass touchdown plate that forms the uppermost surface of the vacuum volume. The connected metal parts of the rotor may then be set to any desired potential by launching the rotor with the brass plate set at that potential.

The various performance requirements which have led to the present design of the rotor will be discussed in the following chapters.

6.4 Rotor Drive

Torque for spin-up and spin-down is provided by a simple reluctance motor. The system block diagram Fig. 6.3 shows the components of the motor and Fig. 6.13 gives details of the electronics. The placement of the drive coils is shown in Fig. 6.6. Torque is applied to the armature by a unipolar magnetic field switched on and off twice per complete revolution of the rotor. The drive coils that generate the magnetic field are driven by a power MOSFET switch operating at a 50% duty cycle. The switching signal is derived from a photoelectric tachometer that watches

four reflective copper pads on the rotor. The tachometer LED and photodiode are mounted on a ring concentric with the rotor axis that may be rotated to adjust the drive phase.

To estimate the torque that the arrangement will provide we may use a formula for the torque on a prolate spheroid of high permeability in a uniform magnetic field (58)

$$N = \frac{2}{3}\pi m^2 n B^2 \left(\frac{(n/m)^2}{\ln(2n/m)} - 2 \right) \sin 2\alpha, \tag{6.17}$$

where n and m are the semimajor and semiminor axes, B is the applied magnetic field, and α is the angle between the major axis and the applied field. The expression is in the gaussian cgs system. The magnetic field B at the armature may be estimated from

$$B = 2t \cdot I \cdot \frac{2\pi}{c} \cdot \frac{r^2}{(r^2 + z^2)^{1/2}}, \tag{6.18}$$

where the leading factor of two is because there are two drive coils, t is the number of turns per coil, I is the current in each coil (statamps), c is the speed of light (cm/sec), r is the mean radius of the coil turns, and z is the distance from the center of the coils to the rotation axis.

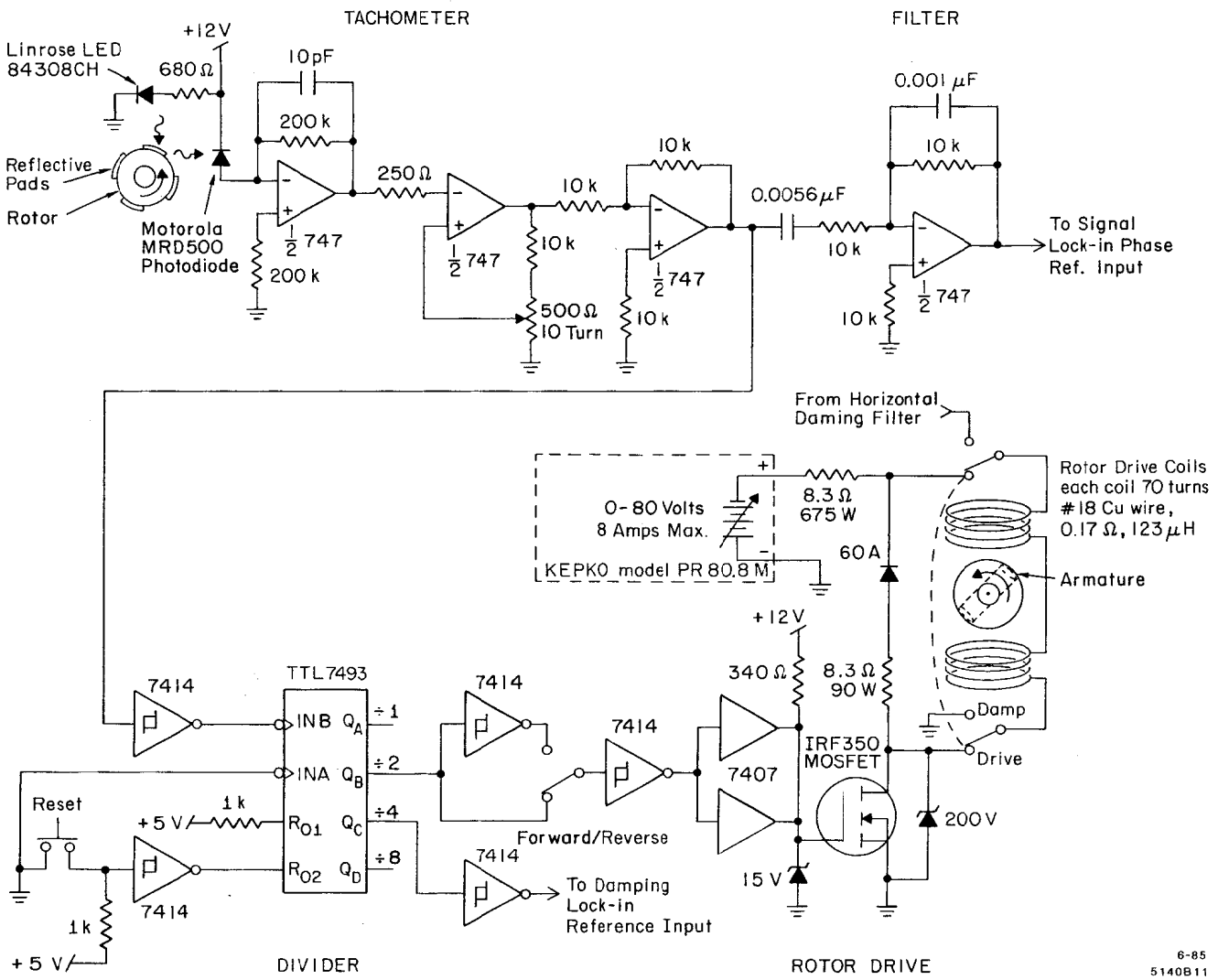

Figure 6.13. Rotor Drive Electronics

With the parameters:

$$\begin{aligned} m &= .25\,\text{cm}, \\ n &= 1.5\,\text{cm}, \\ t &= 70, \\ I &= 8\,\text{A} \cdot 3 \cdot 10^9\,\text{statamp/A}, \\ r &= 1.5\,\text{cm}, \\ z &= 3.0\,\text{cm}, \end{aligned} \tag{6.19}$$

one finds that the peak torque (at $\alpha = \pi/4$) is 4330 dyne $\cdot$ cm. The mean torque is equal to the peak torque divided by π so that the average acceleration is given by

$$\ddot{\theta} = \frac{N_{peak}}{\pi}\frac{1}{I_z}, \tag{6.20}$$

where I_z is the moment of inertia of the rotor about the spin axis, equal to 70 g$\cdot$cm^2. The estimated acceleration is thus

$$\ddot{\theta} = 2\pi \cdot 3\,\text{Hz/sec}, \tag{6.21}$$

about three times higher than the observed acceleration of 1 Hz/sec. This level of understanding has been sufficient so far.

In operation the drive torque may be adjusted by changing the voltage of the rotor drive power supply (see Fig. 6.13). At full power the rotor will go from 0 to 900 Hz in about 16 minutes, and may be spun back down in the same amount of

time. The drive electronics are dc coupled throughout so that the motor will work at very low speeds and may be used to bring the rotor to a dead stop.

6.5 Coupling Capacitors

The coupling capacitors are visible in the close-up photograph Fig. 6.5. Figure 6.1 shows how the rotor fits into the stationary halves of the capacitors. The stationary halves were machined from aluminum and then electroplated with copper so that their surfaces would match those of the rotor.

The gap of the signal coupling capacitor is set to 1.0 mm and it is 20.3 mm in radius. Using the parallel plate approximation we may calculate the signal coupling capacitance

$$C_{SC} = 11.4\,\text{pF}. \tag{6.22}$$

The ground capacitor has a larger gap of 2.2 mm to allow for the swinging of the rotor that occurs as it goes through its 2 Hz pendulum mode during spin-up. Its length is 48 mm and its inside radius is 15.2 mm. Again using the parallel plate approximation one finds

$$C_{GC} = 18.5\,\text{pF}. \tag{6.23}$$

Some of the electrostatic inefficiency of the instrument is due to the finite values of the coupling capacitors. This will be discussed in chapter 7.

6.6 Preamplifier and Signal Processing

Figure 6.14 is a schematic of the low noise preamplifier. The main design goal here is to ensure that no significant noise is contributed from any source other than

the first stage JFET.

As has been mentioned, the 2N3686 JFET first stage is mounted inside the vacuum just beneath the signal coupling capacitor. The drain and source leads come through a feedthrough in the vacuum wall and into an electrostatically shielded box that encloses the preamplifier circuitry. A separate shielded box houses the two 12 V lead-acid batteries which power the preamplifier. Shielded cable connects the battery box to the preamplifier so that the battery box, the preamplifier enclosure, and the vacuum chamber together form an unbroken electrostatic shield. this arrangement is very convenient (the batteries last $\sim$ 1 year between charging cycles) and eliminates problems with noise coupled in from the 120 V ac utility.

Two supply regulators are used. A low noise FET regulator supplies the first two stages of the preamplifier. Its voltage reference is a zener diode which is low pass filtered to reduce noise. Measurements at 7.2 kHz of this regulator's output noise indicate that it may be represented by a series $4\,\mathrm{nV}/\sqrt{\mathrm{Hz}}$ voltage generator. The second voltage regulator was added to isolate the third stage when it was found that the LF356 op-amp impressed noise onto its supply.

With the feedback disconnected the measured voltage gain of the first stage is 30, which implies that the forward transconductance g_{fs} of the FET is $30/R_D \sim$ 2 mmho. The second and third stages together have a voltage gain of 1500 (from 2 kHz to 16 kHz) so the open loop gain is 45000, and since the feedback attenuation factor is 100 the closed loop gain is 100 while the loop gain is 450.

An analysis will be given in chapter 7 which shows that the amount of feedback

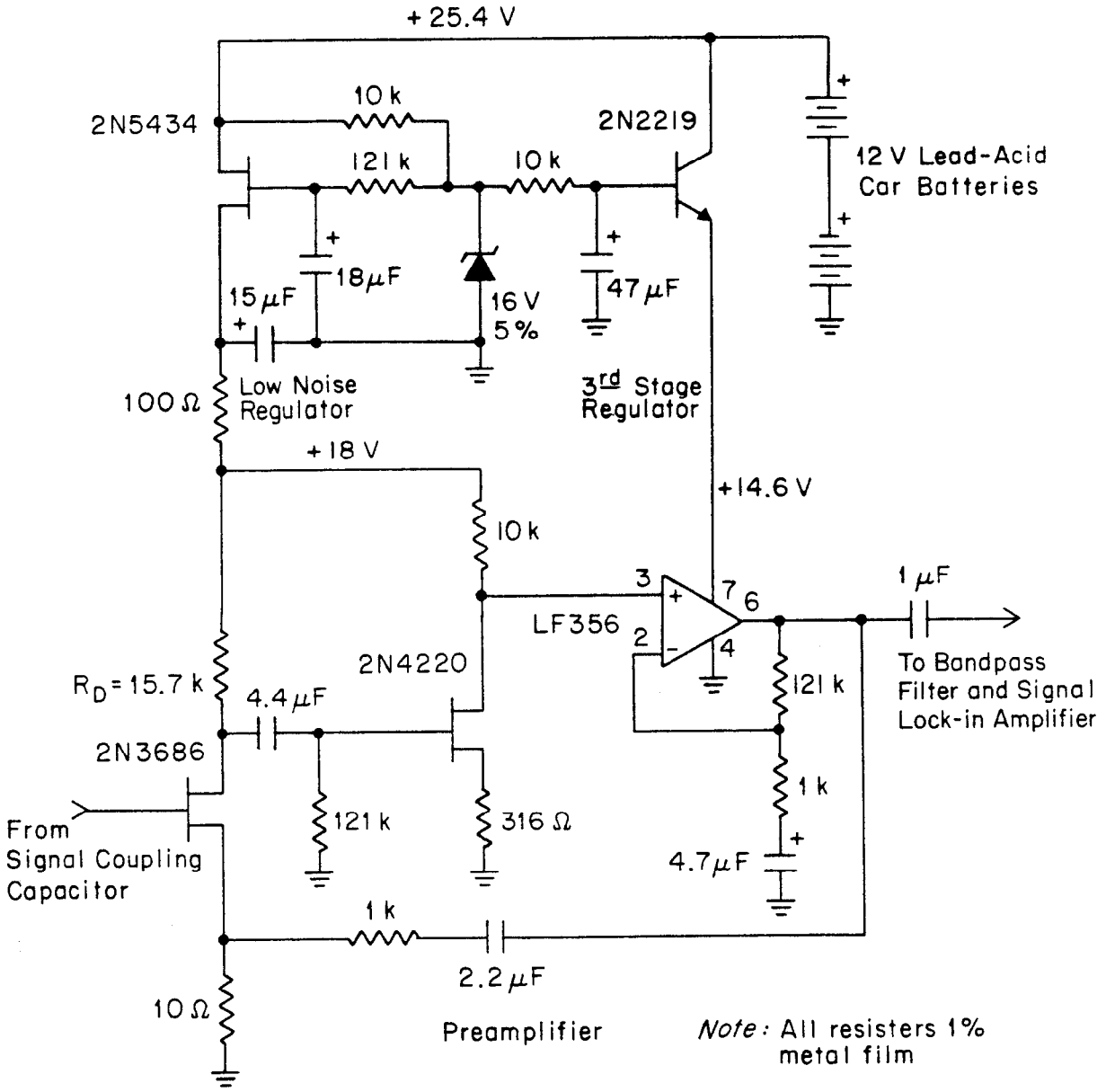

Figure 6.14. Preamplifier Schematic

and the size of the drain resistor have no effect on the signal to noise ratio *assuming* that all noise sources outside the FET are negligible and providing, of course, that the dc operating point of the FET is maintained. Here we will show that noise sources outside the FET are indeed negligible.

This is most convincingly done by measurement. By observing the output noise with the first stage FET removed, we find that the total noise of the later stages, referred to the input of the second stage, is less than $5\,\mathrm{nV}/\sqrt{\mathrm{Hz}}$ from 2 kHz to 16 kHz. When referred to the input of the preamplifier by dividing by the first stage voltage gain this gives a contribution of $.17\,\mathrm{nV}/\sqrt{\mathrm{Hz}}$. The $4\,\mathrm{nV}/\sqrt{\mathrm{Hz}}$ supply noise and the $15.7\,\mathrm{nV}/\sqrt{\mathrm{Hz}}$ Johnson noise of R_D are not included in this. Since the FET output impedance is high ($\sim 100\,\mathrm{k}\Omega$) their full values are seen at the second stage input, giving $.13\,\mathrm{nV}/\sqrt{\mathrm{Hz}}$ and $.52\,\mathrm{nV}/\sqrt{\mathrm{Hz}}$ contributions when referred to the input. The only other amplifier noise source outside of the first stage FET is the Johnson noise of the $10\,\Omega$ source resistor. This is already at the input and gives a $.4\,\mathrm{nV}/\sqrt{\mathrm{Hz}}$ contribution. Summing these sources (incoherently) we find that the total noise from outside the first stage, when referred to the preamplifier input, amounts to $.69\,\mathrm{nV}/\sqrt{\mathrm{Hz}}$. This is totally negligible compared to the $8.3\,\mathrm{nV}/\sqrt{\mathrm{Hz}}$ first stage FET noise.

The first stage FET, a 2N3686, was chosen because it gave the best signal to noise ratio of those devices tried. About 25 devices were tried in all, of types 2N3686, 2N4416, 2N4417, and 2N4220. Several devices were found that were as good as the chosen one, some of type 2N4416 and some of type 2N3686. These

types were selected for trial because they have small input capacitances ($1 - 3\,\mathrm{pF}$) and so are expected to be well matched to our source capacitance ($\sim 3\,\mathrm{pF}$). A general discussion of the noise matching problem and its effect on the signal to noise ratio, along with a complete characterization of the noise properties of the chosen FET will be given in chapter 7. Briefly, the total noise at 7.2 kHz with a 2.8 pF dummy load is $8.3\,\mathrm{nV}/\sqrt{\mathrm{Hz}}$, and the measured amplifier input capacitance is 1.5 pF. An optimally matched FET would be three times smaller, but no high quality smaller devices seem to be available.

The first stage biasing arrangement used in the amplifier is a bit unusual and deserves comment. With the supply voltage at 18.0 V and $R_D = 15.7\,\mathrm{k}\Omega$, and with $V_{GS} = 0$ (gate to source voltage), the measured V_{DS} (drain to source voltage) is 4.3 V. This implies a drain current of about .9 mA, and puts the FET at its most quiet operating point. The value of V_{DS} is not critical, but it is important to maintain $V_{GS} \sim 0$. We find that no bias resistor on the gate is needed to ensure this. With a signal source such as ours, which injects no dc leakage current into the preamplifier whatsoever, it is found that the FET gate will "autobias" at $V_{GS} = 0$. If very large signals are applied to the input the circuit can occasionally get stuck with the gate very negative and the channel turned off, but this may be easily cured by grounding the input, and is a small price to pay for avoiding the gate resistor altogether with its attendant stray capacitance and noise contribution.

Several signal processing components follow the preamplifier, and are shown in the block diagram Fig. 6.3. The bandpass filter is centered at the signal frequency

and has a passband about 1 kHz wide. The filter serves two purposes, to block out the large signal at the 900 Hz rotation frequency, and to remove the amplifier noise at the odd harmonics of the signal frequency. Typical signal amplitudes at 7.2 kHz are about 10 μV rms (referred to the input), while the signal at 900 Hz can be 100 times larger. This causes dynamic range problems in the lock-in and so must be filtered out. The charge measuring signal at 7.2 kHz is nearly sinusiodal. The lock-in, however, demodulates with a square wave and so passes to some extent the odd harmonics of the signal frequency. Unless filtered out these contain amplifier noise but no signal and so will degrade the signal to noise ratio.

The main lock-in amplifier is a Princeton Applied Research model #5402. It can demodulate in two orthogonal phases, which is very useful when neutralizing samples and measuring their motion sensitivities. The phase reference signal for the lock-in comes from the photoelectric tachometer (see Fig. 6.13). The tachometer output which is used for the phase reference is bandpass filtered—this was found to be helpful in reducing the electronic lock-in phase noise, as will be discussed in section 9.2.3.

The lock-in is followed by a 48 dB/octave low pass filter at $\sim$ .5 Hz which provides protection against aliasing at the 1 Hz sampling rate usually used. A gain of 10 is included here to match the $\pm$1 V output of the lock-in to the $\pm$10 V input range of the ADC. The 17 bit ADC is interfaced to an LSI-11 computer. This computer is used only for data logging and for pulsing the ultraviolet light. For analysis, data is transferred to the laboratory's IBM mainframe system, where

programs have been developed to do spectral analysis and filtering.

The whole signal analysis system may be checked for its noise contribution by putting a dummy load on the preamplifier input and recording the resulting noise at the computer. No contribution above the preamplifier noise is seen and in this way one may be sure that the lock-in input noise, noise of the filters, digitizing noise, *etc.*, all make negligible contributions to the total noise.

6.7 Active Horizontal Damping

As will be discussed in section 8.3 on the rotor gyrodynamics, the slow (6 second period) gravitational precession of the rotor is not well damped by the viscous oil. The observed natural decay time in this mode of several hours would be a great inconvenience, since the mode is excited to an amplitude of $\sim 100\,\mu$m at spin-up and one would have to wait for it to decay before making measurements. Consequently an active damping system has been added; its components are shown in the block diagram Fig. 6.3.

To explain how the active horizontal damping works, it will be necessary to explain how it is that surface potentials are thought to generate the 900 Hz signal seen at the preamplifier input. It is found by measurements that the surface potential variations at different points on metal surfaces such as those used for the coupling capacitors are of order $10 - 100\,$mV*. The coupling capacitors should thus be modeled as a capacitor with a voltage source in series, where the voltage

* Early in the project we built an instrument with which we could measure the potential at the surface of a spinning aluminum disk. The observations

is equal to the mean potential measured across the capacitor gap. When the rotor spins, because of mechanical imperfections, the capacitance varies slightly, but more importantly the mean potential across the gap varies so that the voltage generator becomes time dependent. A crude estimate for the signal size may be made by setting it equal to the magnitude of surface potential variations times $\delta g/g$, where δg is the typical mechanical inaccuracy (eccentricity for example), and g is the capacitor gap. Taking δg to be $20\,\mu$m and g to be 1 mm we predict the signal amplitude to be in the range $200\,\mu$V to 2 mV. In practice we find an rms signal of $400\,\mu$V to 1 mV, with changes in the amplitude occurring whenever the rotor is handled.

It is found that the amplitude and phase of the 900 Hz signal depends on the rotor position. The motion sensitivity may easily be measured by using the three axis translation stage from which the suspension magnet hangs to translate the rotor could be crudely characterized by a flat spectrum of magnitude $100\,\mathrm{mV}/\sqrt{\mathrm{cm}^{-1}}$ for wavelengths of order 1 cm. We also looked at several other kinds of metal surfaces with a Kelvin probe and obtained similar results. No direct measurements of electroplated copper surfaces have been made, but since the surface potential signals in model III are similar to those in earlier devices, it seems that copper is like aluminum, despite the fact that its oxide is conducting while aluminum's is insulating. The Fourier amplitudes over an interval equal to the 9 cm rotor circumference are what matter for generation of the 900 Hz signal, this would be $100\,\mathrm{mV}/\sqrt{\mathrm{cm}^{-1}} \cdot 1/\sqrt{9\mathrm{cm}} \sim 30\,\mathrm{mV}$.

a known amount. For motion in each of the three directions the motion sensitivity is found to be about $1\,\mu V/\mu m$ (referred to the amplifier input). Since the amplifier noise at 900 Hz is about $20\,nV/\sqrt{Hz}$, the amplitude of the 900 Hz signal gives a measure of the rotor position with a noise of about $20\,nm/\sqrt{Hz}$. The measured value of the motion sensitivity at 900 Hz may be crudely understood by noting that it is equal to 1 mV/mm, which is the signal amplitude divided by the capacitor gap.

A separate lock-in is used to demodulate the 900 Hz signal. It is found that various phase settings of the lock-in correspond to measuring the component of the horizontal motion along various directions. The output of the lock-in is sent through a differentiating filter with a gain of 3 at .1 Hz, and is then applied through a 500 Ω resistor to the drive coils. The lock-in is set for a voltage gain of 40 and a bandwidth of 1 Hz. The net result is that a small current proportional to the rotor's horizontal velocity (about $2\,\mu A/(\mu m/sec)$) is applied to the rotor drive coils. This current generates a magnetic field which applies a small torque to the induced magnetic moment of the rotor bearing piece. With the phase set correctly the precession is then damped with a 10 minute time constant. The gains have been arrived at by trial since no quantitative description of the damping force has been developed.

6.8 Samples and Related Parts

In chapter 9 it will be shown how samples of the sort depicted in Fig. 6.15 are used to measure the charge resolution of the instrument. The method is to average the output of the instrument for a time T, eject a few photoelectrons from the sample by shining a brief burst of ultraviolet light at it, and then average again for a time

T. The difference of the two averages measures the change of the sample charge. The experiment is repeated many times and the charge changes are histogrammed. Peaks appear in the histogram at charge changes equal to integer multiples of the electron's charge. The widths of the peaks measure the charge resolution of the instrument, while their spacing provides a calibration of the instrument in terms of the electron's charge.

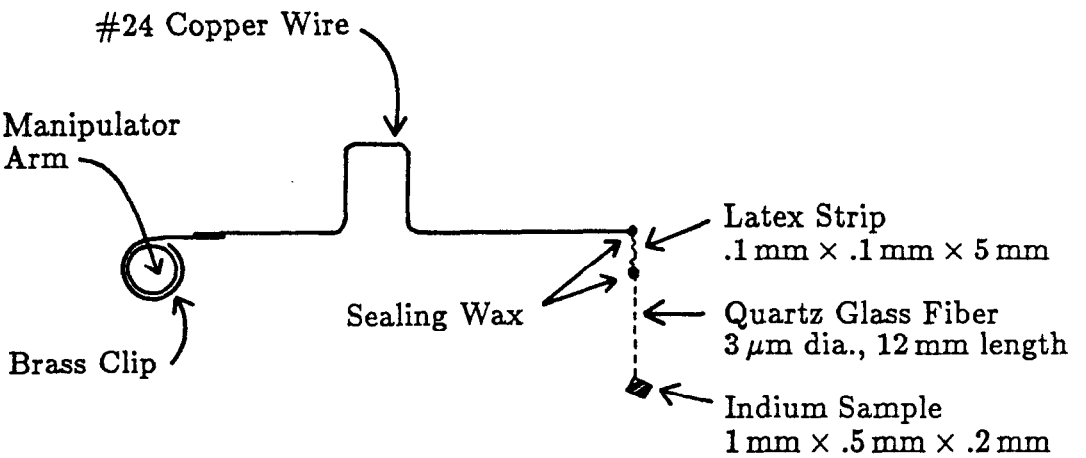

Figure 6.15. Test Sample

The test sample is made from .1 mm thick indium foil which is folded in half and pinched onto a quartz glass fiber. Indium is chosen because it sticks to the glass fiber, eliminating the need for an adhesive.

The quartz glass fibers are fabricated and handled according to the methods

described by Strong (59). An oxygen-hydrogen torch is used for cleanliness and the fibers are made only as needed so that their surfaces are exposed to air for no more than one hour before they are installed in the apparatus. The fiber surfaces are never touched or cleaned.

The top end of the glass fiber is attached to a short strip of latex rubber with a drop of sealing wax. The latex damps the motions of the sample (which have very long time constants otherwise) but is a poor solution to the damping problem because if stretched the strip can take hours to relax back to its original length. No better solution has been found which fits into the space available. Several variations on the sample design shown in Fig. 6.15 have also been tried. These will be discussed in chapter 9.

The sample manipulator arm enters the vacuum chamber through a stainless steel bellows and is attached to a two axis translation stage outside the chamber. This allows calibrated motions of the sample in the vertical and radial directions.

The ultraviolet light source is a 12 V quartz halogen lamp*. It is controlled by the data logging computer through a power MOSFET switch. Two pinholes collimate the light and a small aluminized mirror on an adjustable mount deflects the beam into the vacuum chamber through a quartz glass window. The illuminated spot on the sample is about .5 mm in diameter. The pulse duration required to give a certain mean charge change is found by experiment.

A probe is included in the instrument for rough neutralization of the sample.

* Part #1220 from Sunnex Inc., 87 Crescent Road, Needham Mass. 02194.

In Fig. 6.5 the probe is retracted and is visible behind the signal coupling capacitor. The probe is electrically isolated from the chamber and connected to an adjustable power supply so that its voltage may be set anywhere in the range +9 V to −9 V. The tip of the probe is a piece of 25 μm diameter gold plated tungsten wire. A sample such as the one described above may be set to any desired charge with a reproducibility of about 5000 q_e. Fine adjustments of the sample charge are made with the ultraviolet light.

6.9 Vacuum System

High vacuum is required to keep the gas drag on the rotor low enough so that data may be taken with the rotor coasting, and so that wind does not blow the sample around. It may also be required to keep the surface resistance of the quartz glass fiber high, but this is not known to be a problem.

The deceleration of the rotor due to gas drag may easily be estimated in the limit where the mean free path is much greater than the capacitor gaps. This is well satisfied since the mean free path for air at 10^{-6} Torr (the highest pressure at which the system is operated) is 50 meters. In this limit

$$\ddot{\theta} = 2\pi \cdot p \cdot \left(\frac{M}{2\pi RT}\right)^{1/2} \cdot \dot{\theta} \cdot \frac{r^3 l}{I_z}, \tag{6.24}$$

where p is the pressure, M is the molecular weight of the residual gas, R is the gas constant for a mole, T is the absolute temperature, and r, l, and I_z are the rotor's radius, length, and z-axis moment of inertia. Setting $M = 28$, $p = 10^{-6}$ Torr =

$1.3 \cdot 10^{-3}$ dyne/cm^2, and $\dot{\theta} = 2\pi \cdot 900$ Hz, one finds $\ddot{\theta} = 2\pi \cdot .30$ Hz/hour, which is exactly the observed deceleration. Actually, the base pressure of the chamber is about $4 \cdot 10^{-7}$ Torr (according to a cold cathode guage) and the composition of the residual gas is unknown (and would effect the guage calibration) so the agreement may be accidental. It is not even known for certain that the observed rotor deceleration is due to gas drag, but the estimate nonetheless shows that it is worthwhile to keep the pressure below 10^{-6} Torr.

The wind force on the sample may be estimated with a similar expression

$$F = p \cdot \left(\frac{M}{2\pi RT}\right)^{1/2} \cdot A \cdot \omega r, \tag{6.25}$$

where A is the sample area equal to about 10^{-2} cm^2. The expression assumes that all surfaces are moving past the sample at the rotor's peripheral velocity, which will lead to an overestimate of the force. At 10^{-6} Torr and $\omega = 2\pi \cdot 900$ Hz one finds $F = 1.5 \cdot 10^{-6}$ dyne. If the sample mass is 10^{-3} g and it is hung from a 1 cm fiber this will cause a constant deflection of 15 nm, which is of no importance.

The vacuum is maintained by a conventional 4 inch oil diffusion pump. The working fluid is Dow Corning DC-704 and a liquid nitrogen cold trap is used between the pump and the chamber to prevent backstreaming. All seals in the system are Buna-N or Viton O-rings.

A 1/2 inch thick, 6 inch diameter, glass viewport is provided on the front cover of the vacuum chamber. Its inner surface was coated with transparent conductive tin oxide according to the directions of Holland (60) to avoid breaking the electrostatic

shield. The 1–3/4 inch O.D., 1–7/16 inch I.D., Pyrex glass tube that houses the upper part of the rotor was similarly coated on the inner surface with tin oxide. The coatings have a resistance of about $10\,k\Omega/\square$.

This completes the basic description of the instrument. The following two chapters provide justification for the design and explain certain aspects of the instrument's behavior.

7. Electronic Design

Issues which bear on the electronic and electrostatic design of the instrument are discussed in this chapter. First, the reason for having eight pairs of signal and ground pads is given and the choice of pad size is explained. Then the electrostatic inefficiencies due to imperfect sample to pad coupling and finite signal and ground coupling capacitances are discussed, and the design of the sample container is considered. Next comes a calculation of the signal to noise ratio in terms of the noise properties of the amplifier. The noise matching problem is considered, and it is explained why N-channel JFETs are the preferred input devices for the instrument. Finally the noise properties of the JFET used in the instrument are given, and the dependence of the signal to noise ratio on the capacitance of the signal source and on the operating frequency is shown.

7.1 Pad Geometry

In section 6.7 on the active horizontal damping it was explained how surface potentials generate the 900 Hz signal, and it was stated that the observed motion sensitivity* of this signal is 1 μV/μm for motions of the rotor relative to the coupling capacitors. It follows then that if the instrument were built with but one signal and one ground pad, since 900 Hz would be the signal frequency as well as the rotation frequency, it would be necessary to hold the rotor fixed to better than

* In this thesis, "motion sensitivity" always means the change in the rms amplitude of some signal per unit translation of something, and is expressed in μV/μm or nV/μm.

$8\,\mathrm{nV}/\sqrt{\mathrm{Hz}} \div 1\,\mu\mathrm{V}/\mu\mathrm{m} = 8\,\mathrm{nm}/\sqrt{\mathrm{Hz}}$ in order that the rotor motion not make a noise contribution larger than the amplifier noise. As this would be very difficult it is better to operate at a harmonic of the rotation frequency where both the amplitude and the motion sensitivity of the surface potential generated signal are much reduced.

Eight was chosen as the harmonic for the charge measuring signal based on earlier experience. Figure 7.1 shows the spectrum of the surface potential generated waveform for the current device (referred to the amplifier input, as always). The data was taken with no sample in the instrument and the measured motion sensitivity of the eighth harmonic was $.5\,\mathrm{nV}/\mu\mathrm{m}$. Since this is just about equal to the best motion sensitivity with the sample installed (the change in signal for motions of the rotor relative to the sample) it seems that eight was a good choice. Note that the signal decreases still further at higher harmonics and so presumably does the motion sensitivity, but one doesn't want to use more pairs of pads than absolutely necessary, since each pair contributes to the total stray capacitance.

Its is worth noting that in Fig. 7.1 the eighth harmonic is in no way peculiar. This makes it clear that the waveform output by the instrument with no sample installed is not produced by the eight-fold pad structure. In model I the situation was different, the signal harmonic (then the sixteenth) was much stronger than its neighbors due to the pad structure being too close to surface potentials of stationary metal parts. In model II and the present design an effort was made to shield the pad structure from stationary metal parts. This is why, for example, the rotating

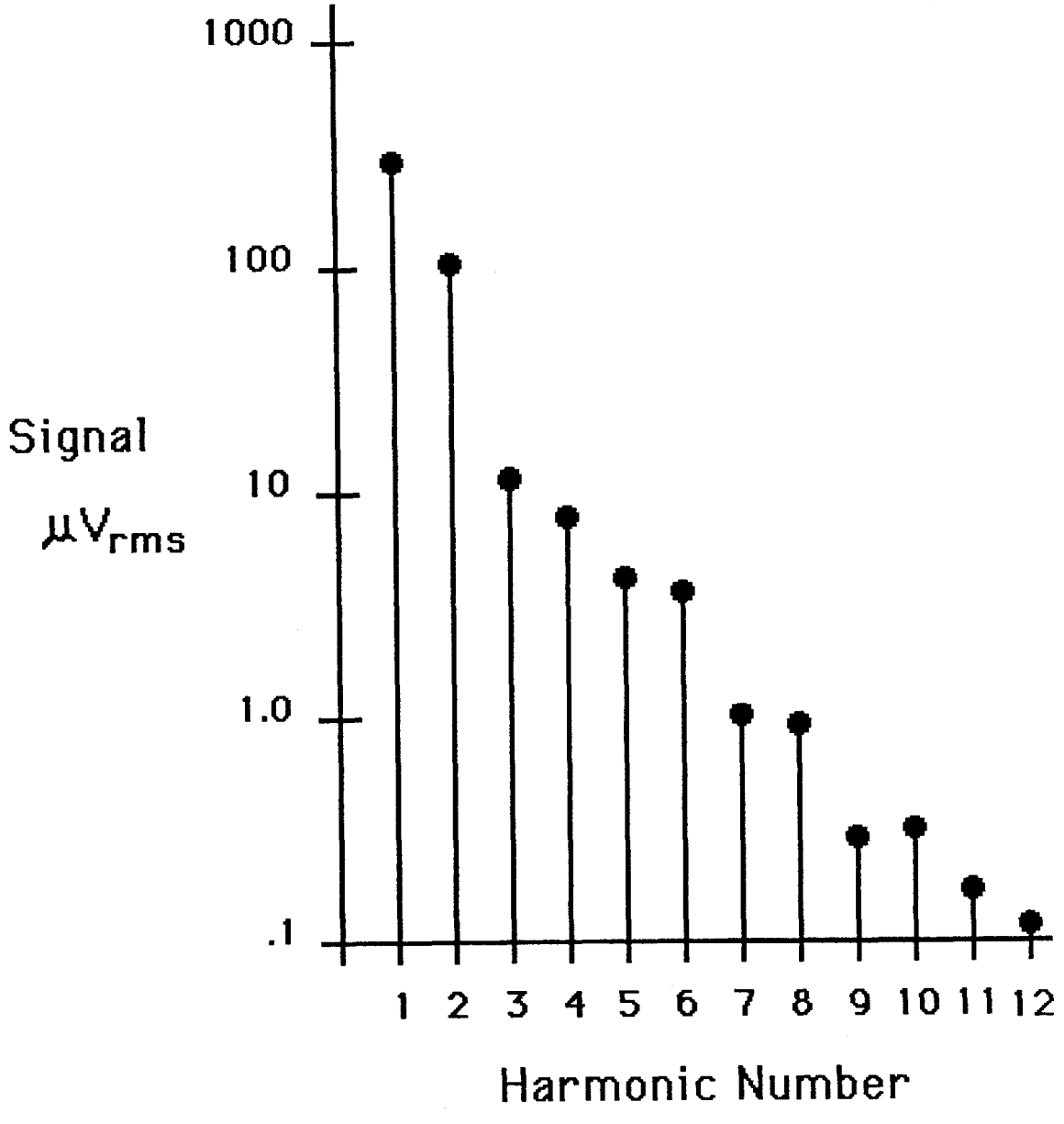

Figure 7.1. Surface Potential Signal. The motion sensitivity at 900 Hz (1st harmonic) is $1\,\mu V/\mu m$ and at 7.2 kHz (8th harmonic) is $.5\,nV/\mu m$. The motion sensitivity at the other harmonics has not been measured.

inner half of the ground capacitor extends well below the outer half, as is visible in Fig. 6.5.

The size of the pads is fixed roughly by the sample size. According to the discussion of chapter 3, an attractive goal seems to be to try to measure samples of $\sim 10\,\mathrm{mg}$ mass, corresponding to a volume of about $1\,\mathrm{mm}^3$ of steel, for example. One might imagine small cylindrical samples about 1 mm in diameter and 1 mm high. These would go down inside a cylindrical sample container (as in Fig. 4.4) which would be about 4 mm high and 1.5 mm in diameter on the outside. A sensible guess is that for good coupling efficiency the pads should be somewhat larger than the sample container, but they should not be much larger or again they would contribute unnecessary stray capacitance. As shown in Fig. 6.12 (which has dimensions in inches) the pads were chosen to be 2.5 mm wide and 5 mm high and are spaced by 1.5 times their width. To check what coupling efficiency this would lead to we made some measurements on a $\times 10$ scale model, as will be described below.

Note that once the pad width and spacing is chosen, and the number of pairs of pads is fixed, the rotor circumference is implied. Thus an explanation has now been given for why the rotor diameter was chosen to be 3 cm.

7.2 Electrostatic Efficiency

To discuss the efficiencies it is necessary to give a definite model of the electrostatics. Figure 7.2 identifies the lumped elements we will use. C_{GC} and C_{SC} are the ground and signal coupling capacitors, C_{TB} is the capacitance between the upper and lower halves of the rotor ("top to bottom"), and C_{IN} is the amplifier

input capacitance. These are all constant in time. $c_S(t)$ and $c_G(t)$ both vary periodically at the signal frequency and are assumed to have the same waveform but to be 180° out of phase. $c_S(t)$ and $c_G(t)$ are meant to represent the capacitance from the sample to all of the signal pads and to all of the ground pads, although only the capacitances to the adjacent pads are indicated in the diagram.

Figure 7.3 is a schematic for the lumped element model. Note that in the limit where C_{GC} and C_{SC} are large this circuit reduces to the original circuit of Fig. 4.2a, with the total capacitance C being now equal to $C_{IN} + C_{TB}$. It is straightforward to derive an expression for the voltage at the amplifier input

$$V(t) = Q \cdot \frac{\frac{1}{C_{IN}}\left(\frac{1}{c_G(t)} + \frac{1}{C_{GC}}\left(1 + \frac{C_{TB}}{c_S(t)} + \frac{C_{TB}}{c_G(t)}\right)\right)}{\frac{1}{C_{IN}} + \frac{1}{C_{GC}} + \frac{1}{C_{SC}} + \left(\frac{1}{c_S(t)} + \frac{1}{c_G(t)}\right)\left(1 + \frac{C_{TB}}{C_{IN}} + \frac{C_{TB}}{C_{GC}} + \frac{C_{TB}}{C_{SC}}\right)}. \quad (7.1)$$

We will assume that the signal is sinusoidal, since this is observed in practice *, and calculate the peak-to-peak voltage V_{pp} at the amplifier input, equal to $V_{max} - V_{min}$. When $V(t) = V_{max}$ the sample is over a signal pad and we will have $c_S(t) = c_{max}$ and $c_G(t) = c_{min}$, while when $V(t) = V_{min}$ the sample is over a ground pad and we have $c_S(t) = c_{min}$ and $c_G(t) = c_{max}$. c_{max} and c_{min} are the maximum and

---

* The only significant higher harmonic of the signal is the third, at 21.6 kHz. Its amplitude is about 5% of the 7.2 kHz signal and its phase is such that the total waveform is slightly triangular.

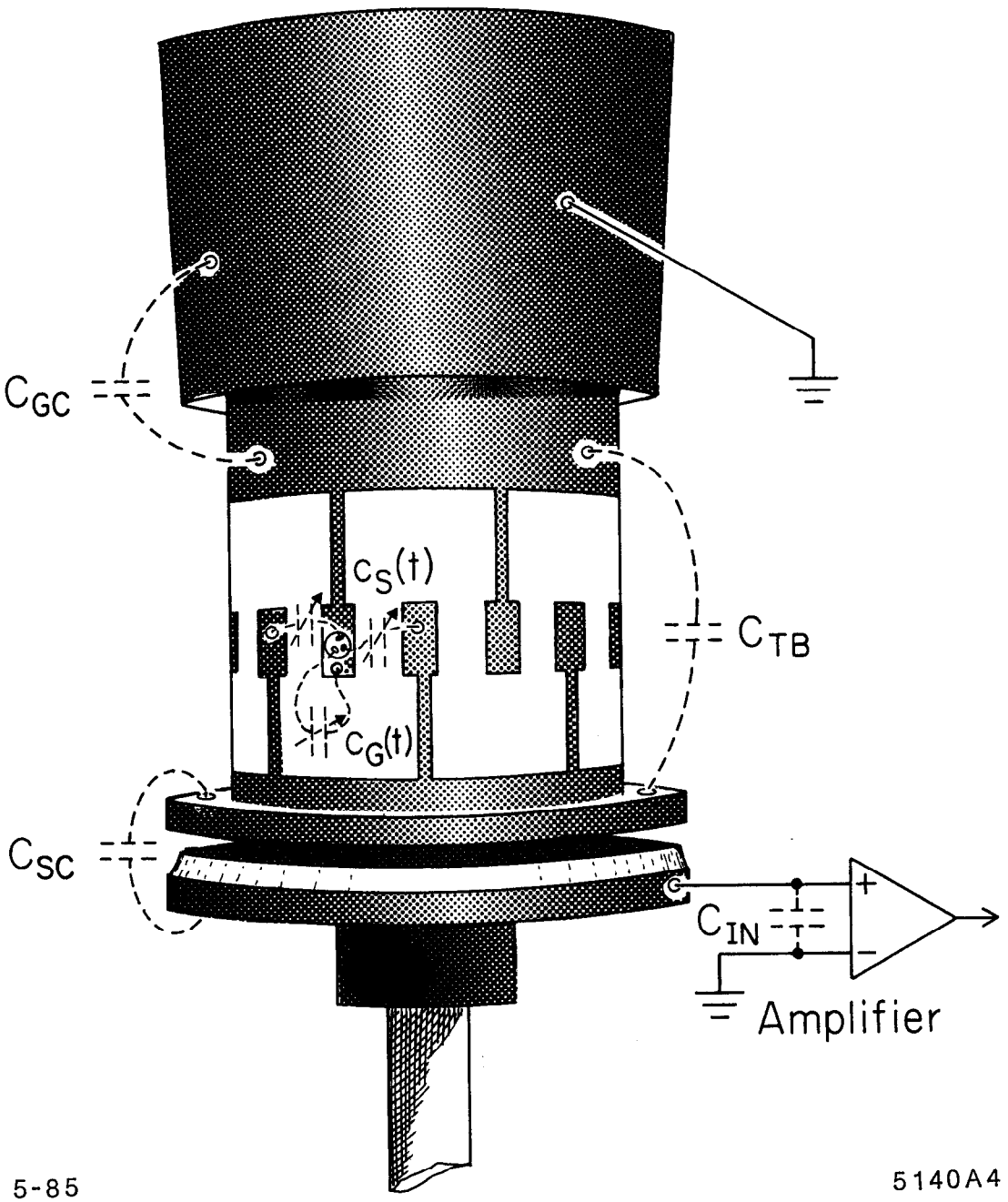

Figure 7.2. Capacitance Definitions

minimum values of both $c_G(t)$ and $c_S(t)$. One then finds

$$V_{pp} \simeq \frac{Q}{C_{IN}+C_{TB}} \cdot \frac{c_{max}-c_{min}}{c_{max}+c_{min}} \cdot \left(1+\frac{C_{IN}C_{TB}}{C_{IN}+C_{TB}} \cdot \frac{C_{SC}+C_{GC}}{C_{SC}C_{GC}}\right)^{-1} \equiv \frac{Q}{C_{IN}+C_{TB}} \cdot E_s \cdot E_c \tag{7.2}$$

The expression is now approximate because some terms proportional to $c_{max} \cdot c_{min}$ have been neglected, which is safe since both c_{max} and c_{min} are much smaller than any of the other capacitances. Each term now has a simple meaning. The first is the peak-to-peak voltage generated for perfect sample to pad coupling and infinitely large coupling capacitances. The second is the sample to pad coupling efficiency E_s which would be one if c_{min} were zero. The final term is the efficiency of the coupling capacitors E_c which is equal to one for $C_{SC}, C_{GC} \longrightarrow \infty$.

In chapter 9 data will be presented which shows that, for small test samples, the signal generated at the amplifier input per electron charge is 4.7 nV rms. We want to compare this to the value predicted by Eqn. 7.2, so we need C_{IN}, C_{TB}, E_c, and E_s. The amplifier input capacitance C_{IN} will be discussed in section 7.4; its measured value is $1.5 \pm .3$ pF. C_{TB} was measured to be $2.8 \pm .3$ pF on a bridge with the rotor out of the apparatus. Values for C_{SC} and C_{GC} were given in section 6.5. They may be used to calculate E_c; one finds $E_c = .87 \pm .03$. Evidently the coupling capacitors are large enough for good efficiency.

In order to get some estimate for E_s we made a $\times 10$ scale model of the pad structure. This was necessary because there was no way to measure the very tiny c_{max} and c_{min} on the apparatus directly. The measurements were made early in

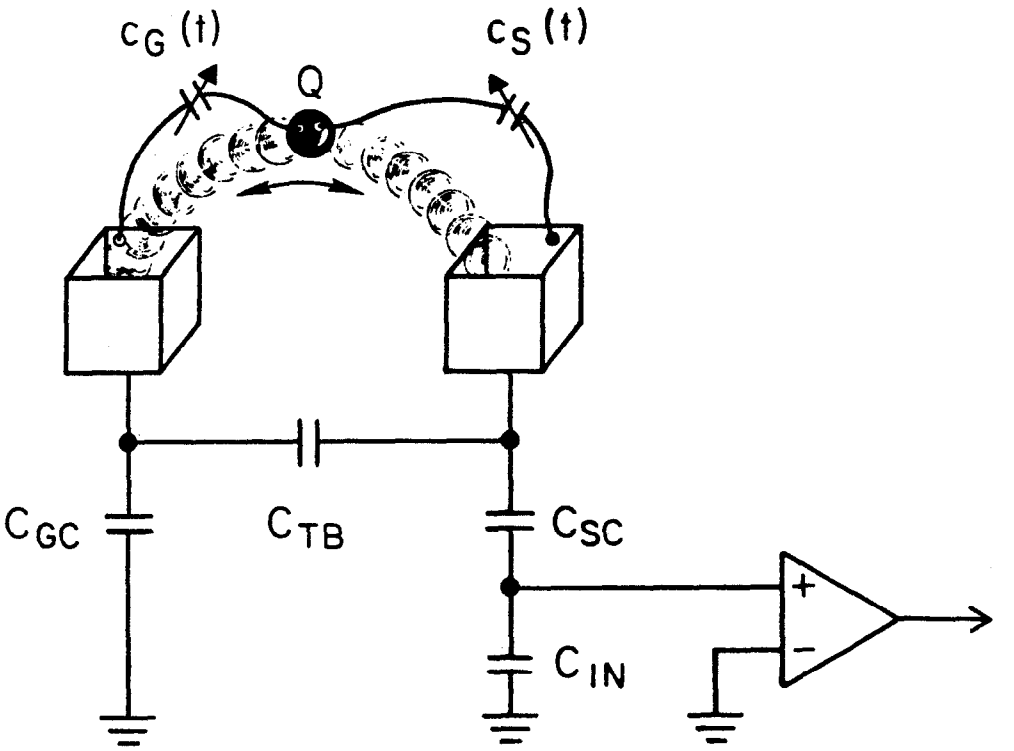

Figure 7.3. Lumped Element Model

the design process, and unfortunately the sample containers studied were not the same size or shape as the test samples eventually used in the instrument.

Measurements were made for a large cylindrical sample container whose height and diameter were equal to the pad height and width, and for a small one whose height and diameter were .4 times the pad height and width. For the large container E_s varied from $.70 \pm .10$ to $.40 \pm .10$ for container to rotor gaps of from .15 mm to .6 mm, and for the small container from $.80 \pm .05$ to $.70 \pm .05$ for the same range of gaps. (The gaps given are those for the actual device, not the $\times 10$ values used in the model.)

The smaller container used in the model corresponds most closely to the size of the test sample used in practice, but is still about a factor of two too large. The gap used in practice was .2 mm. The model data would suggest that we take $E_s = .75 \pm .05$, but we will raise the error to $\pm .10$ because of the size and shape discrepancy.

Equation 7.2 then implies

$$\begin{aligned} V_{\text{rms}} &= \frac{1}{2\sqrt{2}} \cdot \frac{q_e}{C_{IN} + C_{TB}} \cdot E_s \cdot E_c \\ &= \frac{1}{2\sqrt{2}} \cdot \frac{1.6 \cdot 10^{-19}\,\text{C}}{2.8 \pm .3 + 1.5 \pm .3\,\text{pF}} \cdot .75 \pm .10 \cdot .87 \pm .03 \\ &= 8.9 \pm 1.9\,\text{nV}, \end{aligned} \tag{7.3}$$

for the signal due to one electron charge on the sample. The errors for C_{IN}, C_{TB}, and E_c have been treated as correlated since they depend on the same systematics. The result is somewhat larger than the measured 4.7 nV calibration. We have no

good explanation for this, but clearly either the measured parameters are not as well known as the errors indicate, or the lumped element model is incomplete.

7.3 Sample Container

In section 4.2 it was claimed that if a deep enough sample container is used then it is possible to measure the net sample charge instead of just changes in the charge. Here we want to show what deep enough means.

We will restrict the considerations to conducting samples or to samples coated with a conductor, and will suppose that when the sample is placed in the container it makes a conducting contact with the inside of the container. In practice we suspect that it will be necessary to prepare two identical samples and compare their charge, because the instrument is very sensitive to motions of the sample container, and it will be easiest to maintain the sample container's position if it always has the same weight. For this reason alone we expect to not actually measure the net charge of the sample, but to measure the difference of the net charge of two samples. This is sufficient for a fractional charge search and is, of course, entirely different from only being able to measure changes in the charge of a single sample, which is all that can be done without the sample container.

The measurement procedure would thus involve first placing sample #1 into the sample container and averaging the output for a time T. Then sample #1 would be replaced by sample #2 and the output would again be averaged for a time T. The difference between the two averages measures the difference between the net charge of sample #1 and the net charge of sample #2. In fact this will be true

for any shape sample container so long as the samples are identical. Unavoidably they will not be identical—the most important effect will likely be that their surface potentials will differ, typically by about 30 mV.

To study this effect we again need a model for the electrostatics. In Fig. 7.4 we show the sample container with a sample inside, and indicate the important capacitances. $c_S(t)$ and $c_G(t)$ are again meant to represent the capacitances from the sample container to all of the signal pads and to all of the ground pads, although only one each is shown. We have ignored coupling capacitors for simplicity so as before $C = C_{IN} + C_{TB}$. $c'_S(t)$ and $c'_G(t)$ represent the capacitances from the top surface of the sample to the signal pads and ground pads. One may imagine that the top surface of the sample is a separate conductor from the rest of the sample, and to model the surface potential we imagine that there is a fixed potential V_s between the sample bulk and its top surface. Our task is to find out how the signal generated by the instrument depends on V_s. Figure 7.5 is a schematic for the situation. From it we may compute the signal at the amplifier input due to V_s

$$V(t) = V_s \cdot \left(\frac{c'_S(t)}{c_S(t) + c'_S(t)} - \frac{c'_G(t)}{c_G(t) + c'_G(t)} \right) \cdot \left(\frac{C}{c_G(t) + c'_G(t)} + \frac{C}{c_S(t) + c'_S(t)} + 1 \right)^{-1}. \tag{7.4}$$

We will make the same assumptions for $c'_S(t)$ and $c'_G(t)$ as were made before for $c_S(t)$ and $c_G(t)$; they are periodic at the signal frequency and have the same waveform but are 180° out of phase. We may then compute the peak-to-peak voltage if we

assume that $V(t) = V_{max}$ when $c'_S(t) = c'_{max}$ and $c'_G(t) = c'_{min}$ and so forth as before. The result is

$$V_{pp} \simeq V_s \cdot \frac{2}{C} \cdot \frac{c'_{max}c_{min} - c'_{min}c_{max}}{c_{max} + c_{min}}, \tag{7.5}$$

where some terms have been neglected that are very small because C is much greater than any of the other capacitances and c_{min}, c_{max} are much greater than c'_{min}, c'_{max}. Measurements on the model indicate that

$$\frac{c'_{min}}{c'_{max}} \ll \frac{c_{min}}{c_{max}}, \tag{7.6}$$

so the second term may be dropped. If this condition is somewhat violated the signal will be smaller so we still get an upper bound. For the rms signal we then have

$$V_{rms} \simeq \frac{V_s}{\sqrt{2}} \cdot \frac{c'_{max}}{C} \cdot \frac{c_{min}}{c_{max}}, \tag{7.7}$$

where we have made the additional assumption that the signal is sinusoidal and have neglected c_{min} compared to c_{max} in the denominator.

A $\times 10$ scale model of the sample container and sample with the proportions shown in Fig. 7.4 was constructed to measure c'_{max}, c_{min}, and c_{max}. This design is rather shallow since the container height is only twice the diameter, and is also rather large relative to the pad size. We found $c_{min}/c_{max} \sim .1$ for a range of sample to pad gaps, and $c'_{max} = 30\,\text{aF}$ in the model, corresponding to $c'_{max} = 3\,\text{aF}$ at true

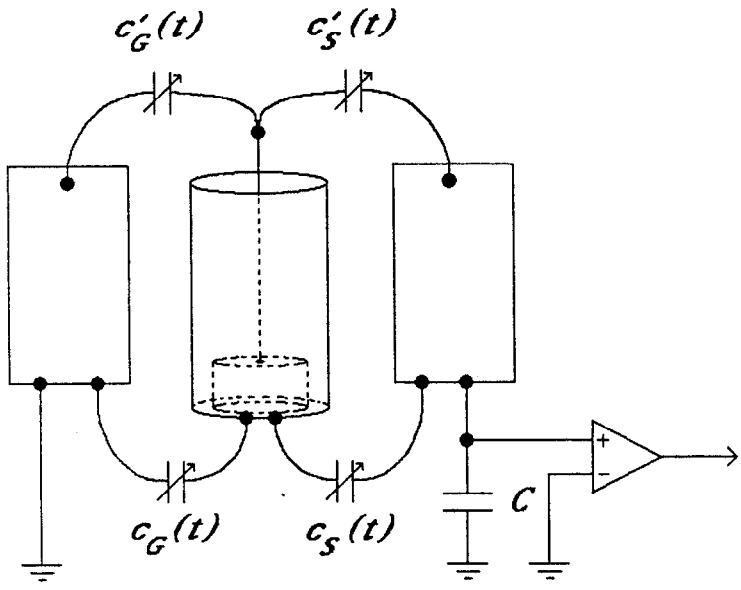

Figure 7.4. Sample Container Electrostatics

scale ($1\,\mathrm{aF} = 10^{-18}$ Farad). Thus for $V_s = 30\,\mathrm{mV}$ one finds

$$V_{rms} = \frac{30\,\mathrm{mV}}{\sqrt{2}} \cdot \frac{3\,\mathrm{aF}}{4.3\,\mathrm{pF}} \cdot .1 = 1.5\,\mathrm{nV}, \tag{7.8}$$

equivalent to the signal from a charge of $\sim .3q_e$, so if sample #1 had $V_s = 0$ and sample #2 had $V_s = 30\,\mathrm{mV}$, a fractional charge could be simulated. This sample container is therefore not quite good enough, but since one expects the shielding to improve very rapidly as the diameter is decreased and the sample is made smaller, an adequate arrangement could certainly be found.

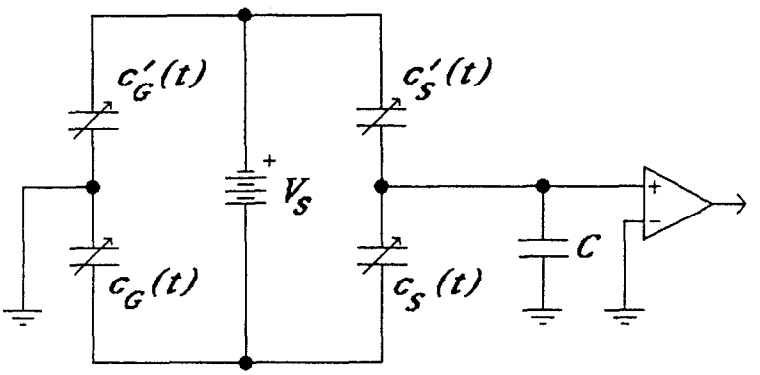

Figure 7.5. Sample Container Schematic

The reader may well feel that the discussion given above of the instrument's electrostatics is too crude. Unfortunately, it is not so easy to do better. First of all, it is difficult to measure small capacitances accurately because of the disturbances caused by the test leads, which decrease only logarithmically with the wire diameter. The best approach seems to be to make large scale models, since the capacitances to be measured will increase linearly with the scale size. Some more work of this kind might be done, but it is a very tedious way to proceed if one wants design guidance (rather than to simply characterize the chosen design) since many models must be studied. Simple analytic estimates of the capacitances can be made but for complicated three dimensional shapes it is impossible to be even as accurate

as the measurements already made. Perhaps some useful numerical work could be done—this has not been explored.

7.4 Amplifier Noise Properties

We first make some general points that do not depend on the choice of a JFET as the input device. Any *quiet* linear three terminal device may be represented by an impedance matrix $\|Z\|$ (see Fig. 7.6), yielding the equations:

$$\begin{aligned} v_g - v_s &= i_g z_i + i_d z_r, \\ v_d - v_s &= i_g z_f + i_d z_o. \end{aligned} \tag{7.9}$$

The subscripts g, s, and d are used because these terminals will become the gate, source, and drain when the general device is replaced by a FET.

An arbitrary *noisy* device may be modeled by adding a voltage noise generator and a current noise generator at the input (61). $\overline{i_n}$ and $\overline{v_n}$ are the square roots of the spectral densities of the generators*. In general they will be correlated so we define a complex correlation coefficient

$$c \equiv \frac{\overline{i_n^* v_n}}{\left(\overline{i_n^2}\,\overline{v_n^2}\right)^{1/2}}, \tag{7.10}$$

with $|c|^2 \leq 1$ as is usual.

When the device is placed in a feedback circuit $\overline{v_n}$ and $\overline{i_n}$ become generators for the feedback amplifier, as shown in Fig. 7.6. R_D is included here to model the input

---

* By $\overline{i_n}$ we really mean $\left(\overline{i_n^2}\right)^{1/2}$. This is a standard abuse of notation.

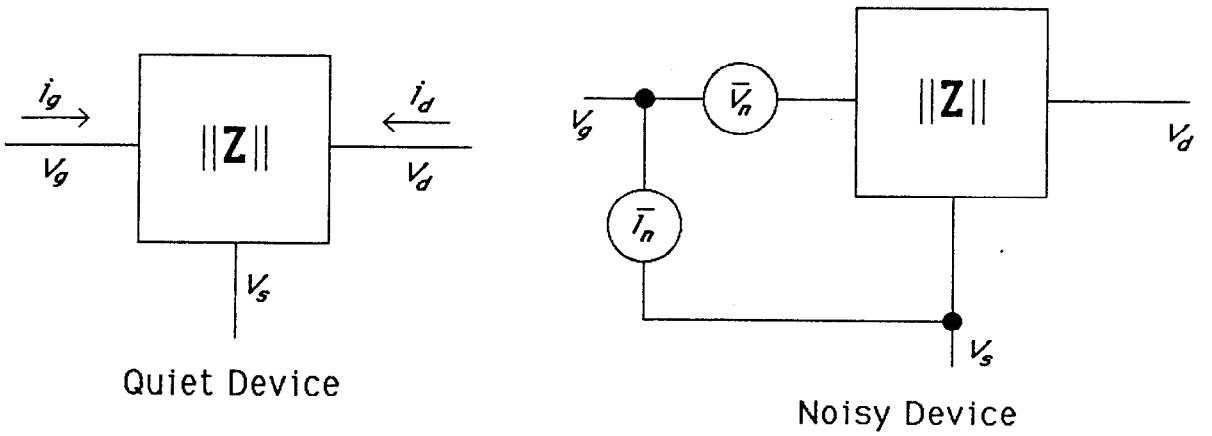

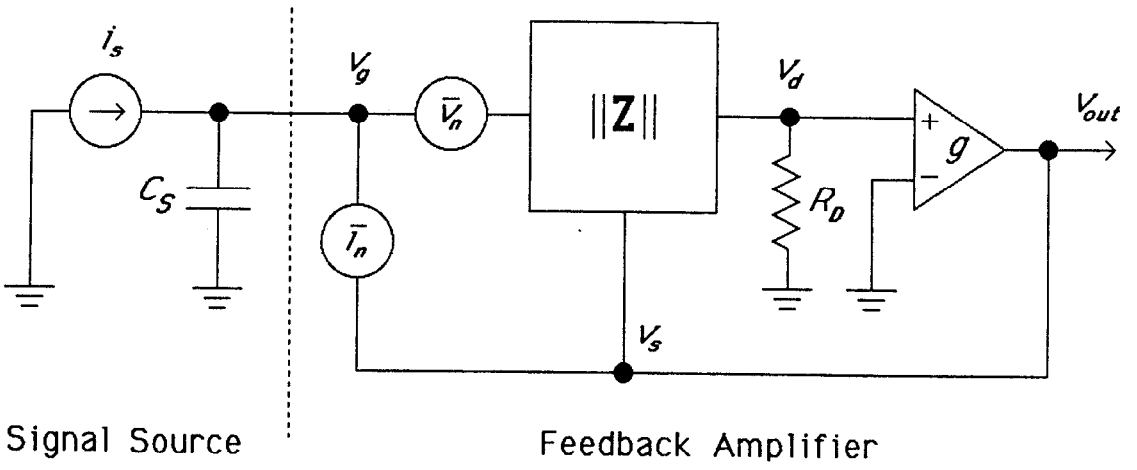

Figure 7.6. Noise Model for the Feedback Amplifier

impedance of the following stages. It is made explicitly a resistance because it will model the drain resistor in our circuit, but it might also be a general impedance. g is the loop gain not including the first stage. The signal source is specialized to model our instrument. Neglecting the finite size of the coupling capacitances, the source capacitance C_S is just equal to C_{TB}, as defined in Fig. 7.2. Neglecting also the imperfect sample coupling the current source is

$$i_s = \omega \frac{Q}{2\sqrt{2}}, \tag{7.11}$$

the rms current generated as the pads move past the sample.

It is now straightforward to calculate the input impedance of the amplifier

$$Z_{IN} \equiv \frac{v_g}{i_g} = z_i + z_f \cdot \frac{g - z_r/R_D}{1 - g + z_o/R_D}, \tag{7.12}$$

and the voltage gain

$$G \equiv \frac{v_{out}}{v_g} = \frac{1 - z_i/Z_{IN}}{1 - z_r/(gR_D)}. \tag{7.13}$$

Using these we may calculate the spectral density of the noise at the output

$$N = \left(\overline{i_n^2} + \omega^2 C_S^2 \overline{v_n^2} - 2Im(c)\omega C_S \overline{i_n}\,\overline{v_n}\right) \cdot \left|\frac{Z_{IN}}{1 + j\omega C_S Z_{IN}}\right|^2 \cdot |G|^2, \tag{7.14}$$

and the mean square signal at the output

$$S = \frac{\omega^2 Q^2}{8} \cdot \left|\frac{Z_{IN}}{1 + j\omega C_S Z_{IN}}\right|^2 \cdot |G|^2. \tag{7.15}$$

The signal to noise ratio* is thus

$$S/N = \frac{\omega^2 Q^2/8}{\overline{i_n^2} + \omega^2 C_S^2 \overline{v_n^2} - 2Im(c)\omega C_S \overline{i_n}\,\overline{v_n}}. \tag{7.16}$$

Only the imaginary part of the correlation coefficient appears in these expressions because the signal source is a pure reactance. The signal to noise ratio is seen to be independent of the drain resistor R_D and of the feedback loop gain g, and it is also independent of everything about the input device except the noise generators. This is a very important result since it shows just what one needs to know about an input device to judge its worth and shows that one has freedom to choose any amplifier circuit. In practice it may be necessary to measure some combination of the elements of $\|Z\|$ in order to measure $\overline{i_n}$, $\overline{v_n}$, and the correlation.

We may now go one step further and note that if one has a certain input device characterized by $\|Z\|$, $\overline{i_n}$, $\overline{v_n}$, and c one may always connect n such devices in parallel with the consequences:

$$\begin{aligned} \|Z\| &\longrightarrow \|Z\|/n, \\ \overline{i_n} &\longrightarrow n^{1/2}\overline{i_n}, \\ \overline{v_n} &\longrightarrow n^{-1/2}\overline{v_n}. \end{aligned} \tag{7.17}$$

This freedom may be used to optimize the signal to noise ratio. One finds

$$n_{opt} = \omega C_S \frac{\overline{v_n}}{\overline{i_n}}, \tag{7.18}$$

---

* By S/N we sometimes mean the signal to noise times the bandwidth, as here.

$$(S/N)_{opt} = \frac{Q^2}{16C_S} \cdot \frac{1}{J(\omega)}, \tag{7.19}$$

where we have defined

$$J(\omega) \equiv \frac{\overline{i_n}\,\overline{v_n}}{\omega}(1 - Im(c)). \tag{7.20}$$

$J(\omega)$ has units Joules/Hz and will be called the energy sensitivity of a device. It depends only on the device noise parameters and the operating frequency. The name is apt since the optimal signal to noise is simply the ratio of the mean electrostatic energy that would be present in the source capacitance if it were disconnected from the amplifier, to the "energy sensitivity" of the input device. In principle one may also implement optimal matching with a transformer, but this cannot be done efficiently at audio frequencies.

The most quiet devices for frequencies around 10 kHz are SQUIDs, which can have $J(\omega) \sim 100\hbar$ (62). ($\hbar$ is used to express $J(\omega)$ because the quantum limit for linear amplifiers is thought to be $J(\omega) \sim 1\hbar$ (63).) Unfortunately SQUIDs cannot be used in our application because they are grossly mismatched; n_{opt} is around 10^{-5}. Some attempts have been made to increase the SQUID input impedance with a transformer, but it has not been possible to equal the performance of a JFET for signal sources like ours (64). Other devices one might consider are bipolar transistors, MOSFETs, and GaAsFETs; all these have larger $J(\omega)$ than JFETs for frequencies near 10 kHz, and while for MOSFETs and GaAsFETs n_{opt} would be near one, bipolar transistors have $n_{opt} < 1$, so optimal matching cannot be implemented. N-channel JFETs are the best choice for our application. As discussed next, JFETs

have $J(\omega) \sim 10^{-28}\,\mathrm{J/Hz} \sim 10^6\hbar$ at 10 kHz and the smallest available devices are fairly well matched to our source.

A commonly used lumped element model for the FET is given in Fig. 7.7. C_{gs} and C_{gd} are the input capacitances, equal to a few pF for the device we use, r is the channel resistance, and g_{fs} is the forward transconductance equal to $\sim$ 2 mmho. From this model one may calculate the elements of $\|Z\|$ and then use them to find the amplifier input impedance Z_{IN}. The result is

$$Z_{IN} \simeq \frac{1}{j\omega C_{gd}}. \tag{7.21}$$

Thus the amplifier input impedance is capacitive, and the input capacitance C_{IN} is approximately equal to C_{gd}. This result would be exact in the limit of high loop gain ($g \gg 1$) and low frequency ($\omega \ll 1/rC_{gd}$). The characterization of the FET properties below depends only on the input impedance being capacitive (which is observed) and not on $C_{IN} = C_{gd}$, so we shall continue to call the input capacitance C_{IN}.

The total noise referred to the FET input follows from Eqn. 7.14

$$\overline{v_{tot}^2} = \frac{\overline{i_n^2}}{\omega^2 C_{IN}^2} \cdot \frac{C_{IN}^2}{(C_{IN}+C_S)} + \overline{v_n^2} \cdot \frac{C_S^2}{(C_{IN}+C_S)} - 2Im(c)\frac{\overline{i_n}}{\omega C_{IN}}\overline{v_n}\frac{C_{IN}C_S}{(C_{IN}+C_S)^2}. \tag{7.22}$$

This is the expression to which measured noise data must be fit. C_{IN} can be measured directly by driving the amplifier input through a known small capacitance, though it is difficult to be accurate. One can then measure $\overline{v_{tot}^2}$ at various frequencies

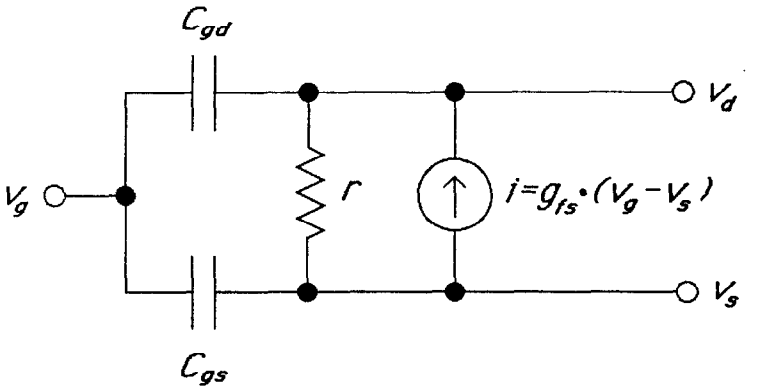

Figure 7.7. FET Circuit Model

and with various values for C_S and do a fit to extract $\overline{v_n}$, $\overline{i_n}$, and $Im(c)$.

The raw noise data for the 2N3686 used in our apparatus is given in Table 7.1. The test loads used were all polystyrene to eliminate any contribution from dielectric loss and, as discussed in section 6.6, no gate bias resistor was used. C_{IN} was measured to be $1.5 \pm .3\,\mathrm{pF}$. Results of a fit to Eqn. 7.22 are given in Fig. 7.8 together with the values for $J(\omega)$ calculated from Eqn. 7.20. The errors come mostly from uncertainties in the capacitances.

The most important piece of information, of course, is that the total amplifier noise at 7.2 kHz and with a 2.8 pF load (since $C_{TB} = 2.8\,\mathrm{pF}$) is $8.3\,\mathrm{nV}/\sqrt{\mathrm{Hz}}$. This, together with the measured calibration of the instrument of $4.7\,\mathrm{nV}/q_e$, gives the actual signal to noise for a charge of $1q_e$:

$$S/N = \frac{(4.7\,\mathrm{nV})^2}{(8.3\,\mathrm{nV}/\sqrt{\mathrm{Hz}})^2} = (.57)^2\,\mathrm{Hz}. \tag{7.23}$$

Table 7.1– 2N3686 Noise Data. Total noise for various values of C_S. C_S is known $\pm.3\,\mathrm{pF}$ and the noise measurements are accurate to 5%.

C_S	2 kHz	4 kHz	7.2 kHz	16 kHz
1000 pF	$3.6\,\mathrm{nV}/\sqrt{\mathrm{Hz}}$	$3.3\,\mathrm{nV}/\sqrt{\mathrm{Hz}}$	$3.1\,\mathrm{nV}/\sqrt{\mathrm{Hz}}$	$2.9\,\mathrm{nV}/\sqrt{\mathrm{Hz}}$
20.5	4.8	4.3	3.8	3.5
10.5	7.5	5.7	4.8	4.0
5.2	10.5	7.9	6.2	5.2
2.8	15.2	10.5	8.3	6.3
0	43	30	22	16.0

Or in other words, the rms fluctuation at the output due to the amplifier noise (with the efficiencies $E_s = E_c = 1$) is $1.75\,q_e/\sqrt{\mathrm{Hz}}$.

The other information is important for design guidance. Equation 7.18 may be used to calculate n_{opt}; we find $n_{opt} = .28$ at 7.2 kHz and with $C_S = 2.8\,\mathrm{pF}$. Since n_{opt} is less than one, optimal matching cannot be implemented, and it seems that we should be using a smaller FET. Unfortunately the chosen FET was selected from among the smallest devices made and no smaller devices of similar quality seem to be available. If a smaller device could be found then Eqn. 7.16 and Eqn. 7.19 allow us to calculate the benefit that might be expected. We find

$$\frac{(S/N)_{opt}}{S/N} = 1.7, \tag{7.24}$$

for $C_S = 2.8\,\mathrm{pF}$ and $\omega = 2\pi \cdot 7.2\,\mathrm{kHz}$, so evidently the mismatch is not so bad. Equation 7.16 and the fit noise parameters allow us to calculate how S/N depends on frequency and the load capacitance C_S. Fig. 7.9 shows the results plotted two different ways. The plot on the left makes clear why the region around 10 kHz

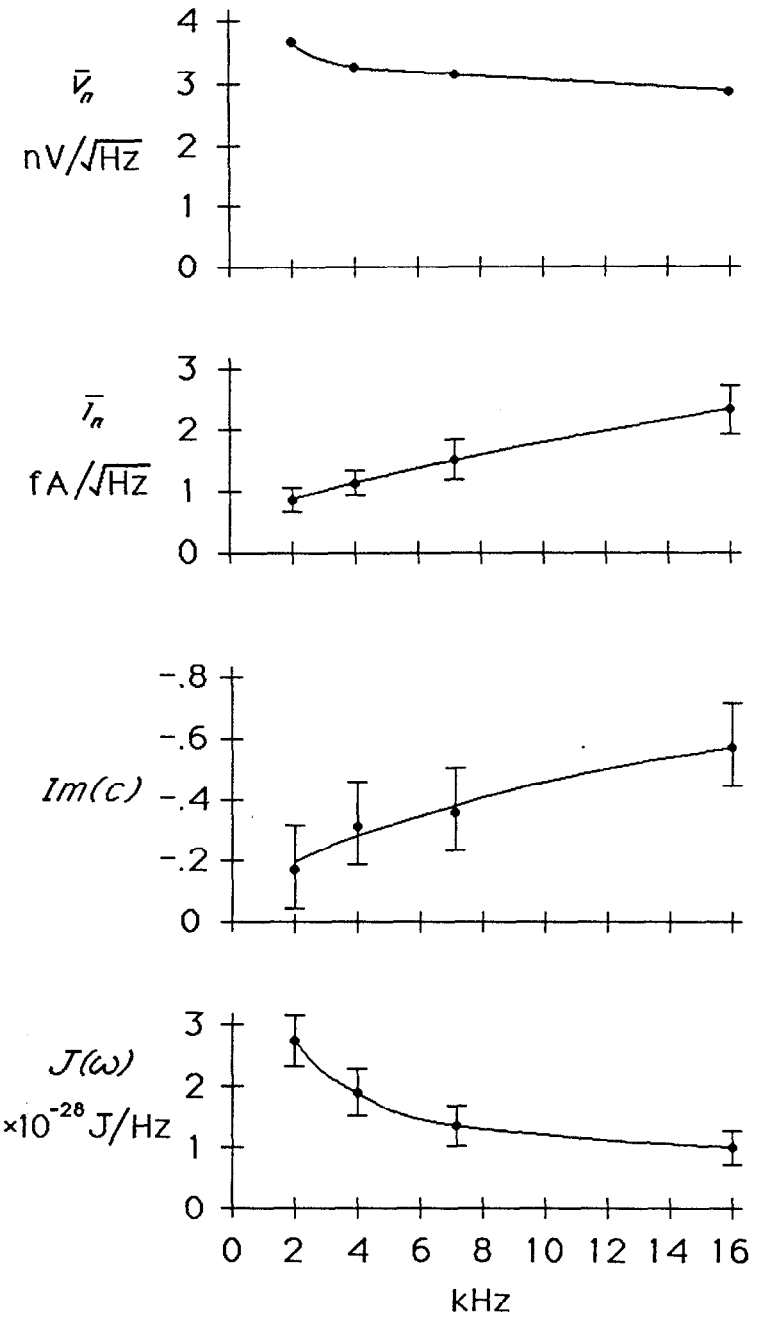

Figure 7.8. Measured 2N3686 Noise Parameters

was chosen for the operating frequency since the signal to noise decreases rapidly at lower frequencies. Clearly it would be better to spin faster and have a higher signal frequency, but we are currently limited by mechanical factors which will be discussed in the next chapter. The main reason why S/N improves from 7.2 kHz to 16 kHz is that the matching is improving. Once the matching is optimal the S/N will stop improving since $J(\omega)$ improves only slightly above about 10 kHz. From the plot on the right it is apparent that there is not much to be gained by decreasing C_S below 2.8 pF unless the frequency can be raised. Equation 7.19 shows that if somehow optimal matching can be maintained then $S/N \propto 1/C_S$.

Two methods have been discussed in the literature for improving the noise performance of JFETs. Several authors have claimed that the dielectric loss of the glass header used to mount the FET chip contributes to the total noise (65, 66). While this may be true in some circumstances, it is not an important effect for us. This has been demonstrated directly by connecting a second header across the input and noting that the noise does not increase. In fact the noise decreases slightly because of the additional $\sim$ .3 pF of the second header, as would be expected. A more important issue for us is the possibility of cooling the FET. At the optimal temperature of 150 °K an improvement of about a factor of two in $J(\omega)$ can be expected, according to the data of Bordoni *et al.* (65). We did some work on a cooled amplifier appropriate to model II (67), which had $C_S \sim 20$ pF, but have not yet made measurements with $C_S = 2.8$ pF.

No mention has been made here of the mechanism for JFET noise, but the

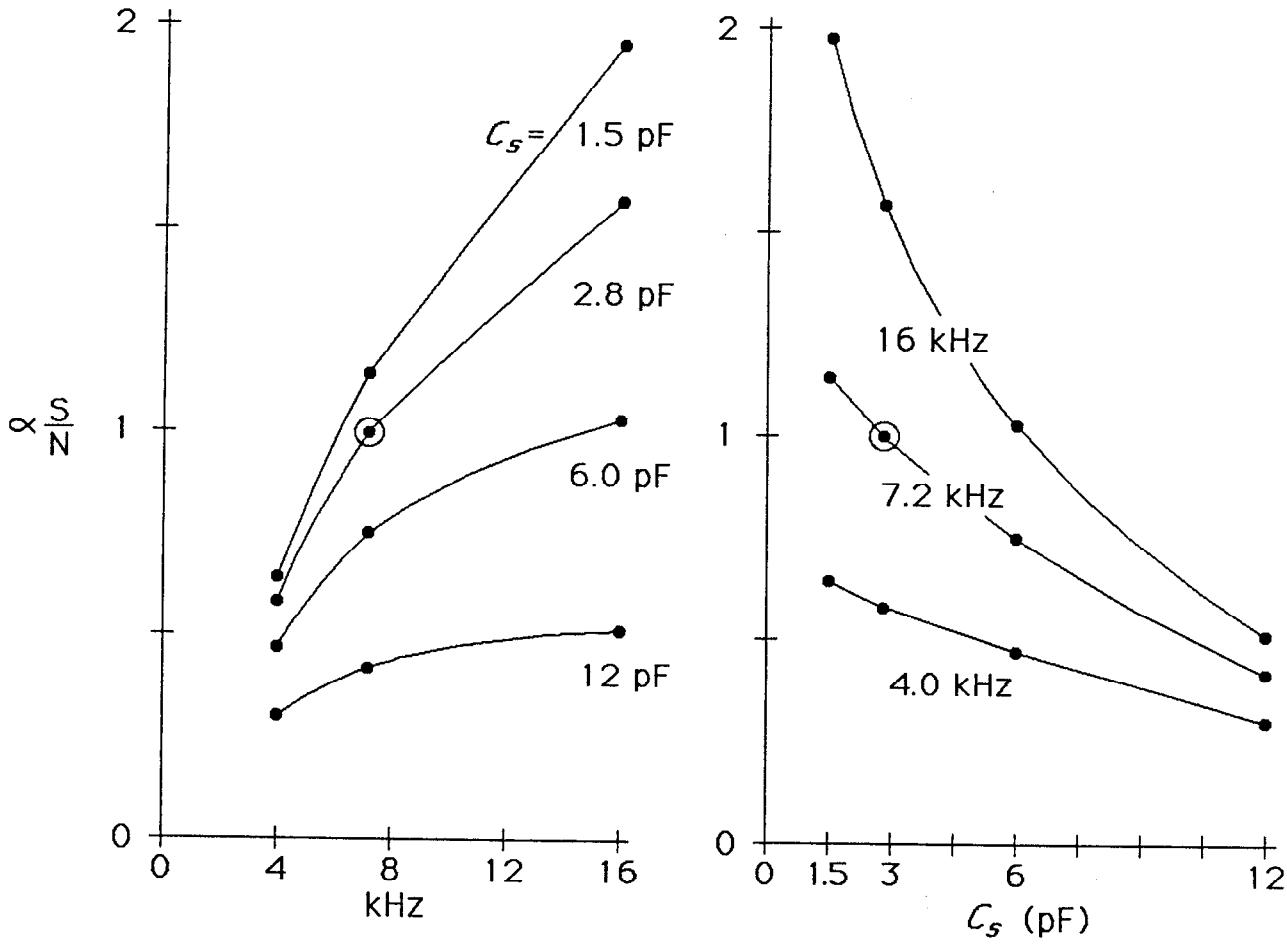

Figure 7.9. Signal to Noise versus C_S and Frequency. The circle indicates the present operating point.

subject is well understood at least in general terms according to the original discussion of Van der Ziel (68), who identified the Johnson noise of the channel resistance and the shot noise of the gate leakage current as the main effects.

Before closing this section it might be worthwhile to point out that the treatment given here of JFET noise is a bit unorthodox. Most authors model the FET with noise generators placed after the FET input capacitance. This changes the expressions and would be more clumsy for our purposes. A treatment of the noise matching problem using the more common language has been given by Bordoni and Pallottino (69), who consider the problem of matching a JFET to a piezoelectric transducer for a gravity wave detector.

8. Mechanical Design

In this chapter some mechanical issues relevant to the rotor electrometer design are discussed. First the relationship between critical speeds and vibration is explained and it is explained why the spin speed was chosen to be below the frequency of the lowest flexural mode of the rotor. Next some requirements on the rotor material are discussed and alternatives to the polystyrene design are considered. A treatment of the rotor gyrodynamics follows and it is used to describe the forward whirl instability, an important practical problem which arose during mechanical tests with prototype rotors. Finally the whole design process is summarized.

8.1 Vibration and Critical Speeds

An essential breakthrough in the engineering of high speed rotating devices was made by De Laval in the 1880's while he was struggling with vibration problems in a centrifuge designed to separate cream from milk (70). De Laval discovered that if he replaced the stiff steel shaft of his high speed rotor with a much more flexible shaft, then once past a critical rotation speed the rotor tended to center itself and vibrations were greatly reduced.

The mechanism for autocentering can be understood with a simple model (71). Suppose a massive unbalanced rotor is placed on a massless flexible shaft, as shown in Fig. 8.1. Let the rotor mass be m and the distance from the center of the shaft to the center of mass be ϵ. If the spring constant tending to keep the shaft straight

is k, then by balancing the centrifugal and spring forces one finds

$$mr\omega^2 = k(r - \epsilon), \tag{8.1}$$

where r is the distance from the center of mass to the rotation axis. Solving for r yields

$$r = -\epsilon \frac{\omega_c^2}{\omega^2 - \omega_c^2}, \tag{8.2}$$

where

$$\omega_c^2 \equiv \frac{k}{m}. \tag{8.3}$$

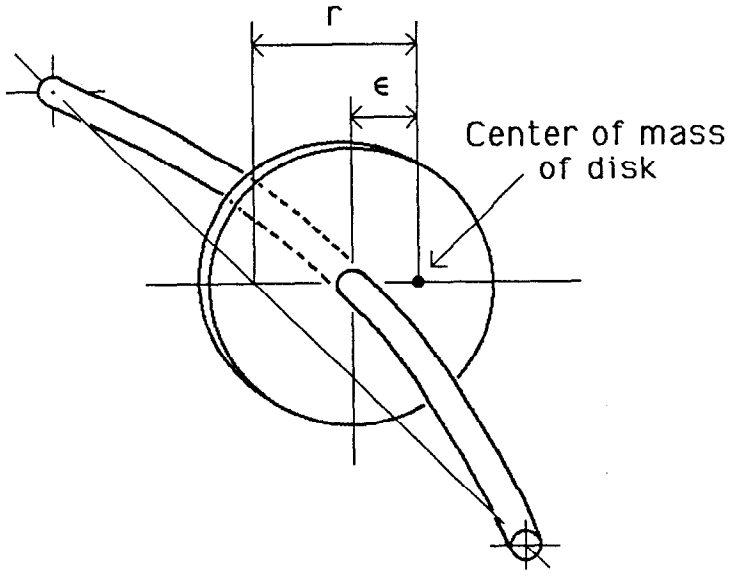

Figure 8.1. An Unbalanced Rotor

The "critical speed" ω_c is equal to the frequency of transverse vibrations with the rotor not spinning. At the critical speed the shaft deflection diverges but above

it $r \longrightarrow 0$ so that the rotor spins about its center of mass. Since the vibration causing force applied by the shaft to its supports is just the centrifugal force, one finds that

$$F_{vib} = m\epsilon\omega_c^2 \frac{1}{1-(\omega_c/\omega)^2}, \tag{8.4}$$

implying that for $\omega \gg \omega_c$ the vibratory forces are a factor $(\omega/\omega_c)^2$ less than they would be with a stiff shaft. Thus one should make ω_c as small as possible for low vibration.

For the more complicated example of a flexible shaft with distributed mass mounted on elastic bearings, there are critical speeds for each transverse normal mode. The lowest mode might be a rigid translation of the shaft in the flexible bearings while higher modes would include flexure of the shaft.

The chief attraction of the Beams type magnetic bearing used in the rotor electrometer is the extremely low critical speed that may be obtained for the lowest modes. In our instrument there are two low frequency transverse normal modes for which the rotor may be considered rigid. One is a pendulum motion for which the top of the rotor remains fixed and the bottom moves sinusoidally. For the other mode the ends of the rotor move sinusoidally and a point near the center of mass is fixed. The frequencies are:

$$\begin{aligned} \omega_1 &= \left(\frac{mgl}{I_x + ml^2}\right)^{1/2} = 2\pi \cdot 1.5\,\text{Hz}, \\ \omega_2 &= \left(\frac{k_x l^2}{I_x}\right)^{1/2} = 2\pi \cdot 4.1\,\text{Hz}. \end{aligned} \tag{8.5}$$

Here g is the acceleration of gravity, l is the distance from the center of mass to the

top of the rotor, k_x is the spring constant for horizontal motions of the top of the rotor relative to the suspension magnet, and I_x is the moment of inertia of the rotor about a horizontal axis through the center of mass. The numbers given result from substituting in measured values of l, k_x, and I_x, which will be given later. The above expressions ignore the fact that the magnet itself is free to move horizontally in an oil bath, which changes the frequencies somewhat but more importantly provides damping for the modes.

A system of this type will also have higher critical frequencies, the next highest one being the lowest transverse flexural mode of the rotor. For our system it is at 1220 Hz, well above the 900 Hz operating speed. Consequently our system is *supercritical* with respect to the bearing modes but *subcritical* with respect to flexural modes. The rotor will thus tend to rotate about an optimal axis (a principal axis in the limit $k_x \longrightarrow 0$), but will not deform to correct a misalignment between the axis of the ferromagnetic bearing piece and the axis of the polystyrene body, for example.

Early in the design phase it was thought to be important to keep the bearing far away from the signal generating part of the rotor, because of fear that the bearing would generate unwanted signals. For this reason long rotors were considered whose lowest flexural normal mode was well below the operating speed. Prototypes were unsuccessful, deforming so much near the critical speeds that they hit the sides of the vacuum chamber. There are two ways to limit the amplitude of shaft flexure while passing through critical speeds, one is to have high acceleration, the other is

to apply viscous damping to the bearing mounts. Dimentberg (72) and Macchia (73) have shown that with no damping the peak deflection on passing through a critical speed at ω_0 for constant angular acceleration $\dot{\omega}$ is given by

$$r_{max} = 1.5 \cdot \epsilon \cdot \frac{\omega_0}{\dot{\omega}^{1/2}}, \tag{8.6}$$

so that one wants $\dot{\omega}^{1/2} \sim O(\omega_0)$. The present design has $\dot{\omega} \sim 2\pi \cdot 1$ Hz/sec so that the condition $\dot{\omega}^{1/2} \sim O(\omega_0)$ is very far from satisfied for critical speeds anywhere near the required operating speed. Higher torques might make it possible to pass through flexure critical speeds but are difficult to apply because the rotor is unconstrained horizontally. Commonly used high torque electric motors have small gaps between ferromagnetic elements which are unstable radially making them unsuitable for this application. Except at very low speeds, the mass of the magnet and the weak horizontal spring constant seem to make it difficult to apply enough viscous damping at the top of the rotor to assist the transition through critical speeds.

Because of the above considerations it was decided to make the rotor as long as possible consistent with keeping the operating speed below the first flexural mode. Note that the condition $\dot{\omega}^{1/2} \sim O(\omega_0)$ is satisfied for the low frequency modes of Eqn. 8.5 for which the rotor is rigid, so that passage through these critical speeds is not a problem.

A calculation of the amplitude of the horizontal motion of the magnet will indicate the effectiveness of our arrangement for reducing vibrations. The rotor body and bearing piece were measured concentric to better than $\epsilon = 25\,\mu$m during

construction. At speed the bearing would be centered somewhat better, say to $\epsilon = 5\,\mu$m. The amplitude of the periodic force applied to the magnet is $F = k_x\epsilon$. The amplitude of motion for the magnet is thus

$$x = \frac{F}{m_m\omega^2} = \frac{k_x\epsilon}{m_m\omega^2} = .22\,\text{nm}, \tag{8.7}$$

for $\omega = 2\pi \cdot 900\,\text{Hz}$ and the magnet mass $m_m = 26\,\text{g}$.

8.2 Rotor Materials

The choice of a material for the rotor is constrained by several requirements. The specific modulus of elasticity (E/ρ, the modulus of elasticity divided by the mass density) should be high so that the frequency of the lowest bending mode can be as high as possible. The rotor material should also have a high specific tensile strength (σ/ρ, the tensile strength divided by the mass density) so that the spin speed will not be limited by burst. There are two important electrical requirements: the dielectric constant should be low to keep the total capacitance down, and the dielectric loss angle should be small enough so that the dielectric does not contribute significant Johnson noise. Below we show how well the present design satisfies these requirements and then consider alternatives.

For a tube of radius r and length l the frequency of the lowest bending mode is

$$\omega_0 = \frac{(3.93)^2}{l^2}\frac{r}{\sqrt{2}}\left(\frac{E}{\rho}\right)^{1/2}, \tag{8.8}$$

where E is the elastic modulus and ρ is the mass density (74). The factor of $\sqrt{2}$ is for a tube with thin walls and would be replaced by 2 for a solid bar. It is

Table 8.1– Rotor Materials. E/ρ is the specific modulus of elasticity in $(\text{cm/sec})^2$, σ/ρ is the specific tensile strength in $(\text{cm/sec})^2$, κ is the dielectric constant, and δ is the dielectric loss angle.

Material	E/ρ	σ/ρ	κ	δ
Polystyrene	$2.1 \cdot 10^{10}$	$4.8 \cdot 10^{8}$	2.5	.0001
Polyphenylene Oxide	$3 \cdot 10^{10}$	$5 \cdot 10^{8}$	2.6	.0004
Polycarbonate	$2 \cdot 10^{10}$	$5 \cdot 10^{8}$	3.0	.001
Quartz Glass	$2 \cdot 10^{11}$	$2 \cdot 10^{8}$	3.8	.0001
Alumina Ceramic	$1 \cdot 10^{12}$	$5 \cdot 10^{8}$	9.6	.00003
Steels	$3 \cdot 10^{11}$	$1 \cdot 10^{8} - 4 \cdot 10^{8}$	–	–
Aluminum Alloys	$3 \cdot 10^{11}$	$4 \cdot 10^{8} - 2 \cdot 10^{9}$	–	–
Titanium Alloy	$2 \cdot 10^{11}$	$2 \cdot 10^{9}$	–	–
Beryllium	$2 \cdot 10^{12}$	$1 \cdot 10^{9} - 3 \cdot 10^{9}$	–	–

therefore better to make the rotor hollow; a factor of $\sqrt{2}$ is gained in the frequency of the lowest mode. The factor of 3.93 is dependent on the boundary conditions, chosen here to be free at one end and hinged at the other. The hinged end is an approximate way to model the large weight of the bearing at the top of the rotor in our design. With $l = 18\,\text{cm}$, $r = 3\,\text{cm}$, and the properties of polystyrene given in Table 8.1, Eqn. 8.8 gives $\omega_0 = 2\pi \cdot 1170\,\text{Hz}$. The measured frequency of the lowest bending mode of the rotor is $2\pi \cdot 1220\,\text{Hz}$, in agreement with the calculation.

The bursting speed of a tube spun about its axis is given by

$$\omega_b = \frac{1}{r}\left(\frac{\sigma}{\rho}\right)^{1/2}, \tag{8.9}$$

where σ is the tensile strength. This is $2\pi \cdot 2300\,\text{Hz}$ for our design and so is not a limiting factor. An important point to note is that if one wishes to raise the signal frequency as much as possible then the requirement that the rotor not burst places

no restriction on the rotor radius, since the maximum peripheral velocity is equal to $(\sigma/\rho)^{1/2}$ and is independent of r. Also note that since neither ω_0 nor ω_b depend on the thickness of the walls of the rotor, they can be made thin, which helps in the pad region to keep the capacitance down.

The dielectric constant of polystyrene has the very low value of 2.5.

The dielectric loss requirement is very stringent and limits the choice of materials. Assuming that the whole 2.8 pF rotor capacitance C_{TB} goes through the dielectric and that there is an additional 1.5 pF amplifier capacitance C_{IN} in parallel (see Fig. 8.2), one may compute the noise voltage at the amplifier input due to dielectric loss

$$\overline{v_n} = \left(4kT\frac{\delta}{\omega C_{TB}}\right)^{1/2} \frac{C_{TB}}{C_{IN}+C_{TB}} = 2.3\,\mathrm{nV}/\sqrt{\mathrm{Hz}}, \tag{8.10}$$

assuming a dielectric loss angle $\delta = 10^{-4}$ (the value for polystyrene*), and $\omega = 2\pi \cdot 7.2\,\mathrm{kHz}$. This noise source when added in quadrature with the $8.3\,\mathrm{nV}/\sqrt{\mathrm{Hz}}$ amplifier noise makes only a small contribution to the total noise. Materials with dielectric loss higher than about $4 \cdot 10^{-4}$ would be unacceptable. Note that if the signal frequency could be raised then larger dielectric loss angles could be tolerated.

The all polystyrene design is easy to fabricate and simple, but several other possibilities might be considered. Table 8.1 includes some other low loss insulators.

* 10^{-4} is the value for Rexolite 1422 polystyrene at 1 MHz. δ is not given by the manufacturer at lower frequencies but an extrapolation suggests δ may be $3 \cdot 10^{-5}$ at 7.2 kHz. The 10^{-4} value used here is conservative.

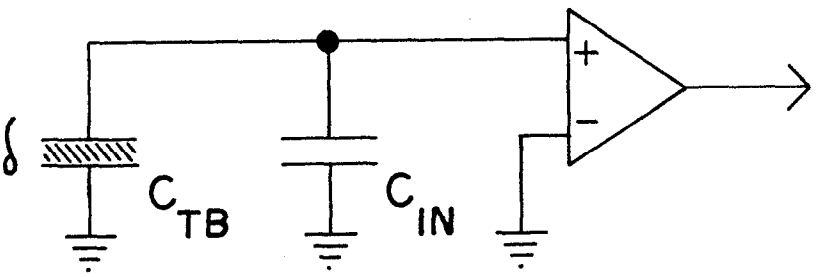

Figure 8.2. Circuit Model for Dielectric Loss Noise

The plastics listed, polyphenylene oxide and polycarbonate, have mechanical properties very similar to polystyrene but have somewhat higher dielectric loss and dielectric constant. Polyphenylene oxide might serve as well as polystyrene in our design but we know of no advantages. The only other low loss plastics we know of are polyethylene and polytetrafluoroethylene (Teflon), both of which have very poor mechanical properties.

Quartz glass can have a low dielectric loss angle and has a specific modulus of elasticity an order of magnitude greater than polystyrene. Unfortunately the dielectric constant is rather high and strength can be a problem since glass cannot flow to relieve stress concentrations*. Alumina ceramic is even stiffer than quartz glass and is extremely low loss, however its high dielectric constant is prohibitive.

---

* An early prototype made of a quartz glass tube shattered at 350 Hz for no apparent reason. Glass dust makes a terrible mess in vacuum systems.

One might consider either quartz glass or alumina in a composite design where the pad region would be made of polystyrene and the stiffer material would be used for the upper part of the rotor.

In a composite design one might also consider making the whole upper part of the rotor of a conducting material with a polystyrene part added to the bottom to carry the pads. The motor used in the present design would require modification to eliminate eddy current problems. Also the ground coupling capacitor would then be connected to the bearing, a problem if any signals are generated by the bearing, but this is not known to be the case. Table 8.1 includes the mechanical properties of some conductors. One sees that the specific modulus of elasticity and tensile strength could be one to two orders of magnitude greater than for polystyrene. Beryllium looks particularly attractive, although there are fabrication difficulties.

8.3 ROTOR GYRODYNAMICS

The analysis of the rotor's dynamics presented below was forced upon us by the destruction of a prototype rotor when its forward whirl mode* was excited to the point that the rotor hit the walls of the chamber. This discussion of dynamics is completely separate from the discussion of section 8.1 on critical speeds, for here we are concerned with the rigid body normal modes of the rotor when it is spinning at full speed, and not the problem of passing through critical speeds to get to full speed.

We first show that there are three transverse motions of the rotor: The

* This is the same as the wobbling motion seen when a football is poorly thrown.

forward whirl whose frequency is proportional to the spin speed, a slow gravitational precession at a frequency inversely proportional to the spin speed, and a horizontal oscillation whose frequency is independent of the spin speed. Then a theory is given for the threshold spin speed at which the forward whirl mode becomes unstable, but unfortunately it does not give a good description of the observed behavior. A partly empirical theory which uses measured values of the whirl driving force is more successful.

8.3.1 Normal Modes

The rotor's rigid body motions may be described using standard methods of gyrodynamics (75). We will model the system as a rapidly spinning symmetric body subject to gravity with its top point constrained by a harmonic potential. The moments of inertia (defined about principal axes through the center of mass) satisfy $I_x = I_y > I_z$. Fig. 8.3 shows the geometry. The constraining forces, indicated schematically by the spring, are harmonic and isotropic horizontally, but have a different spring constant vertically. The vertical force applied to the top of the rotor includes a constant upwards force mg to model the suspension magnet while the spring constant k_z models the active feedback of the magnetic suspension. The gravitational force mg is applied to the center of mass. The equations of motion are

$$\begin{aligned} \vec{F}_{external} &= m\ddot{\vec{R}}_{cm}, \\ \vec{N}_{external} &= \dot{\vec{L}}. \end{aligned} \tag{8.11}$$

The torque and angular momentum must be defined about the center of mass, and

the time derivative must be inertial, and not with respect to rotating axes.

Four different coordinate systems are indicated in Fig. 8.3. $(\mathrm{X}, \mathrm{Y}, \mathrm{Z})$ is a fixed orthogonal frame. $(\mathrm{X}', \mathrm{Y}', \mathrm{Z}')$ can only translate relative to $(\mathrm{X}, \mathrm{Y}, \mathrm{Z})$ and is attached to the rotor's center of mass. (x, y, z) is another orthogonal set fixed to the center of mass but these are rotated by an angle θ_1 about X' and by an angle θ_2 about y. (x, y, z) are principal axes but are not body fixed. y is always in the $\mathrm{Y}' - \mathrm{Z}'$ plane and z is aligned with the rotor's symmetry axis. $(1, 2, 3)$ are defined as $1 = \mathrm{X}'$, $2 = y$, $3 = z$. The angular coordinates of the rotor θ_1, θ_2, and θ_3 are rotations about 1, 2, and 3. $(1, 2, 3)$ are not orthogonal and 2 and 3 rotate but 1 does not.

The six dynamical coordinates we will use are X, Y, and Z, the components of $\vec{R}_{cm}$ in the $(\mathrm{X}, \mathrm{Y}, \mathrm{Z})$ frame, and the rotations θ_1, θ_2, and θ_3. The coordinates $(\theta_1, \theta_2, \theta_3)$ are not Euler angles but have the advantage that we may approximate the equations of motion by taking θ_1 and θ_2 to be infinitesimal. To begin we write the (x, y, z) components of the rotor's angular velocity:

$$\begin{aligned} \omega_x &= \dot{\theta}_1 \cos\theta_2, \\ \omega_y &= \dot{\theta}_2, \\ \omega_z &= \dot{\theta}_3 + \dot{\theta}_1 \sin\theta_2. \end{aligned} \tag{8.12}$$

Since (x, y, z) are principal axes, we may easily write these components of the

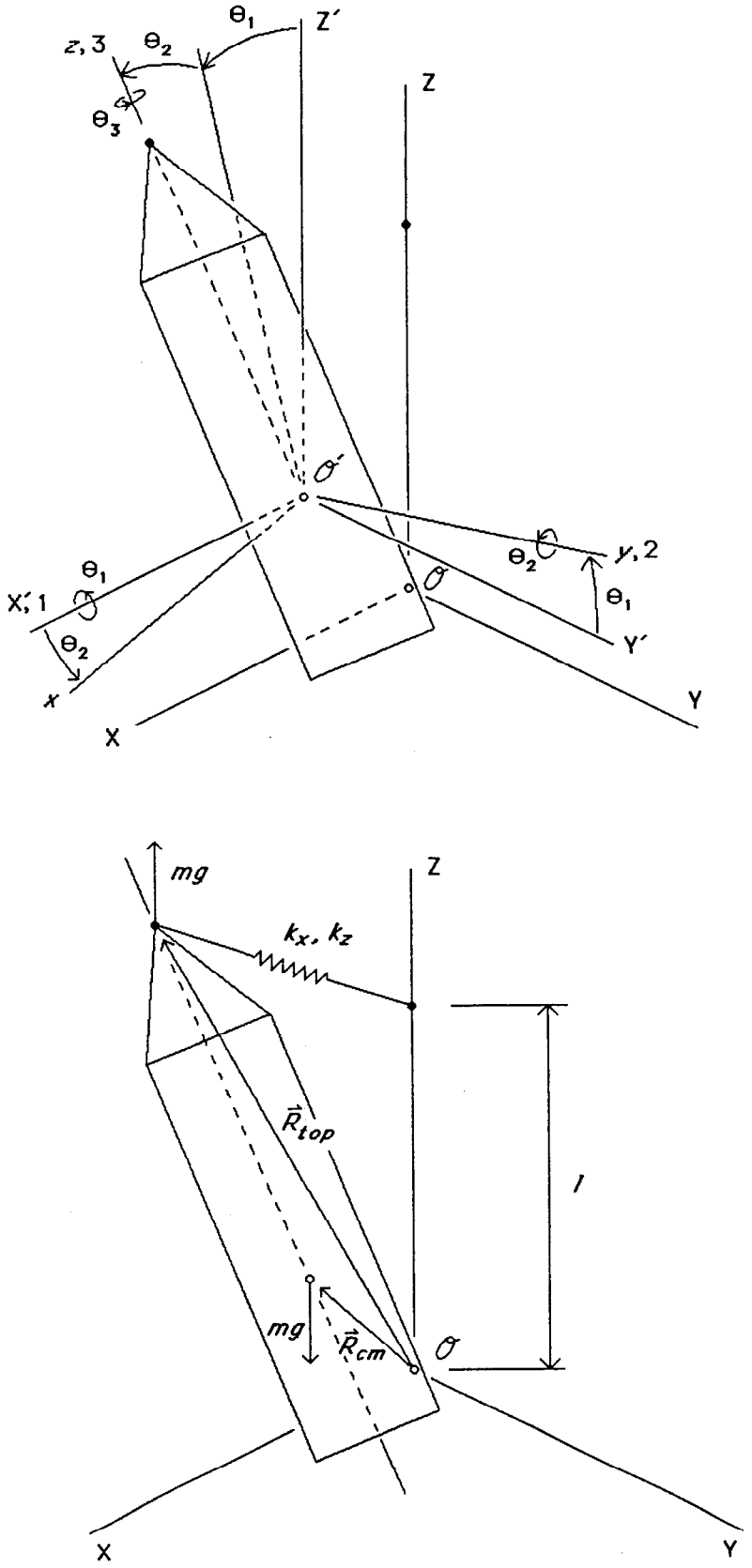

Figure 8.3. Coordinate Systems

angular momentum:

$$\begin{aligned} L_x &= I_x \dot{\theta}_1 \cos\theta_2, \\ L_y &= I_x \dot{\theta}_2, \\ L_z &= I_z(\dot{\theta}_3 + \dot{\theta}_1 \sin\theta_2). \end{aligned} \tag{8.13}$$

Next we project the angular momentum onto the $(1,2,3)$ axes:

$$\begin{aligned} L_1 &= L_x \cos\theta_2 + L_z \sin\theta_2 \\ &= I_x \dot{\theta}_1 \cos^2\theta_2 + I_z(\dot{\theta}_3 + \dot{\theta}_1 \sin\theta_2)\sin\theta_2, \\ L_2 &= L_y, \\ L_3 &= L_z. \end{aligned} \tag{8.14}$$

The inertial time rate of change of the angular momentum may then be calculated:

$$\begin{aligned} \dot{L}_1 &= \frac{\partial}{\partial t}(L_x \cos\theta_2) + \frac{\partial}{\partial t}(L_z \sin\theta_2), \\ \dot{L}_2 &= \frac{\partial}{\partial t}(L_y) + \dot{\theta}_1(L_x \sin\theta_2 - L_z \cos\theta_2), \\ \dot{L}_3 &= \frac{\partial}{\partial t}(L_z) + \dot{\theta}_1 L_y \cos\theta_2 - \dot{\theta}_2 L_x. \end{aligned} \tag{8.15}$$

Now we must calculate the applied torque and force. The $(\mathrm{X}, \mathrm{Y}, \mathrm{Z})$ components of $\vec{R}_{top}$ are given by:

$$\begin{aligned} R_X &= X + l\sin\theta_2, \\ R_Y &= Y - l\sin\theta_1\cos\theta_2, \\ R_Z &= Z + l\cos\theta_1\cos\theta_2, \end{aligned} \tag{8.16}$$

so that the $(\mathrm{X}, \mathrm{Y}, \mathrm{Z})$ components of the total force $\vec{F}$ applied at the top of the rotor

become:

$$\begin{aligned} F_X &= -k_x(X + l\sin\theta_2), \\ F_Y &= -k_x(Y - l\sin\theta_1\cos\theta_2), \\ F_Z &= -k_z(Z + l\cos\theta_1\cos\theta_2 - l) + mg. \end{aligned} \tag{8.17}$$

The torque about the center of mass is obtained from $\vec{N} = \vec{R}'\times\vec{F}$ where $\vec{R}' \equiv \vec{R}_{top} - \vec{R}_{cm}$. Using the above components of F_X and $R'_X = R_X - X$ *etc.*, one may get the (X, Y, Z) components of $\vec{N}$, which may be projected onto the (1, 2, 3) axes:

$$\begin{aligned} N_1 &= N_X, \\ N_2 &= N_Y\cos\theta_1, \\ N_3 &= N_Z\sin\theta_2 - N_Y\sin\theta_1\cos\theta_2. \end{aligned} \tag{8.18}$$

We now have all of the ingredients to write the six exact equations of motion of the system:

$$\begin{aligned} \dot{L}_1 &= N_1, & F_X &= m\ddot{X}, \\ \dot{L}_2 &= N_2, & F_Y &= m\ddot{Y}, \\ \dot{L}_3 &= N_3, & F_Z - mg &= m\ddot{Z}, \end{aligned} \tag{8.19}$$

where in the last equation we have included the force of gravity acting on the center

of mass. The three torque equations (divided by I_x) are:

$$
\begin{aligned}
&2\frac{I_z - I_x}{I_x}\sin\theta_2\cos\theta_2\dot{\theta}_1\dot{\theta}_2 + \frac{I_z}{I_x}\cos\theta_2\dot{\theta}_2\dot{\theta}_3 \\
&+ (\cos^2\theta_2 + \frac{I_z}{I_x}\sin^2\theta_2)\ddot{\theta}_1 + \frac{I_z}{I_x}\sin\theta_2\ddot{\theta}_3 = \\
&\qquad + \frac{k_z l^2}{I_x}\sin\theta_1\cos\theta_2(Z/l + \cos\theta_1\cos\theta_2 - 1 - \frac{mg}{k_z l}) \\
&\qquad + \frac{k_x l^2}{I_x}\cos\theta_1\cos\theta_2(Y/l - \sin\theta_1\cos\theta_2),
\end{aligned}
$$

$$
\begin{aligned}
&-\frac{I_z - I_x}{I_x}\sin\theta_2\cos\theta_2\dot{\theta}_1^2 - \frac{I_z}{I_x}\cos\theta_2\dot{\theta}_1\dot{\theta}_3 + \ddot{\theta}_2 = \\
&\qquad + \frac{k_z l^2}{I_x}\cos\theta_1\sin\theta_2(Z/l + \cos\theta_1\cos\theta_2 - 1 - \frac{mg}{k_z l}) \\
&\qquad - \frac{k_x l^2}{I_x}\cos^2\theta_1\cos\theta_2(X/l + \sin\theta_2),
\end{aligned}
\tag{8.20}
$$

$$
\begin{aligned}
&\frac{I_z}{I_x}\cos\theta_2\dot{\theta}_1\dot{\theta}_2 + \frac{I_z}{I_x}\sin\theta_2\ddot{\theta}_1 + \frac{I_z}{I_x}\ddot{\theta}_3 = \\
&\qquad + \frac{k_x l^2}{I_x}\cos\theta_1\cos\theta_2(\sin\theta_1\cos\theta_2(X/l) + \sin\theta_2(Y/l)).
\end{aligned}
$$

The three force equations (divided by ml) are:

$$
\begin{aligned}
\ddot{X}/l &= \frac{-k_x}{m}(X/l + \sin\theta_2), \\
\ddot{Y}/l &= \frac{-k_x}{m}(Y/l - \sin\theta_1\cos\theta_2), \\
\ddot{Z}/l &= \frac{-k_z}{m}(Z/l + \cos\theta_1\cos\theta_2 - 1).
\end{aligned}
\tag{8.21}
$$

All terms now have dimensions (frequency)^2.

This system of equations may be linearized by considering only those motions

for which the rotor is nearly vertical. We will assume:

$$\begin{aligned} \theta_1, \theta_2, X/l, Y/l, Z/l &\sim O(\delta), \\ \dot{\omega} &\sim O(\delta^2), \end{aligned} \tag{8.22}$$

where we have defined $\omega = \dot{\theta}_3$ (the spin speed), and δ is an infinitesimal angle. These conditions lead to the six equations:

$$O(\delta): \quad \omega_w \dot{\theta}_2 + \ddot{\theta}_1 = \omega_x^2 \cdot Y/l - \omega_*^2 \theta_1, \tag{8.23}$$

$$O(\delta): \quad \omega_w \dot{\theta}_1 - \ddot{\theta}_2 = \omega_x^2 \cdot X/l + \omega_*^2 \theta_2, \tag{8.24}$$

$$O(\delta^2): \quad \frac{I_z}{I_x}(\dot{\theta}_1 \dot{\theta}_2 + \theta_2 \ddot{\theta}_1 + \dot{\omega}) = \omega_x^2(\theta_1 \cdot X/l + \theta_2 \cdot Y/l), \tag{8.25}$$

$$O(\delta): \quad \ddot{X}/l = -\alpha\omega_x^2(X/l + \theta_2), \tag{8.26}$$

$$O(\delta): \quad \ddot{Y}/l = -\alpha\omega_x^2(Y/l - \theta_1), \tag{8.27}$$

$$O(\delta): \quad \ddot{Z}/l = -\alpha\omega_z^2(Z/l), \tag{8.28}$$

where we have defined:

$$\begin{aligned}
\omega_w &\equiv \frac{I_z \omega}{I_x}, \\
\omega_x^2 &\equiv \frac{1}{\alpha}\frac{k_x}{m}, \\
\omega_z^2 &\equiv \frac{1}{\alpha}\frac{k_z}{m}, \\
\omega_g &\equiv \frac{mgl}{\omega I_z}, \\
\omega_*^2 &\equiv \omega_x^2 + \omega_g \omega_w, \\
\alpha &\equiv \frac{I_x}{ml^2}.
\end{aligned} \tag{8.29}$$

Equation 8.28 shows that the vertical motion is completely decoupled to this order. The vertical oscillations at the frequency $(k_z/m)^{1/2}$ are controlled by the active magnetic suspension and were discussed in section 6.2. Here we discuss only the horizontal motions.

Equations 8.23, 8.24, 8.26, and 8.27 are a set of four coupled linear differential equations for the four variables θ_1, θ_2, X/l, and Y/l. These will be used to find four normal modes. Equation 8.25 shows that the assumption $\dot{\omega} \sim O(\delta^2)$ is consistent with $\theta_1, \theta_2, X/l, Y/l \sim O(\delta)$. Once θ_1, θ_2, X/l, Y/l, are known, Eqn. 8.25 may be used to solve for $\dot{\omega}$, but this is of no interest in what follows. To find the normal modes we may substitute:

$$\begin{aligned}
\theta_1 &= \delta e^{i\kappa t}, \\
\theta_2 &= i\delta e^{i\kappa t}, \\
X/l &= \epsilon e^{i\kappa t}, \\
Y/l &= i\epsilon e^{i\kappa t}.
\end{aligned} \tag{8.30}$$

The four equations then become algebraic and may be combined to yield a quartic characteristic equation for the frequencies of the normal modes

$$0 = \kappa^4 + \underbrace{\omega_w}_{\alpha\omega^1}\kappa^3 - \underbrace{\left((\alpha+1)\omega_x^2 + \omega_g\omega_w\right)}_{\alpha\omega^0}\kappa^2 - \underbrace{\alpha\omega_x^2\omega_w}_{\alpha\omega^1}\kappa + \underbrace{\alpha\omega_x^2\omega_g\omega_w}_{\alpha\omega^0}. \tag{8.31}$$

For our purposes it will be sufficient to find the roots in the limit $\omega \longrightarrow \infty$. The dependence of the coefficients in the characteristic equation on ω is shown above. First we search for roots $\kappa \sim O(\omega^1)$. Lowest order in ω^{-1} is then ω^4 and so we get:

$$\begin{aligned} 0 &= \kappa^4 + \omega_w\kappa^3, \\ \kappa &= (-\omega_w, 0, 0, 0), \end{aligned} \tag{8.32}$$

and three of the roots are zero to this order. Next we try $\kappa \sim O(\omega^0)$. This gives $O(\omega^1)$ as the lowest order and so we get:

$$\begin{aligned} 0 &= \omega_w\kappa^3 - \alpha\omega_x^2\omega_w\kappa, \\ \kappa &= (-\omega_w, +\alpha^{1/2}\omega_x, -\alpha^{1/2}\omega_x, 0), \end{aligned} \tag{8.33}$$

with one root still zero to this order. Note that we have not shown the $O(\omega^0)$ corrections to the first root. Finally we try $\kappa \sim O(\omega^{-1})$ and find:

$$\begin{aligned} 0 &= -\alpha\omega_x^2\omega_w\kappa + \alpha\omega_x^2\omega_g\omega_w, \\ \kappa &= (-\omega_w, +\alpha^{1/2}\omega_x, -\alpha^{1/2}\omega_x, \omega_g). \end{aligned} \tag{8.34}$$

These are the four normal mode frequencies, each given only to lowest order in ω^{-1}. Before we discuss the various modes in detail note that because the values

$$\omega_w : \omega_x : \omega_g = 42 : 4 : .17 \tag{8.35}$$

hold in practice the corrections to the normal mode frequencies will be small and the $\omega \longrightarrow \infty$ limit is a good approximation.

We first examine the solution $\kappa = -\omega_w$. It is simplest to go back to the linearized differential equations. We will assume $\omega_g = 0$, $\theta \sim O(\delta)$, $\kappa = \omega_w + O(\omega_x)$, and $\frac{d}{dt} \sim O(\omega_w + \omega_x)$. $O(\omega_x)$ is taken as the correction to κ since it is the largest term that may be present. Equation 8.26 then implies

$$X/l \sim O\left(\delta \frac{\omega_x^2}{\omega_w^2}\right), \tag{8.36}$$

and using this fact in Eqn. 8.23 and Eqn. 8.24 gives:

$$\begin{aligned} \omega_w \dot{\theta}_2 + \ddot{\theta}_1 &= 0, \\ \omega_w \dot{\theta}_1 - \ddot{\theta}_2 &= 0. \end{aligned} \tag{8.37}$$

The solution is:

$$\begin{aligned} \theta_1 &= \delta \cos \omega_w t, \\ \theta_2 &= \delta \sin \omega_w t. \end{aligned} \tag{8.38}$$

Recalling the meaning of the coordinates one sees that the top of the rotor moves in a circle of radius δl in the same direction as the rotor rotates, while the center of mass is almost stationary because of Eqn. 8.36. This motion is called the "forward whirl" and has definitely been observed in our system. For the present rotor the whirl appears if the speed is brought up to 1000 Hz but decays away again with about a 5 minute time constant if the speed is reduced to 900 Hz. Some

observed frequencies are:

$$\begin{aligned} \omega/2\pi &= 945.6\,\text{Hz}, \quad \omega_w/2\pi = 44.25\,\text{Hz}, \\ &897.2\,\text{Hz}, \qquad\quad 42.00\,\text{Hz}. \end{aligned} \tag{8.39}$$

The whirl frequency is seen to be proportional to the rotation frequency with $\omega/\omega_w = 21.4$, which should be equal to I_x/I_z, since according to the theory $\omega_w \equiv (I_z/I_x)\omega$. The moments of inertia have been measured by making a torsion pendulum of the rotor. The results are (accurate to 5%):

$$\begin{aligned} I_x &= 1530\,\text{g}\cdot\text{cm}^2, \\ I_z &= 69.6\,\text{g}\cdot\text{cm}^2. \end{aligned} \tag{8.40}$$

The measured I_x/I_z is thus 22.0, in agreement with the observed value of ω/ω_w.

The damping and driving of the forward whirl are important issues which will be discussed in the next section. For the moment note that if the top of the rotor is subject to a viscous drag $\eta \sim$ force/velocity then the equations of motion for this mode become:

$$\begin{aligned} \omega_w\dot{\theta}_2 + \ddot{\theta}_1 &= -\frac{\eta l^2}{I_x}\dot{\theta}_1, \\ \omega_w\dot{\theta}_1 - \ddot{\theta}_2 &= -\frac{\eta l^2}{I_x}\dot{\theta}_2, \end{aligned} \tag{8.41}$$

and the solutions are now damped exponentials with a damping time constant $\tau_w = I_x/\eta l^2$.

To investigate the motion with $\kappa = \pm\alpha^{1/2}\omega_x$ we again go back to the linearized equations and assume $\omega_g = 0$, $X/l, Y/l \sim O(\delta)$, $\kappa = \pm\alpha^{1/2}\omega_x + O(\omega_x^2/\omega_w)$, and

$\frac{d}{dt} \sim O(\omega_x + \omega_x^2/\omega_w)$. These conditions in Eqn. 8.23 imply

$$\theta_1, \theta_2 \sim O(\frac{\delta\omega_x}{\omega_w}), \tag{8.42}$$

and Eqn. 8.26 and Eqn. 8.27 reduce to

$$\begin{aligned} k_x/m \cdot X/l &= \ddot{X}/l, \\ k_x/m \cdot Y/l &= \ddot{Y}/l, \end{aligned} \tag{8.43}$$

so that this mode has the rotor nearly vertical and executing horizontal simple harmonic motion at the frequency $(k_x/m)^{1/2}$ (about $2\pi \cdot 4$ Hz in our device). Again the introduction of viscous damping η will lead to exponential decay of the motion, now with a time constant $\tau_x = m/\eta$. This mode cannot be observed in the instrument because it is well damped by the oil bath.

Finally we investigate the $\kappa = \omega_g$ solution. Returning to the linearized equations with the assumptions $X/l, Y/l, \theta_1, \theta_2 \sim O(\delta)$, $\kappa = \omega_g + O(\omega_g^2/\omega_x)$, and $\frac{d}{dt} \sim O(\omega_g)$, Eqn. 8.26 and Eqn. 8.27 can be used to show:

$$\begin{aligned} X/l + \theta_2 &\sim O(\frac{\delta\omega_g^2}{\omega_x^2}), \\ Y/l - \theta_1 &\sim O(\frac{\delta\omega_g^2}{\omega_x^2}). \end{aligned} \tag{8.44}$$

Using this in Eqn. 8.23 and Eqn. 8.24 now gives:

$$\begin{aligned} \dot{\theta}_2 &= -\omega_g\theta_1, \\ \dot{\theta}_1 &= +\omega_g\theta_2. \end{aligned} \tag{8.45}$$

The solutions are:

$$\theta_1 = \delta \sin \omega_g t, \qquad \theta_2 = \delta \cos \omega_g t. \tag{8.46}$$

Thus the bottom of the rotor moves in a circle of radius δl in a direction opposite to the direction of rotation, while the top is almost stationary. This very slow motion is called the gravitational precession and should occur at the frequency $mgl/\omega I_z = 2\pi \cdot .168\,\text{Hz}$ for $\omega = 2\pi \cdot 900\,\text{Hz}$, $l = 7.6\,\text{cm}$, and $m = 55.6\,\text{g}$. The gravitational precession is observed in the device after spin-up because the rotor is pulled about $100\,\mu\text{m}$ off axis by the driving coils. The observed frequency when the rotor spins at 900 Hz is .165 Hz, in agreement with the theory, and it has been observed that the frequency is proportional to the spin speed.

A calculation of the damping time constant for this mode when viscous drag is applied to the top of the rotor requires an analysis of higher order in ω^{-1}, since to lowest order the top of the rotor is stationary and so the mode cannot be damped in this way. Because of this one might expect the mode to be poorly damped; in practice the gravitational precession was found to have a time constant of several hours and so it was necessary to add active damping to bring the motion under control more quickly.

8.3.2 Damping of the Forward Whirl

In early studies of magnetically levitated spherical steel rotors, several workers discovered that above a threshold speed the rotors tended to develop a horizontal instability (76). The only transverse normal mode for a spherical rotor is the one

at the frequency $(k_x/m)^{1/2}$, for which the spin axis remains vertical and the rotor executes horizontal oscillations against the magnet spring constant just as it would if it were not spinning. Above the threshold speed it was found that the spheres would begin to move in a circle at the frequency $(k_x/m)^{1/2}$ with steadily increasing radius. The spiral motion could be eliminated by adding sufficient horizontal damping.

A possible explanation of the effect was given by Vladimirskii and Kalebin (77) who showed how eddy currents generated when the sphere is moved off the magnetic axis produce a force that can drive the spiral motion.

Our more complicated system also has a normal mode $(k_x/m)^{1/2} = 4\,\mathrm{Hz}$, but it is very well damped and no instability has been observed. Unfortunately the system has in addition the forward whirl mode at $\omega_w = \omega/22 = 42\,\mathrm{Hz}$ and a threshold for instability in this mode has been observed. In the mechanism of Vladimirskii and Kalebin the eddy current driving force increases as the rotor spins faster, while the damping of the whirl mode in our system is expected to decrease at high speeds because of the mass of the magnet. Evidently at some high enough speed the driving force exceeds the damping and the rotor begins to whirl. Below we will combine the mechanism of Vladimirskii and Kalebin with a simple model of the damping and with the gyrodynamics of the previous section to calculate the threshold speed for the onset of whirl.

Vladimirskii and Kalebin do an exact calculation for the idealized case of a sphere spinning in the field of an isolated magnetic pole. They develop their results as a power series in a/b, as defined in Fig. 8.4. We will consider only lowest order

which amounts to considering only the magnetic dipole moment of the spinning part. Our calculation will be crude because the complications of the true geometry (see Fig. 6.7) will be ignored. We will set $a = .5\,\text{cm}$ and $b = 1\,\text{cm}$. Using the gaussian cgs system, the magnetic charge q of the isolated pole is expressed as gauss $\cdot\,\text{cm}^2$. Since the magnetic field generated by our magnet is about $1 \cdot 10^3$ gauss we may take $q = 4\pi \cdot (1\,\text{cm})^2 \cdot 10^3\,\text{gauss} \sim 10^4\,\text{gauss} \cdot \text{cm}^2$.

These parameters may now be used in Vladimirskii and Kalebin's expression for the driving force. To give the reader an understanding of the origins of the force we will make a simple derivation, omitting all numerical factors and not fully justifying the approximations. Skeptics may consult the paper.

The radial component of the magnetic field applied to the ball is

$$B_r = \frac{q}{b^2}\phi, \tag{8.47}$$

where ϕ is given in Fig. 8.4. This field generates an apparent electric field on the moving surface of the ball of magnitude

$$E = \frac{v}{c}B_r, \tag{8.48}$$

where $v = \omega a$ is the surface velocity and c is the speed of light. For the geometry shown in the diagram the electric field points upwards on the right side of the ball and downwards on the left, assuming the magnetic charge is positive so that the radial magnetic field points outwards from the vertical axis. The electric field will generate a current flowing counter-clockwise around the circumference of the ball

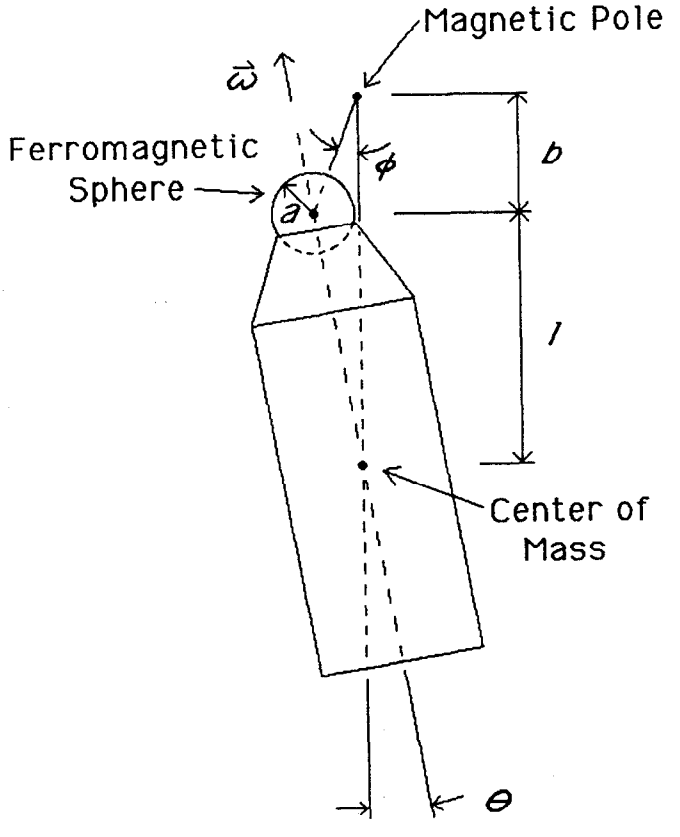

Figure 8.4. Geometry for Calculation of the Driving Force

in the plane of the figure. The current flows only in a region a distance D from the surface, where D is the skin depth

$$D = c/(2\pi\mu\sigma\omega)^{1/2}. \tag{8.49}$$

In the above μ is the relative permeability and σ is the conductivity. The current density $\vec{J}$ in the skin region is given by Ohm's law, $\vec{J} = \sigma\vec{E}$, and the total current I is given by $I = AJ$ where A is the cross-sectional area of the current carrying region. As a crude approximation, we will take $A = Da$.

The current I generates a magnetic moment pointed out of the plane of the figure of magnitude $m = (I/c)S$, where S is the area of the current loop. Letting $S = a^2$, we may use the above relations to obtain

$$m = \phi q \frac{a^4}{b^2}\frac{1}{\mu D}. \tag{8.50}$$

This magnetic dipole will experience a force

$$\begin{aligned} F_{drive} &= m\frac{q}{b^3} \\ &= \phi q^2 \frac{a^4}{b^5}\frac{1}{\mu D}, \end{aligned} \tag{8.51}$$

due to the magnetic pole. The direction of the force is out of the plane of the figure as may be seen by representing the magnetic dipole as a + charge above the plane of the figure and a − charge below; then the + magnetic pole tends to push the dipole up out of the plane. It is crucial to note that this force is in the same direction as the *forward* whirl motion. It can therefore make the mode unstable. The result of

Eqn. 8.51 is the same as given in Vladimirskii and Kalebin's paper, but they have a numerical factor of $3/2$ and terms of higher order in a/b.

In the previous section it was shown that if a viscous drag η is applied to the top of the rotor then the whirl motion is damped (in the absence of a driving force). The viscous drag applied by the oil to the *magnet* has been measured to be about $\eta' = 1000\,\text{dyne}/(\text{cm/sec})$ ($\pm 50\%$). To calculate the drag on the rotor we note that when the top of the rotor whirls at a radius r_{rotor} it applies a force $k_x r_{rotor}$ to the magnet, resulting in a circular motion of the magnet of radius

$$r_{magnet} = \frac{k_x r_{rotor}}{m_m \omega_w^2}, \tag{8.52}$$

where m_m is 26 g, the magnet mass. The power going into the oil must be equal to the power supplied by the rotor so that

$$\eta'(\omega_w r_{magnet})^2 = \eta(\omega_w r_{rotor})^2, \tag{8.53}$$

where η is the drag coefficient seen by the rotor. Thus

$$\eta = \eta' \left(\frac{r_{magnet}}{r_{rotor}}\right)^2 = \eta' \left(\frac{k_x}{m_m \omega_w^2}\right)^2. \tag{8.54}$$

Defining $\omega_m \equiv (k_x/m_m)^{1/2} = 2\pi \cdot 6\,\text{Hz}$ we have

$$\eta = \eta' \left(\frac{\omega_m}{\omega_w}\right)^4. \tag{8.55}$$

The driving force is proportional to $\omega^{1/2}$ (since $D \propto \omega^{-1/2}$) while the damping

force

$$F_{damp} = \phi b \omega_w \eta, \tag{8.56}$$

is proportional to ω^{-3} ($\phi b \omega_w$ is the velocity of the top of the rotor). At some high enough spin speed the driving force will exceed the damping force and the rotor will begin to whirl. The condition $F_{damp} = F_{drive}$ implies that the value for the spin speed where the rotor just becomes unstable is

$$\omega_{threshold} = \eta'^{2/7} \omega_m^{8/7} \left(\frac{I_x}{I_z}\right)^{6/7} \frac{c^{2/7}}{q^{4/7}} \left(\frac{\mu}{2\pi\sigma}\right)^{1/7} \frac{b^{12/7}}{a^{8/7}}. \tag{8.57}$$

Substituting the parameters:

$$\begin{aligned} \eta' &= 1000\,\text{dyne}/(\text{cm/sec}), \\ \omega_m &= 2\pi \cdot 6\,\text{Hz}, \\ I_x/I_z &= 22, \\ c &= 3 \cdot 10^{10}\,\text{cm/sec}, \\ q &= 10^4\,\text{gauss} \cdot \text{cm}^2, \\ \mu &= 10^5, \\ \sigma &= 50\,\mu\Omega \cdot \text{cm} = 1.4 \cdot 10^{16}\,\text{sec}^{-1}, \\ b &= 1\,\text{cm}, \\ a &= .5\,\text{cm}, \end{aligned} \tag{8.58}$$

one finds $\omega_{threshold} = 2\pi \cdot 114\,\text{Hz}$. The values of μ and σ are for the alloy 4750 nickel iron bearing material. With this bearing the onset of instability is at 1000 Hz, a

factor of 10 higher than given by the calculation. Because of the extreme crudeness of our representation of the magnet-bearing geometry the disagreement is perhaps not surprising, but we can hardly claim to have proved that we have the right mechanism for the instability.

To better understand the situation direct measurements of the driving force were made. Several different bearings were mounted in an air motor and spun at 500 Hz with the magnet hung above as a pendulum. The magnet-bearing gap was set so that the magnetic attraction would be the same as in the apparatus. With the bearing spinning at 500 Hz a small horizontal deflection of the magnet could be measured, and from this one may calculate the horizontal force applied to the spinning bearing by the magnet. To get a measurable effect it was necessary to increase the angle ϕ to $\pi/2$, so the bearing rotation axis was made horizontal and the magnetic axis was vertical.

The results are shown in Table 8.2. The force F is calculated from $F = k_x\Delta$ where k_x (the transverse magnet-bearing spring constant) has the value $3.7 \cdot 10^4$ dyne/cm and Δ is the observed deflection. Data for the bearings from three different rotors is given. Rotor 1 was the first prototype polystyrene rotor. Its body had a slightly different shape and so its I_x/I_z was different. Because it began to whirl at 400 Hz, Rotor 2 was built with a bearing made of alloy 4750 nickel iron, which has higher permeability and lower conductivity than the 1018 cold

Table 8.2. Whirl Threshold Data. The first column gives the bearing material, 1018 cold rolled steel or alloy 4750 nickel iron. The second column is the measured force at 500 Hz and with $\phi = \pi/2$. $f_{thres.,calc.}$ is the value of $\omega_{threshold}/2\pi$ calculated from the measured force while $f_{thres.,obs.}$ is the observed value of $\omega_{threshold}/2\pi$. The ratio of the moments of inertia is in the last column.

	Bearing Material	F	$f_{thres.,calc.}$	$f_{thres.,obs.}$	I_x/I_z
Rotor 1	1018 steel	470 dynes	450 ± 100 Hz	400 ± 50 Hz	17.3
Rotor 2	4750 unannealed	380 dynes	590 ± 120 Hz	600 ± 50 Hz	22.0
Rotor 3	4750 annealed	160 dynes	760 ± 150 Hz	1000 ± 50 Hz	22.0

rolled steel used in the first rotor*. The new rotor's bearing had a measured force only slightly smaller than the 1018 steel bearing. Whirl set in at 600 Hz and the rotor hit the walls and was destroyed. Rotor 3 is the present rotor. It differs from Rotor 2 only in that the bearing piece was annealed after fabrication at 1150 °C for 10 minutes in a hydrogen furnace. This made an important improvement in the measured force and the observed whirl threshold increased to 1000 Hz, allowing routine operation at 900 Hz with no whirl.

Assuming that the driving force is given by

$$F_{drive} = F\phi \left(\frac{\omega}{2\pi \cdot 500\,\text{Hz}} \right)^{1/2}, \tag{8.59}$$

with F taking its measured value, we may make a partly empirical prediction of the

* Alloy 4750 stock was obtained from AeroMet Inc., 41 Smith Street, Englewood, N.J. 07631. This material is easy to machine and has as high a permeability as Mumetal at high fields.

whirl threshold using the earlier expression for the damping force

$$F_{damp} = \phi b \omega_w \eta' \left(\frac{\omega_m}{\omega_w}\right)^4. \tag{8.60}$$

Equating F_{damp} and F_{drive} gives

$$\omega_{threshold} = \frac{(2\pi \cdot 500\,\mathrm{Hz})^{1/7}}{F^{2/7}} b^{2/7} \eta'^{2/7} \omega_m^{8/7} \left(\frac{I_x}{I_z}\right)^{6/7}. \tag{8.61}$$

The predictions from this equation are given in the table next to the observed thresholds for each rotor. The errors shown come from uncertainties in the various measured parameters. The results agree rather well with the observed whirl thresholds.

Thus it seems that the measured driving force provides some understanding of the onset of whirl, but that our theory based on the calculation of Vladimirskii and Kalebin for the source of the driving force is poor. In fact the force predicted by Eqn. 8.51 is too high by a factor of about 1000. This does not necessarily mean that the eddy current mechanism is wrong, since the expression contains high powers of geometrical parameters that have been defined very crudely. If the mechanism is correct then since Eqn. 8.57 says that $\omega_{threshold} \propto \mu^{1/7}$, the annealing operation must have increased the permeability in the skin region by a factor $(1000/600)^7 = 36$ to account for the difference between Rotor 2 and Rotor 3. A different mechanism that might be generating the driving force would be magnetic hysteresis in the bearing; this possibility has not been investigated.

8.4 Design Summary

We now summarize the entire design process as discussed in this and the previous chapter. First of all, the sample size is chosen on physics grounds. This fixes the sample container size, as it must be deep enough to fully shield the sample's surface potential. The size of the pad structure then follows; too small and the coupling efficiency is poor, too large and there is unnecessary stray capacitance from pad to pad. The harmonic number is chosen high enough so that the motion sensitivity of the signal generated by surface potentials in the coupling capacitor gaps can be tolerated. Together with the pad size and spacing, the harmonic number fixes the rotor radius. The coupling capacitances must be large enough for good efficiency.

The FET noise properties show that the signal to noise ratio begins to degrade rapidly below about 6 kHz, but that only a 50% improvement is to be had in going from 8 kHz to 16 kHz. This fact combined with mechanical constraints, especially the requirement that the rotor be subcritical with respect to bending modes, led us to choose 8 kHz as the operating frequency. Polystyrene was chosen for the rotor material because of its high stiffness and excellent dielectric properties.

When the first prototype rotor was spun the forward whirl instability was discovered. The force that drives the instability could be measured and was decreased by a factor of three by switching to an annealed alloy 4750 nickel iron bearing piece. The whirl instability presently limits the operating frequency to 7.2 kHz.

9. Performance of the Instrument

In this chapter the performance of the instrument is described in three stages: first with no sample, then with a sample but without charge changes, and then finally with a sample and with charge changes. We begin by showing some data which demonstrates that the total noise with no sample installed is equal to the amplifier noise. The low frequency wanderings of the rotor's position are characterized next, because these become important once a sample is installed. Then the lessons learned with the seventeen samples tried so far are reviewed. The main results are a probable explanation of the source of the motion sensitivities and the discovery that they can be greatly reduced by the addition of a "guard" to the sample. Finally all the data from the most recent sample is discussed. A resolution of $1/3\,q_e$ is reliably achieved, but there is an important contribution to the total noise that remains unexplained. The calibration of the instrument is shown to be $4.7\,\mathrm{nV}/q_e$ by observing unit changes in the sample charge caused by photoemission.

9.1 No-sample Noise

Figure 9.1 shows a spectrum of the signal at the output of the lock-in amplifier with the rotor spinning at 900 Hz. For this data the photoelectric tachometer was used to lock the lock-in to 7.2 kHz so that the spectrum measures the noise in a band ±40 mHz about 7.2 kHz. For this spectrum and others to follow the data was taken with the lock-in time constant set to one second, so that there is no attenuation in the system at the frequencies that will be important, below about 20 mHz. A Hanning window is applied to each data segment before the Fourier transformation,

and a linear least squares fit is subtracted off each segment, which causes the lowest two frequency bins to be attenuated somewhat.

Not including the lowest two bins the average noise is $9.5 \pm .3\,\mathrm{nV}/\sqrt{\mathrm{Hz}}$. This is somewhat higher than the $8.3\,\mathrm{nV}/\sqrt{\mathrm{Hz}}$ amplifier noise given earlier for two reasons. First, when the FET was installed in the instrument the noise at the preamplifier output was measured to be $8.8\,\mathrm{nV}/\sqrt{\mathrm{Hz}}$. This small rise from the $8.3\,\mathrm{nV}/\sqrt{\mathrm{Hz}}$ value measured with a 2.8 pF dummy load is probably due to a small difference in the load capacitance. Secondly, when the spectrum in Fig. 9.1 was recorded the bandpass filter between the preamplifier and the lock-in amplifier had not yet been installed (a highpass filter only was used), so some noise from the odd harmonics of the signal frequency was included. All data to be presented later is with the bandpass filter, so we will take the total amplifier noise contribution to be $8.8\,\mathrm{nV}/\sqrt{\mathrm{Hz}}$.

There is no evidence in Fig. 9.1 for any extra contribution above the amplifier noise. Once a sample is installed this will no longer be true.

9.2 Rotor Motion

An important difficulty once a sample is installed is that the instrument is very sensitive to small motions of the sample relative to the rotor. It is therefore important to know how large the rotor motions are, and so spectra have been obtained for the motions in each of three directions: the vertical, radial, and tangential or phase direction.

9.2.1 Vertical Motion

This is the most well instrumented direction, since the magnetic suspension

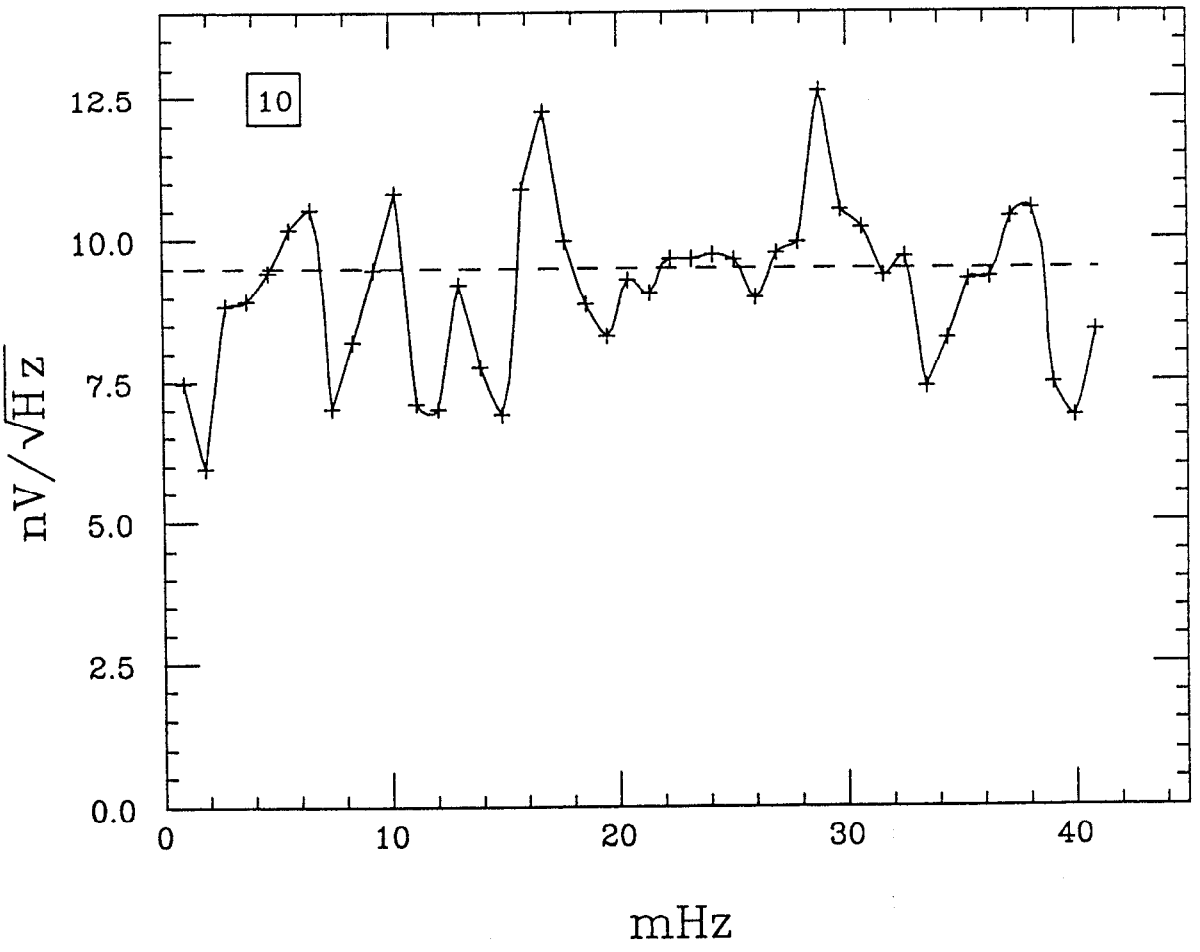

Figure 9.1. No-sample Noise. The average is $9.5 \pm .3\,\mathrm{nV}/\sqrt{\mathrm{Hz}}$. The boxed number is the number of segments n that the data was broken into to compute the spectral density. The statistical fluctuations are $1/(2n)^{1/2}$ and the time duration of the full data record is equal to n times the frequency bin size.

feedback circuit measures the vertical position of the rotor relative to the split photodiode, the 900 Hz signal measures the vertical position relative to the coupling capacitors, and with some samples the 7.2 kHz signal is very sensitive to the vertical position of the rotor relative to the sample. Figure 9.2 is a typical spectrum of the noise in the suspension feedback loop. The signal was taken from the output of the lowpass filter in the feedback loop (see Fig. 6.8) where the sensitivity is .5 μm/mV. Spectra taken simultaneously at the 900 Hz fundamental or at 7.2 kHz with certain samples installed are highly correlated with spectra of the feedback loop noise, and show that the correct calibration is actually 1 μm/ mV. Because the suspension loop gain is 2.0, this can be understood if the noise source is inside the feedback loop, between the rotor position and the lowpass filter output. The exact source of the noise has not been determined; it might be electronic or it might be due to motions of the light source, optics, or photodiode, or might even be due to the mirage effect (78). If mechanical motions are the cause then they could be due to thermal expansions; since aluminum has an expansion rate of $2 \cdot 10^{-5}$/°C and the typical distances are 10 cm, a thermal drift of about 1°C/1000 sec would be required.

Because spectra taken at 7.2 kHz with samples that have a large vertical motion sensitivity are highly correlated with spectra of the suspension feedback signal, we may take Fig. 9.2 to be a measurement of the vertical motion of the rotor relative to the sample.

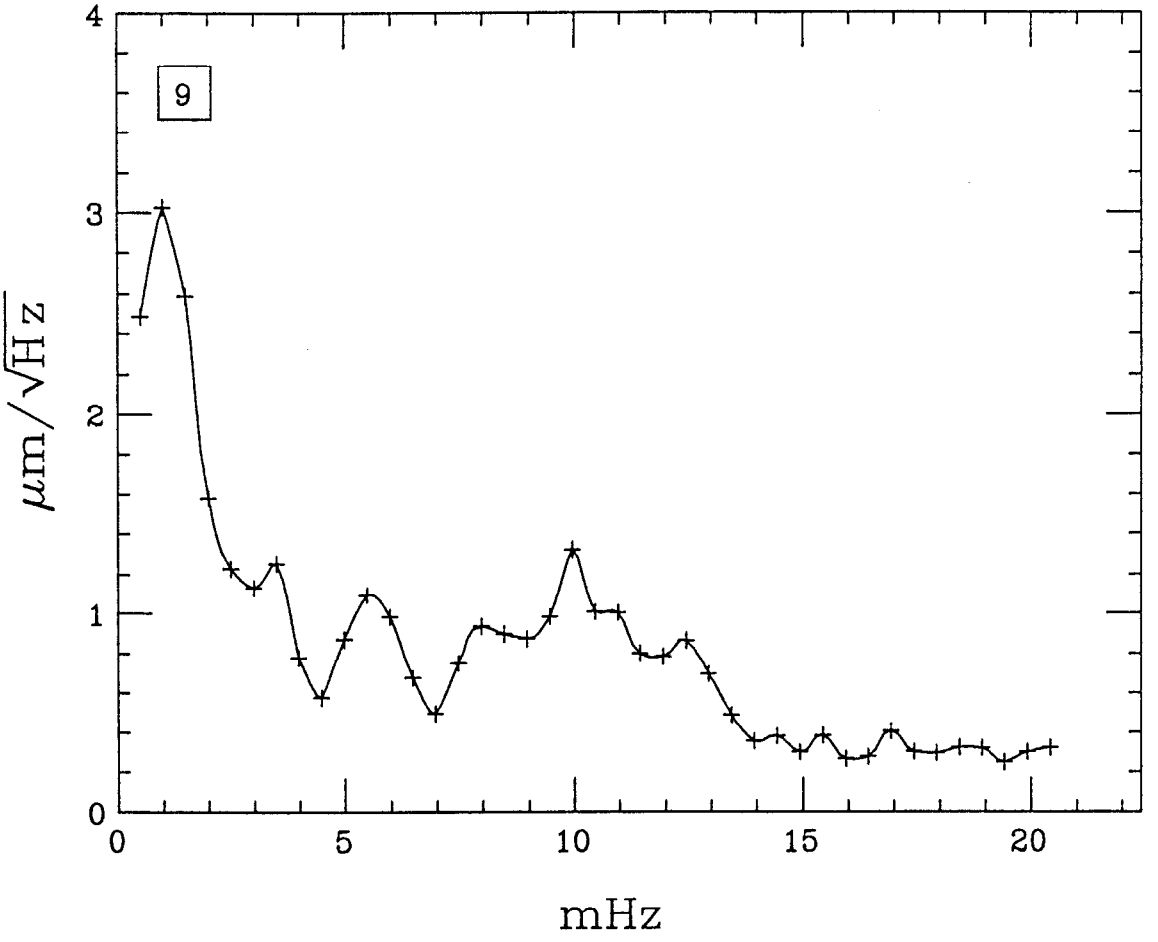

Figure 9.2. Vertical Motion Spectrum

9.2.2 Radial Motion

Figure 9.3 is a measure of the radial motion of the rotor relative to the sample. This spectrum was taken at 7.2 kHz with a sample installed that had a large radial motion sensitivity of 10.3 nV/μm and a smaller vertical motion sensitivity of 6.9 nV/μm. The dotted line shows the spectrum with the contributions from vertical motions, phase motions, and amplifier noise subtracted off.

Comparison with Fig. 9.2 shows that the radial motions are somewhat larger than the vertical ones. The radial motion might be due to thermal expansions or to floor motions. Thermal expansions seem to be the most likely cause of the radial motions, one piece of evidence being that they were improved by a factor of about three when a thick cloth shroud was placed over the instrument. The motions are also somewhat smaller at night, and after the instrument has been running for several hours. All the data in this chapter was taken at night or on weekends and after the rotor had been running for at least two hours, and with the shroud over the instrument.

9.2.3 Phase Motion

Motion of the sample tangential to the rotor will cause a phase shift of the 7.2 kHz signal, so this is called phase motion. It can be measured when there is a large signal in quadrature with the charge measuring signal and small vertical and radial motion sensitivities in-phase. Figure 9.4 gives a spectrum of the in-phase signal under such conditions with 28 μV in quadrature. For small motions the in-phase signal will change 28 μV per radian of motion, so the calibration here

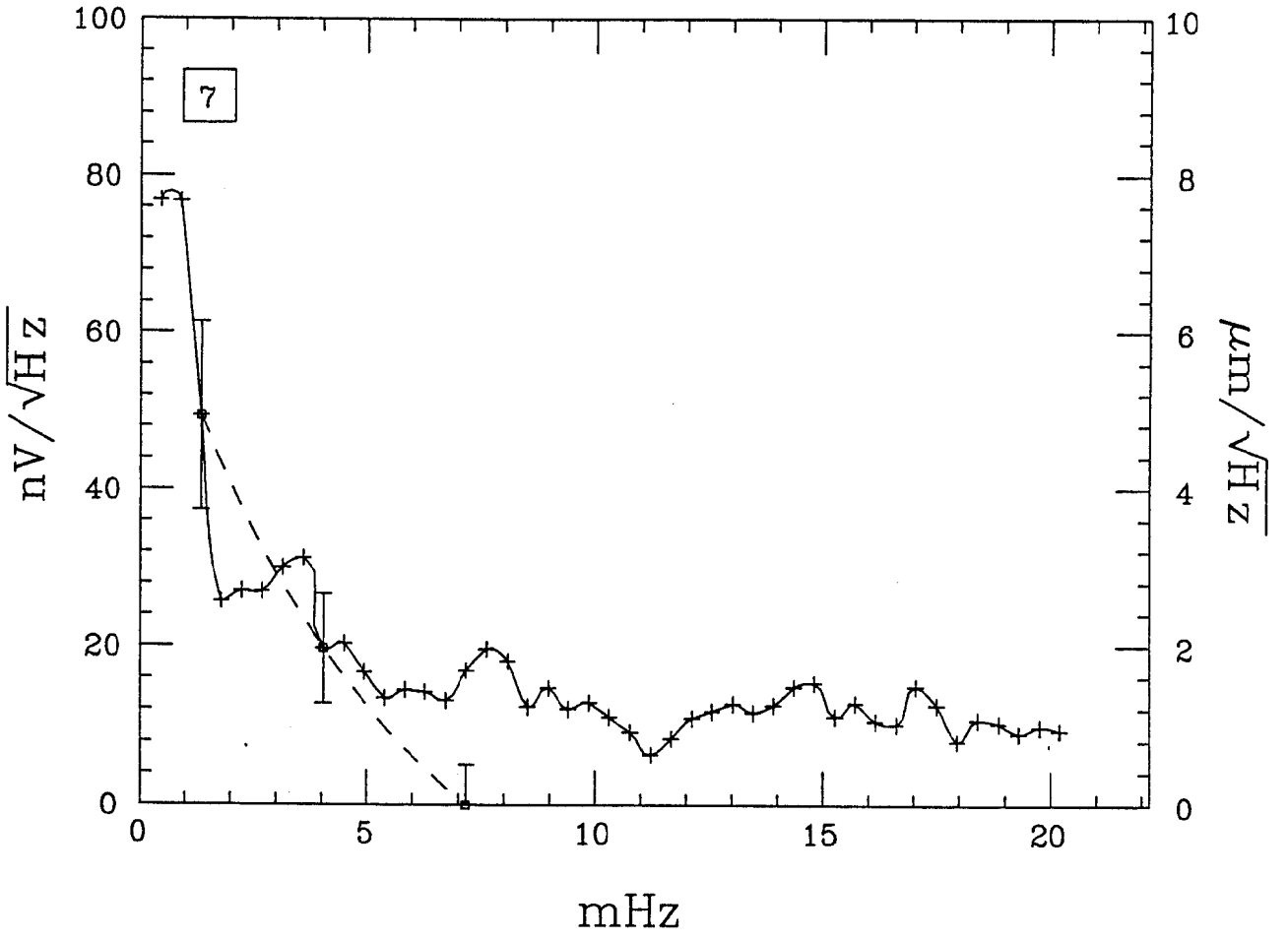

Figure 9.3. Radial Motion Spectrum

is 1 mR/28 nV. Since the distance between two signal pads is 11.96 mm and this is 2π radians of phase, there are 1.9 μm per milliradian. The dotted line shows the spectrum with the amplifier noise subtracted off.

The motions are seen to be about five times less than in the radial direction, which has also been seen in several other similar spectra. This seems somewhat hard to explain since in most respects the instrument is the same in the two horizontal directions. The chamber mounting is not symmetric however; flexure of the steel plate to which the chamber is bolted would tilt the instrument and cause purely radial motions, also the sample manipulator is not symmetric. Even if there is something being misunderstood here the motion spectra will still be reliable as upper bounds.

It should be noted that phase motion cannot be distinguished in this data from electronic phase noise, as would be caused by jitter of the lock-in phase relative to the rotor phase. This was an important problem before the output of the photoelectric tachometer was bandpass filtered (see Fig. 6.13). Figure 9.3 provides an upper bound on any remaining electronic phase noise in the system.

9.3 Properties of Samples

Seventeen different samples of various designs have been tried in the instrument so far. The main problem has been to make the motion sensitivity low enough so that the total noise is dominated by the amplifier noise and not by the motions. As will be discussed in more detail in the next section, if one wishes to average the output for 200 seconds, then it is necessary to have a vertical motion sensitivity

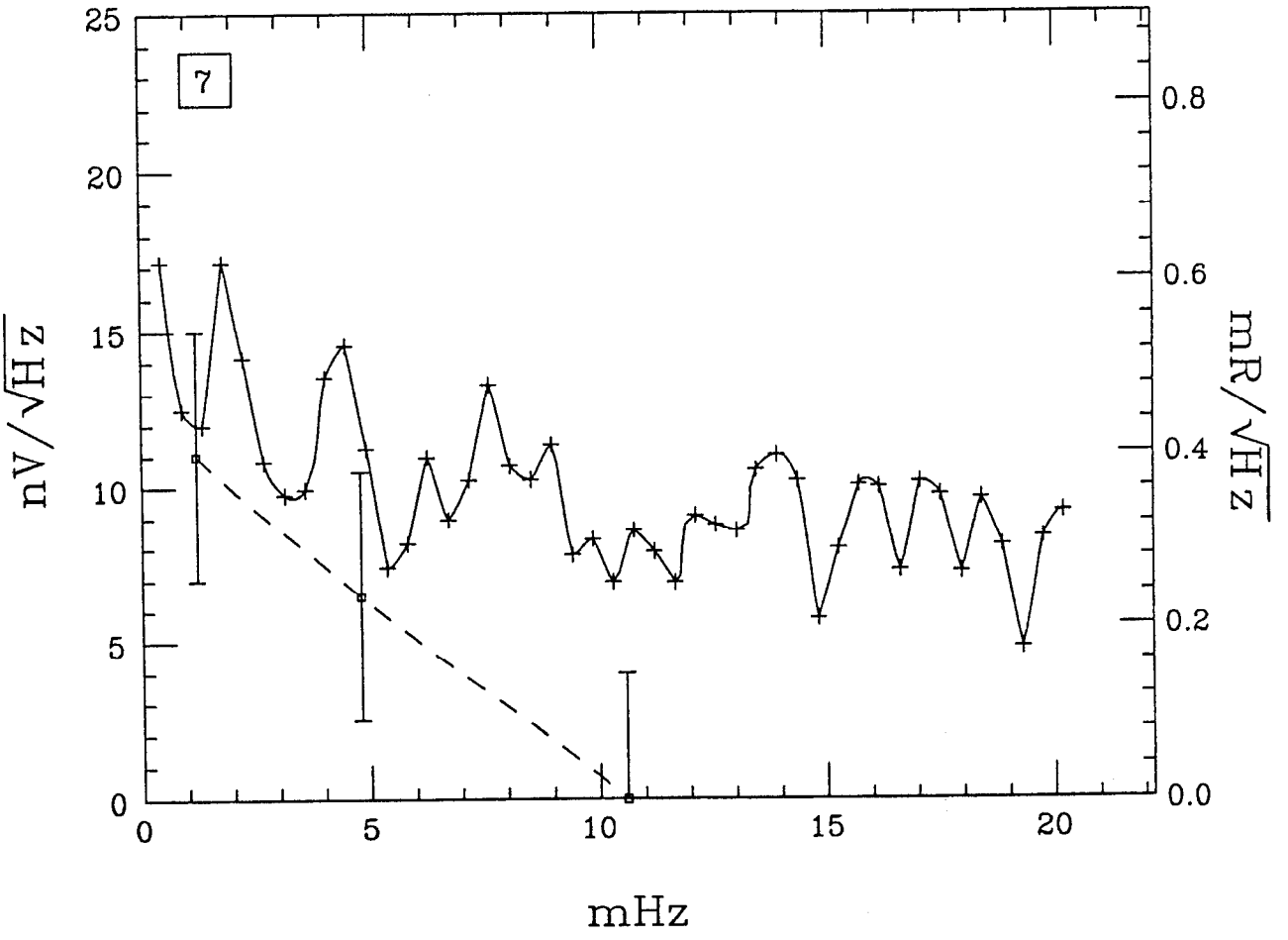

Figure 9.4. Phase Motion Spectrum

less that about $2\,\mathrm{nV}/\mu\mathrm{m}$, a radial sensitivity less than about $1\,\mathrm{nV}/\mu\mathrm{m}$, and a quadrature signal less than about $10\,\mu\mathrm{V}$. Another problem has been mechanical damping. Several of the samples have been useless because of undamped torsional or pendular modes. Below is a brief account of the behavior of each sample.

The first three samples tried were different than the design described earlier (Fig. 6.15). A $.5\,\mathrm{mm} \times .5\,\mathrm{mm} \times .2\,\mathrm{mm}$ indium sample was hung on a $5\,\mu\mathrm{m}$ diameter quartz fiber stretched horizontally tangential to the rotor. The motion sensitivities of the first samples were not measured but the first two had large quadrature signals. The quadrature signal was thought to be due to charge on the quartz fiber and several methods were tried to reduce it. Leaving the sample to sit in air for a few days was helpful, and a similar effect was observed when partly ionized dry nitrogen gas was passed through the chamber. This and later experience showed that flowing partly ionized nitrogen through the chamber at atmospheric pressure for 15 minutes when a new sample is installed has as beneficial an effect as any method, and is quick and not damaging to the vacuum. The nitrogen is ionized by a spark coil. We also tried introducing ionized and neutral water and alcohol vapor into the chamber, but these worked no better. The first time a sample is treated with ionized nitrogen a factor of 10 or 100 improvement is often seen in the quadrature signal and in the motion sensitivities, but subsequent treatments are less helpful. With the first two samples the smallest quadrature signals measured were $50\,\mu\mathrm{V}$ and $200\,\mu\mathrm{V}$. The third sample had a much smaller quadrature signal of about $10\,\mu\mathrm{V}$, but could not be studied further because of an undamped pendular

motion.

The next sample had a very thick 85 μm diameter fiber which could support the weight of the sample cantilevered, and so could be brought away from the rotor along a radius. The hope here was to reduce the quadrature signal by keeping the fiber charge all at the same phase as the sample. After treatment with ions a quadrature of 30 μV was achieved, but a very large drift of .2 q_e/sec was present, about 10 times worse than seen typically and about 400 times worse that seen at best. Perhaps this was due to the fiber having a very large surface area.

From this point on all samples were roughly of the design shown in Fig. 6.15, with a single vertical fiber, usually about 3 μm in diameter. With the exception of one very large sample these all had quadratures of less than 50 μV, often much less. This is thought to be because the fiber charge is all at the same phase. Samples from this point on are identified by capitol letters **A**–**O**.

Sample **A** had a large indium piece 2 mm × 3 mm × .2 mm and had the following vertical and radial motion sensitivities and quadrature signal:

$$\mathbf{A} \qquad V = 7\,\mathrm{nV}/\mu\mathrm{m}, \quad R = 14\,\mathrm{nV}/\mu\mathrm{m}, \quad Q = 30\,\mu\mathrm{V},$$

with the sample charge adjusted to null the in-phase signal. Here and below the motion sensitivities and quadrature signal are those measured after one or two ion treatments. This sample had an undamped torsional oscillation, which has been a recurring problem with the vertical fiber samples and seems to be worst when the sample has a large moment of inertia, the latex strip is too thick, or the fiber is

especially thin.

Sample **B** and **C** were just as in Fig. 6.15, and had

$$\mathbf{B} \qquad V = 7\,\mathrm{nV}/\mu\mathrm{m}, \quad R = 8\,\mathrm{nV}/\mu\mathrm{m}, \quad Q = 25\,\mu\mathrm{V},$$

$$\mathbf{C} \qquad V = 2\,\mathrm{nV}/\mu\mathrm{m}, \quad R = 7\,\mathrm{nV}/\mu\mathrm{m}, \quad Q = 8\,\mu\mathrm{V}.$$

Sample **C** might have been usable for noise studies, but it was not yet realized that the sample charge need not be adjusted to minimize the in-phase signal, but can instead be adjusted to null the radial motion sensitivity.

Sample **D** was broken on installation, and samples **E** and **F** had undamped torsion. Sample **G** began swinging during a liquid nitrogen trap fill and hit the rotor and was destroyed. Thereafter samples were always retracted before nitrogen fills.

Sample **H** and **I** were as in Fig. 6.15, and had

$$\mathbf{H} \qquad V = 30\,\mathrm{nV}/\mu\mathrm{m}, \quad R = 1\,\mathrm{nV}/\mu\mathrm{m}, \quad Q = 20\,\mu\mathrm{V},$$

$$\mathbf{I} \qquad V = 20\,\mathrm{nV}/\mu\mathrm{m}, \quad R = 1\,\mathrm{nV}/\mu\mathrm{m}, \quad Q = 1\,\mu\mathrm{V}.$$

Sample **I** was the first sample with small radial motion sensitivity and a small quadrature signal. Extensive noise studies were made and it was with this sample that it was found that the magnetic suspension feedback signal can be used to measure the vertical rotor motion. In fact it was found to be possible to use the vertical suspension feedback signal to subtract off most of the vertical motion noise

in the charge measuring signal, and in this way a charge resolution of less than $1\,q_e$ was achieved for the first time. Unfortunately because of the need to subtract off the vertical motion the interpretation of the measured total noise is somewhat complex and uncertain for this sample, so a detailed presentation of the data will not be given.

Some useful measurements of the sample coupling versus sample position were made with sample I. These allow a general understanding of the mechanism for the motion sensitivities. As the sample was moved radially away from the center of the pad region the signal strength was observed to drop off linearly at a rate of $6 \cdot 10^{-4}/\mu\mathrm{m}$, so that the signal had decreased by about half when the sample was moved a half of a pad width ($1150\,\mu\mathrm{m}$) away from the rotor. The measurement was made with a very large charge on the sample so one could be certain that the sample charge was the only important signal generating mechanism. This behavior seems very reasonable and implies that the radial motion sensitivity should change by $6 \cdot 10^{-4}\,\mu\mathrm{V}/\mu\mathrm{m} = .6\,\mathrm{nV}/\mu\mathrm{m}$ for a $1\,\mu\mathrm{V}$ ($= 200\,q_e$) change in the sample charge, if the motion sensitivity is due in part to a change in the sample coupling. This is just the observed change in the radial motion sensitivity for a change in the sample charge.

It then became clear that the radial motion sensitivity could be nulled by adjusting the sample charge, and this was done subsequently. Unfortunately the vertical motion sensitivity cannot be changed very much by adjusting the sample charge, since the coupling has a maximum along the vertical direction when the

position of the sample is near the center of the pad. Even if one were willing to operate with reduced coupling with the sample near the upper or lower edge of the pads, one could not independently null the vertical and radial motion sensitivities since there is only one degree of freedom, namely the sample charge. Also the quadrature signal cannot be nulled, since it is by definition orthogonal to the signal which changes as the sample charge changes.

Measurements of the change in coupling as the sample was moved vertically were also made. The coupling showed a maximum at the center of the pad, and with a sample to pad gap of 250 μm, had decreased to 74% of peak with the sample over the lower edge of the pads.

If one assumes that the vertical motion sensitivity is due entirely to charge on the fiber then the measured $20\,\mathrm{nV}/\mu\mathrm{m} = 4\,q_e/\mu\mathrm{m}$ motion sensitivity suggests that the fiber has an average charge of about $4\,q_e/\,\mu$m, since when the sample moves down 1 μm another 1 μm of fiber becomes coupled to the pads. This might explain the $\sim 100\,\mu$V quadrature signal seen with the samples that had a horizontal fiber tangential to the rotor, since with those samples $\sim$ 5 mm of the fiber was seen by the rotor ($20\,\mathrm{nV}/\mu\mathrm{m} \cdot 5\,\mathrm{mm} = 100\,\mu\mathrm{V}$). Another suggestive point is that one expects the ion treatment to leave the fiber with a charge of about $1\,q_e/\mu$m, since the fiber's capacitance is about

$$C = 2\pi\epsilon_0/\ln(500\,\mu\mathrm{m}/2\,\mu\mathrm{m}) \sim 10\,\mathrm{pF/m},$$

and if it were neutralized to the mean thermal potential of 25 mV then the charge

per unit length would be

$$Q = 10\,\mathrm{pF/m} \cdot 25\,\mathrm{mV} = 2.5 \cdot 10^{-13}\,\mathrm{C/m} \sim 1\,q_e/\mu\mathrm{m}.$$

Thus a consistent picture seems to be that the motion sensitivities are simply due to the change in coupling efficiency as the charges on the sample and fiber are moved relative to the pads.

The next sample (**J**) was a very large cylindrical can 4.4 mm high and 1.9 mm in diameter, roughly of the sort that we hope ultimately to use as a sample container. Although it was possible to null the radial motion sensitivity, the other sensitivities were very bad:

$$\mathbf{J} \qquad V = 170\,\mathrm{nV}/\mu\mathrm{m}, \quad R = 1\,\mathrm{nV}/\mu\mathrm{m}, \quad Q = 60\,\mu\mathrm{V}.$$

With this sample the signal had a very different appearance than with the smaller samples. As seen on an oscilloscope triggered on the 900 Hz fundamental, the signal generated by the pads was periodic at 900 Hz but not at 7.2 kHz; in fact the waveform generated varied from pad to pad in an irregular way. This seems to be strong evidence that a large part of the signal was being generated by the surface potentials of the pads, as this is the only feature of the pads which changes from pad to pad.

A possible mechanism can be understood by referring back to Fig. 7.3. To include the effects of the pad surface potentials, imagine including varying potentials of $\sim 30\,\mathrm{mV}$ rms in series with the sample to pad capacitances $c_S(t)$ and

$c_G(t)$. These potentials will generate a voltage at the amplifier input of roughly $30\,\mathrm{mV} \cdot c_G(t) \oplus c_S(t)/C$, where C is $C_{TB} + C_{IN} \sim 4\,\mathrm{pF}$, and $\oplus$ means series sum. In the model measurements discussed in Section 7.2, $c_G(t) \oplus c_S(t)$ was about .05 pF for all positions of the larger sample container, which is a good model for sample **J**. Thus one expects an rms signal of $30\,\mathrm{mV} \cdot (.05\,\mathrm{pF}/4\,\mathrm{pF}) = 400\,\mu\mathrm{V}$, which is about 10 times larger than the observed signals, but note that it is hard to know how much of the observed signal is being cancelled by the sample charge. The very large vertical motion sensitivity suggests that a signal of $\sim 170\,\mathrm{nV}/\mu\mathrm{m} \cdot 5\,\mathrm{mm} = 850\,\mu\mathrm{V}$ might be present (5 mm is the pad height).

Because of the experience with sample **J** we decided to abandon large samples for the time being. For small samples like the one in Fig. 6.15 c_S and c_G are 5 to 10 times smaller than for sample **J**. The pad surface potentials may still generate significant signals and motion sensitivities with the smaller samples but it has not been possible to separate these from the signals due the sample and fiber charges. With the small samples the signal always appears periodic at 7.2 kHz.

Samples **K**, **L**, **M**, and **N** were as in Fig. 6.15. **K** and **N** had undamped torsion while **L** and **M** had

$$\mathbf{L} \qquad V = 10\,\mathrm{nV}/\mu\mathrm{m}, \quad R \sim 1\,\mathrm{nV}/\mu\mathrm{m}, \quad Q = 2\,\mu\mathrm{V},$$

$$\mathbf{M} \qquad V = 12\,\mathrm{nV}/\mu\mathrm{m}, \quad R \sim 1\,\mathrm{nV}/\mu\mathrm{m}, \quad Q = 1\,\mu\mathrm{V}.$$

At this point it began to seem that we might never achieve small vertical motion sensitivity with this sample design since of six samples measured only one had a

vertical motion sensitivity of less than $7\,\mathrm{nV}/\mu\mathrm{m}$.

We therefore decided to try a new sample design, identical to Fig. 6.15 except with an additional small indium piece, called the guard, pinched onto the fiber 4.5 mm above the sample. The guard is placed 2 mm above the upper edge of the pads where the coupling is reduced considerably, but where it has a large dependence on the vertical position. It was hoped that the charge of the guard could be used to null the vertical position sensitivity. So long as the guard charge and the sample charge do not both effect the vertical and radial sensitivity in the same way it should be possible to null both the vertical and radial sensitivity.

Sample **N** was the first guarded sample; it had undamped torsion and was useless. Sample **O** is the most recent sample tried in the instrument and has been very successful. The indium sample measures 1 mm × .5 mm × .2 mm, the guard measures .35 mm × .35 mm × .25 mm and is 4.3 mm above the sample, and the fiber is $5 \pm 1\,\mu$m in diameter. With this sample it has been possible to make the motional noise smaller than or at least comparable to the amplifier noise. In the next two sections all of the data taken with sample O will be presented.

9.4 Sample-in Noise

Over a period of two months 30 data records were made with sample **O**. The records are labeled SMIN33, SMIN34,...SMIN43; INSR31, INSR32, ...INSR51. Table 9.1 gives the starting dates of the eight separate data runs and the names of the data records made during each. Between runs the chamber was valved off from the diffusion pump and roughing pump, and the pressure was allowed to rise at a

rate of 100 μmHg/day. To begin a run the nitrogen trap was filled, the diffusion pump was started, and the chamber was evacuated to below 10^{-6} Torr. The rotor was then levitated and spun up to 900 Hz. After about two hours, the sample was neutralized with the probe and the ultraviolet light and then data taking could begin. The length of each data record was limited to about 7 hours by the nitrogen trap hold time, while the length of the runs varied from 12 to 80 hours. Since the rotor loses about .3 Hz per hour, at the end of the longest runs the rotor speed was down to about 880 Hz. At the end of each run the rotor was spun down and landed, and the chamber was valved off.

For the INSR (integer search) data records a $\sim$ .2 sec burst of ultraviolet light was directed at the sample every 200 seconds to produce charge changes. The INSR data will be presented in the next section to demonstrate that the instrument's calibration is 4.7 nV/q_e. In this section we analyse the SMIN (sample in noise) data, for which the ultraviolet light was not used. All of the data was taken at a 1 Hz rate with the sample 200 μm from the rotor.

One record, SMIN36, had a very large linear drift of .3 nV/sec and so went off scale after only 2 hours. At the beginning of the run the sample and guard had to be probed to null the motion sensitivities. The sample was accidently snagged on the probe and the latex strip was stretched to about twice its usual length. It seems likely that the large drift was caused by the latex slowly relaxing back to its normal length. By the time of the next run three days later the drift had returned to normal. The data from record SMIN36 will be omitted below.

Table 9.1. Starting dates and record titles for the eight runs with sample O.

Start Date	Record
2/30/85	SMIN33
3/4/85	SMIN34
3/5/85	SMIN35
3/7/85	SMIN36
3/8/85	INSR31, INSR32, INSR33, INSR34, INSR35
3/15/85	SMIN37, INSR36, INSR37, INSR38, INSR39, SMIN38
3/22/85	INSR40, INSR41, INSR42, SMIN39, INSR43, INSR44
4/19/85	SMIN40, INSR45, INSR46, INSR47, INSR48, SMIN41, INSR49, INSR50, SMIN42, INSR51, SMIN43

SMIN43 was also special. For this run the sample charge was purposely made very large to increase the motion sensitivities so that the motions could be measured. Spectra of this record have already been presented in Fig. 9.4 and Fig. 9.3.

Figures 9.5–9.7 present spectra for all the remaining SMIN records with sample O. Above about 5 mHz only amplifier noise is visible, but at lower frequencies additional noise is present, rising roughly as $1/f$.

Rather than study the spectra directly it will be more useful to study the noise

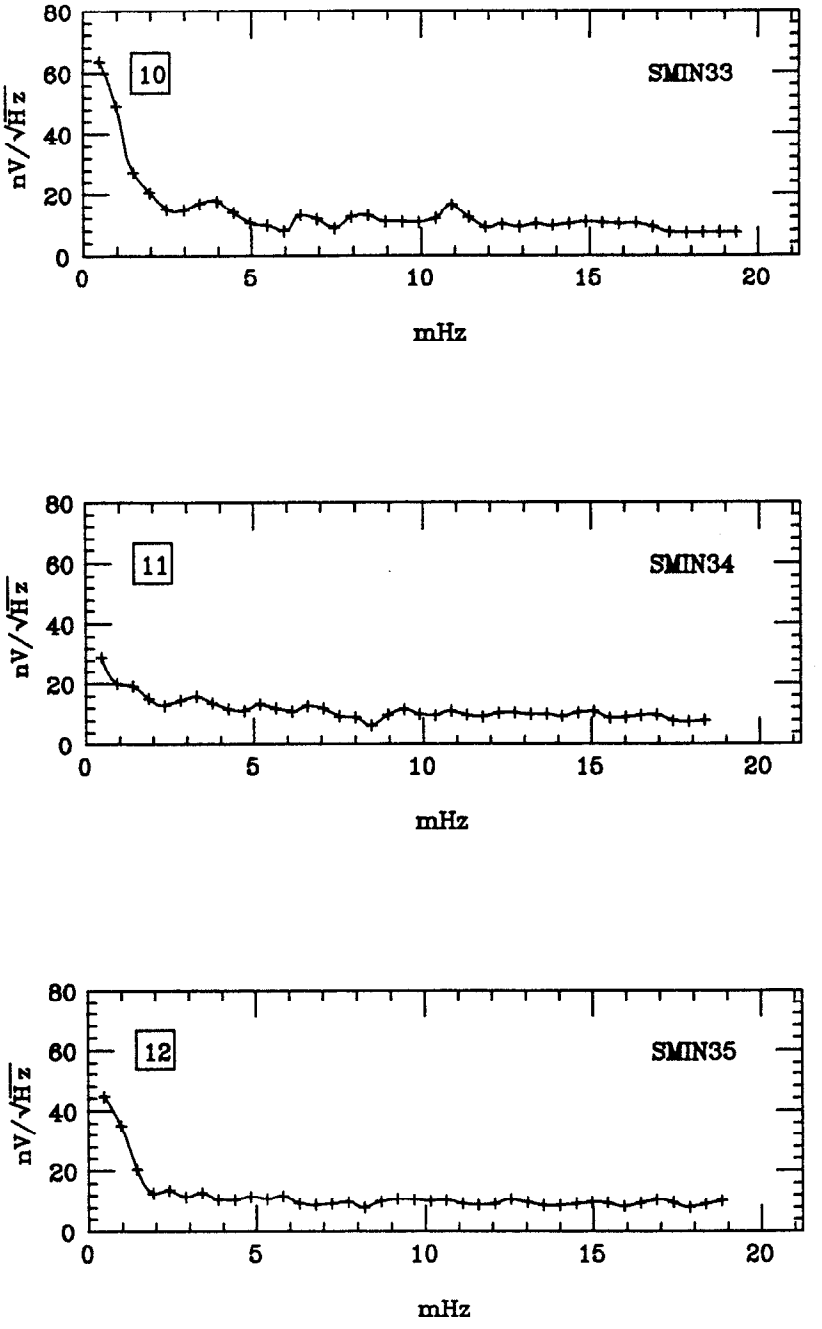

Figure 9.5. Sample-in Spectra; SMIN33, SMIN34, SMIN35

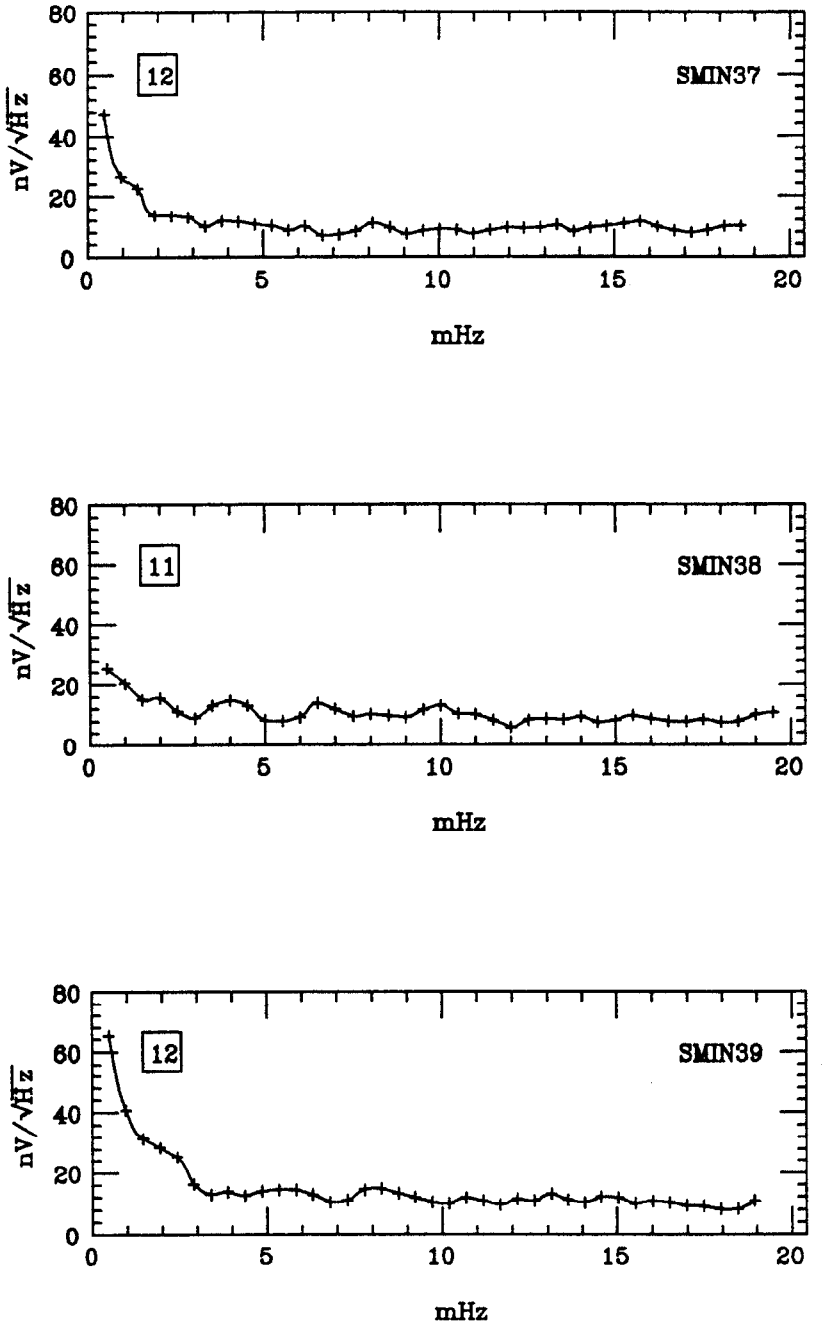

Figure 9.6. Sample-in Spectra; SMIN37, SMIN38, SMIN39

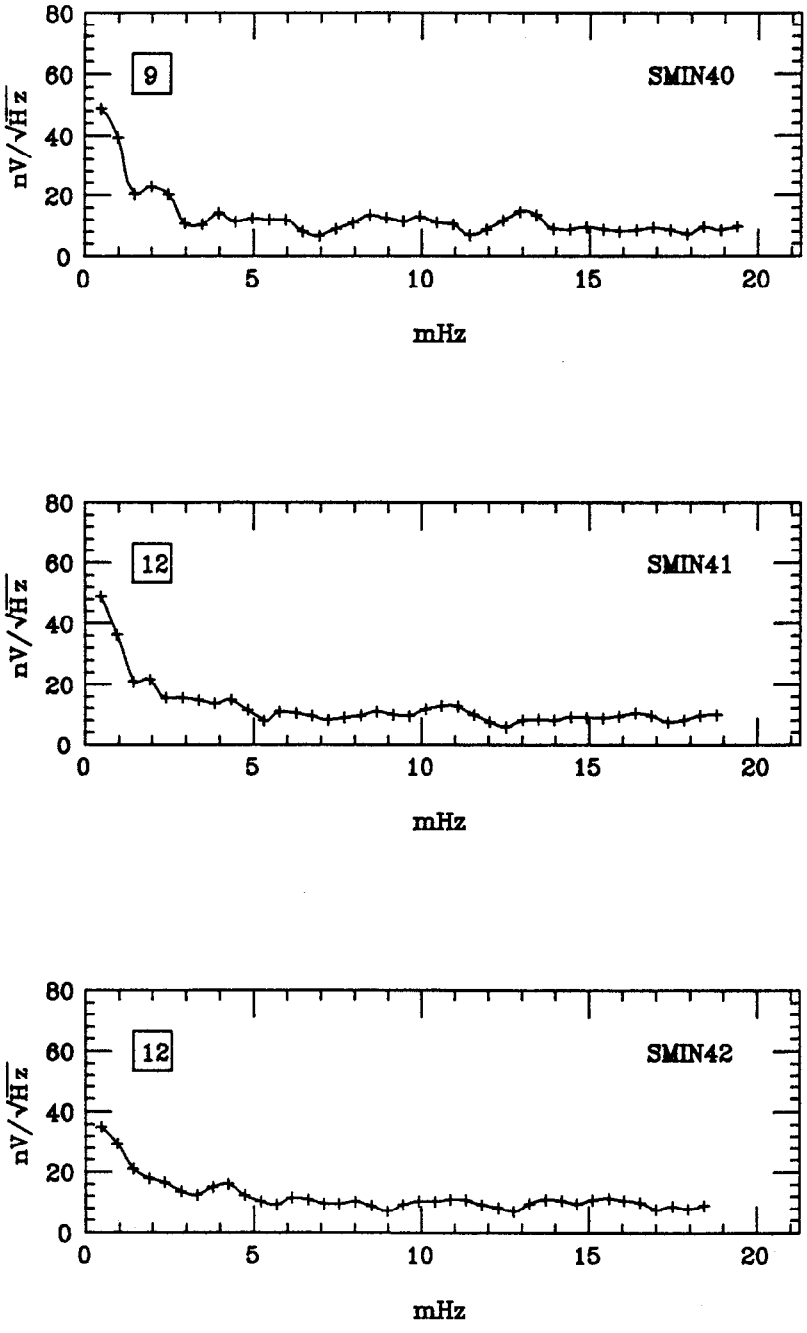

Figure 9.7. Sample-in Spectra; SMIN40, SMIN41, SMIN42

as it would appear in an actual charge measuring experiment. As described earlier, one would first average the output for a time T, then change the contents of the sample container, then average again for a time T, and then take the difference of the two averages. For the INSR data such a charge measuring experiment was simulated by ejecting a few photoelectrons from the sample after each averaging period. For the SMIN data if we apply the same analysis of taking the differences of adjacent averages, the results should have a mean of zero and the standard deviation will be a measure of the resolution.

The average and difference operation is equivalent to integrating the time domain data times a window $W_T(t)$, shown in Fig. 9.8. In frequency domain this is equivalent to filtering with a transfer function

$$|W_T(f)| = 2 \cdot \frac{1 - \cos(2\pi f T)}{2\pi f T}. \tag{9.1}$$

If we model the total noise $\bar{v}_{tot}^2$ as

$$\bar{v}_{tot}^2 = A^2 + \frac{B^2}{f^2}, \tag{9.2}$$

then the variance at the output of the average and difference filter will be

$$\sigma_{tot}^2 = \frac{A^2}{T} + \frac{4}{3}\pi^2 B^2 T, \tag{9.3}$$

as may be shown by integrating $|W_T(f)|^2$ times $\bar{v}_{tot}^2$ from $f = 0$ to ∞. This result implies that there will be an optimal averaging time

$$T_{opt} = \frac{\sqrt{3}}{2} \cdot \frac{A}{\pi B}. \tag{9.4}$$

$W_{T_{opt}}(t)$ is the best square window averaging filter for detection of step changes in the sample charge when the noise is as given in Eqn. 9.2. For our data T_{opt} is near 200 sec, which explains why for the INSR data the ultraviolet light was flashed at this rate.

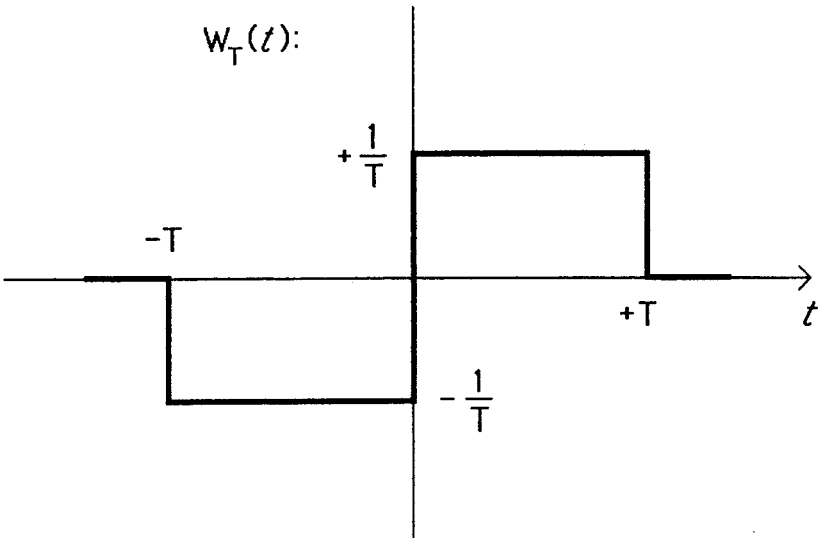

Figure 9.8. Average and Difference Window

Figures 9.9–9.11 show the results of breaking the SMIN data into 200 second long segments, averaging each segment, and then histogramming the difference between adjacent averages. For some of the data records there was a significant nearly linear drift. Since a drift will offset the mean of the distribution, a quadratic

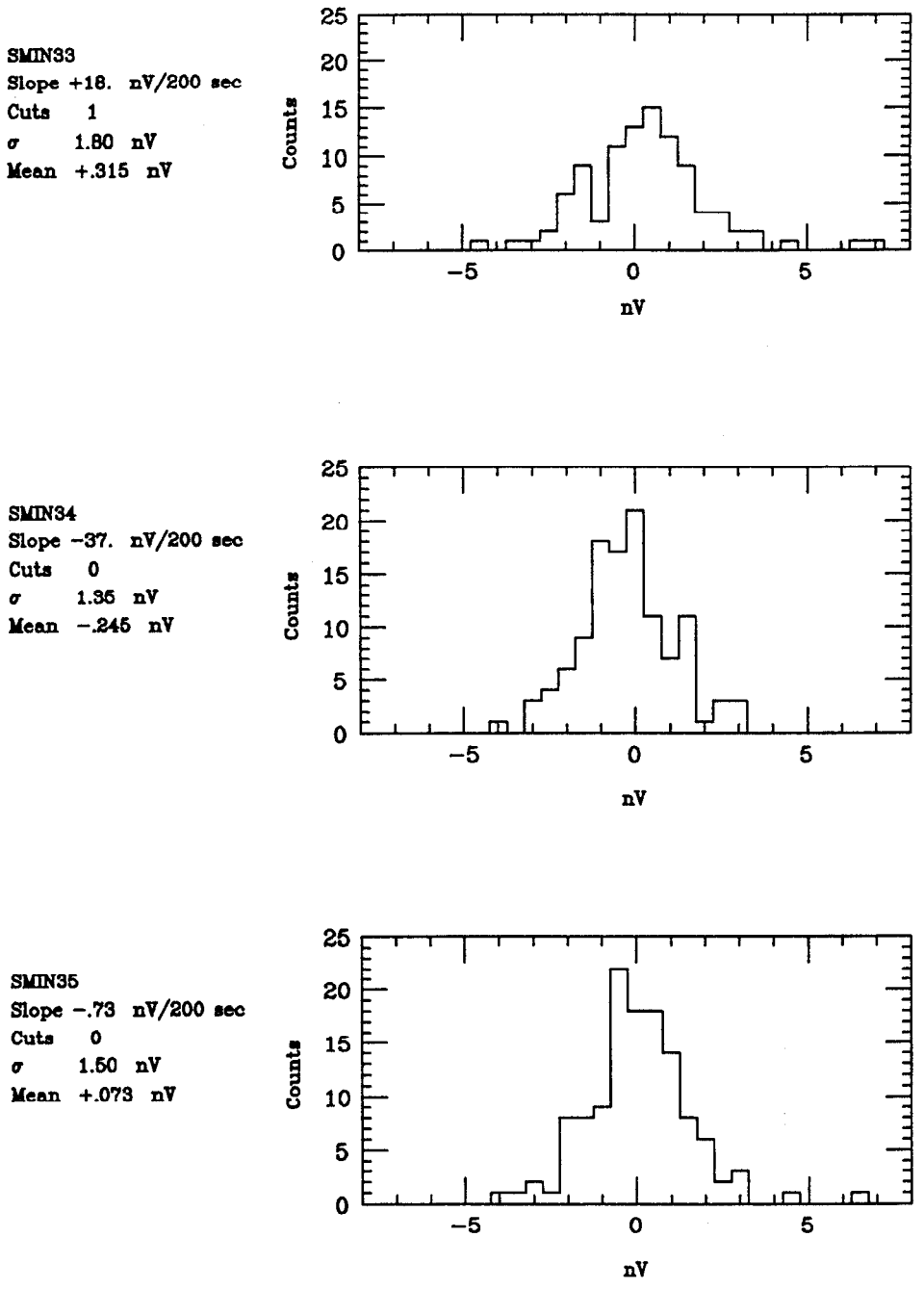

Figure 9.9. Sample-in Histograms; SMIN33, SMIN34, SMIN35. The standard deviation, mean, slope, and number of cuts is shown. Slope is the average slope of the quadratic fit that has been subtracted off.

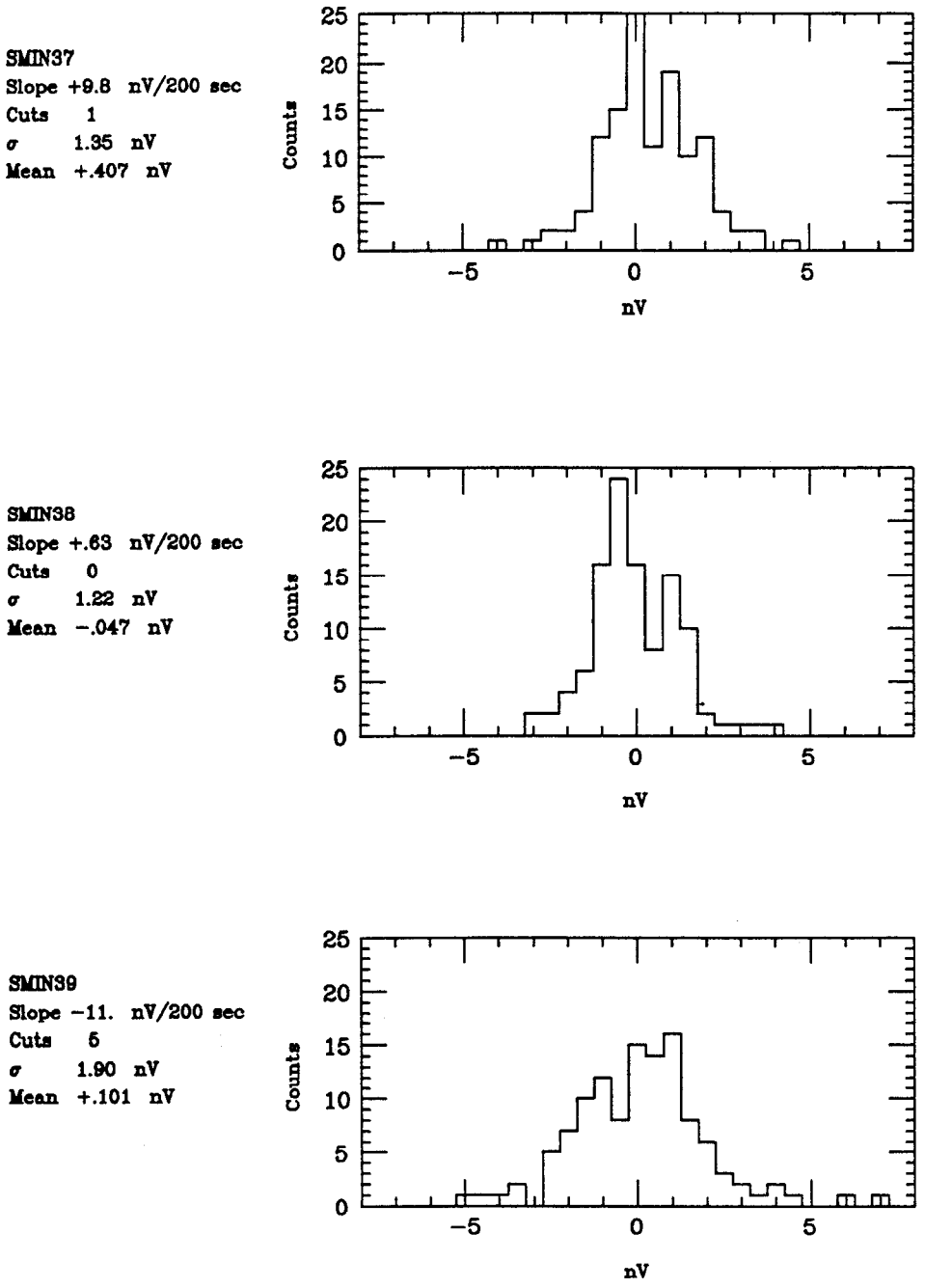

Figure 9.10. Sample-in Histograms; SMIN37, SMIN38, SMIN39

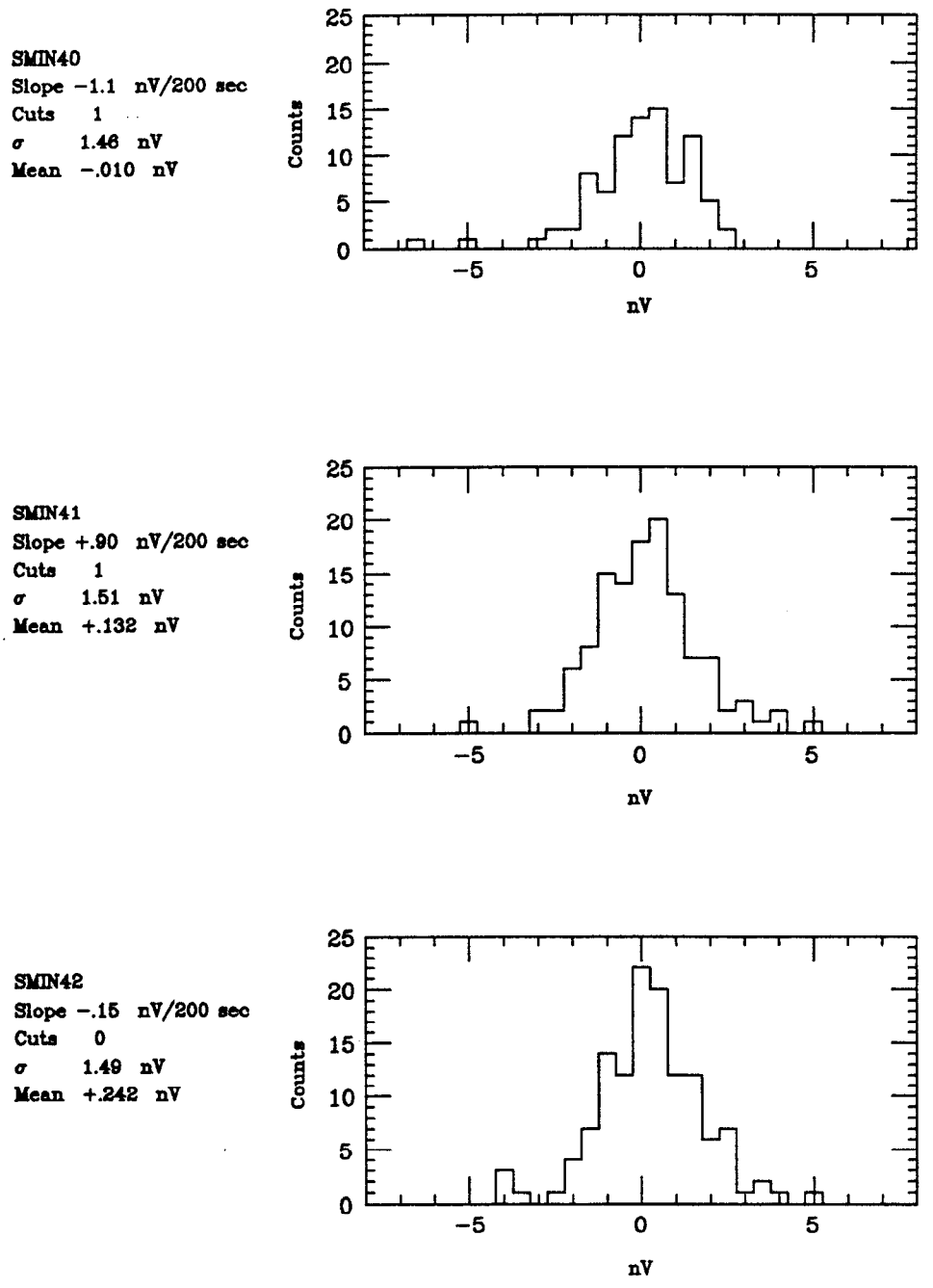

Figure 9.11. Sample-in Histograms; SMIN40, SMIN41, SMIN42

fit has been subtracted off of each data run. The fit was made by first measuring the slope of each 200 second segment, then making a linear fit to the slopes, and then finally integrating the linear fit to the slopes to obtain a quadratic. This procedure was followed because in an actual experiment (and for the INSR data), there will be an unknown step between each 200 second segment so it will be impossible to make a fit to the data directly. Since the means of the distributions are smaller than their standard deviations, it is clear that once the fitting procedure is applied the drifts do not limit the charge resolution.

Points more than 7 nV from the mean have been cut from the histograms; the number cut from each is indicated. A total of nine of the 913 points have been cut; 5 from SMIN39. These points have been cut so they will not dominate our conclusions regarding the noise, but of course in a real experiment they might have to be included. SMIN39 is especially noisy and the instrument showed some peculiar behavior before it was recorded. When the sample was probed (immediately before INSR42, see Table 9.1) there was an abrupt $2\,\mu$V change in the quadrature, and the signal jumped around erratically for a few minutes. One possibility is that a piece of dust was transferred to the sample. The five points cut from SMIN39 were at $-14.5, -14.0, -10.5, +8.5$, and $+9.0$ nV, while the four points cut from the other records were at $+26.0, +11.5, +8.0$, and $+10.5$ nV. Figure 9.12 is the sum of the SMIN histograms, excluding SMIN39. The distribution is too broad at the bottom to be Gaussian. The σ judged from the width at half maximum is 1.1 nV, while the rms of the points is 1.46 nV.

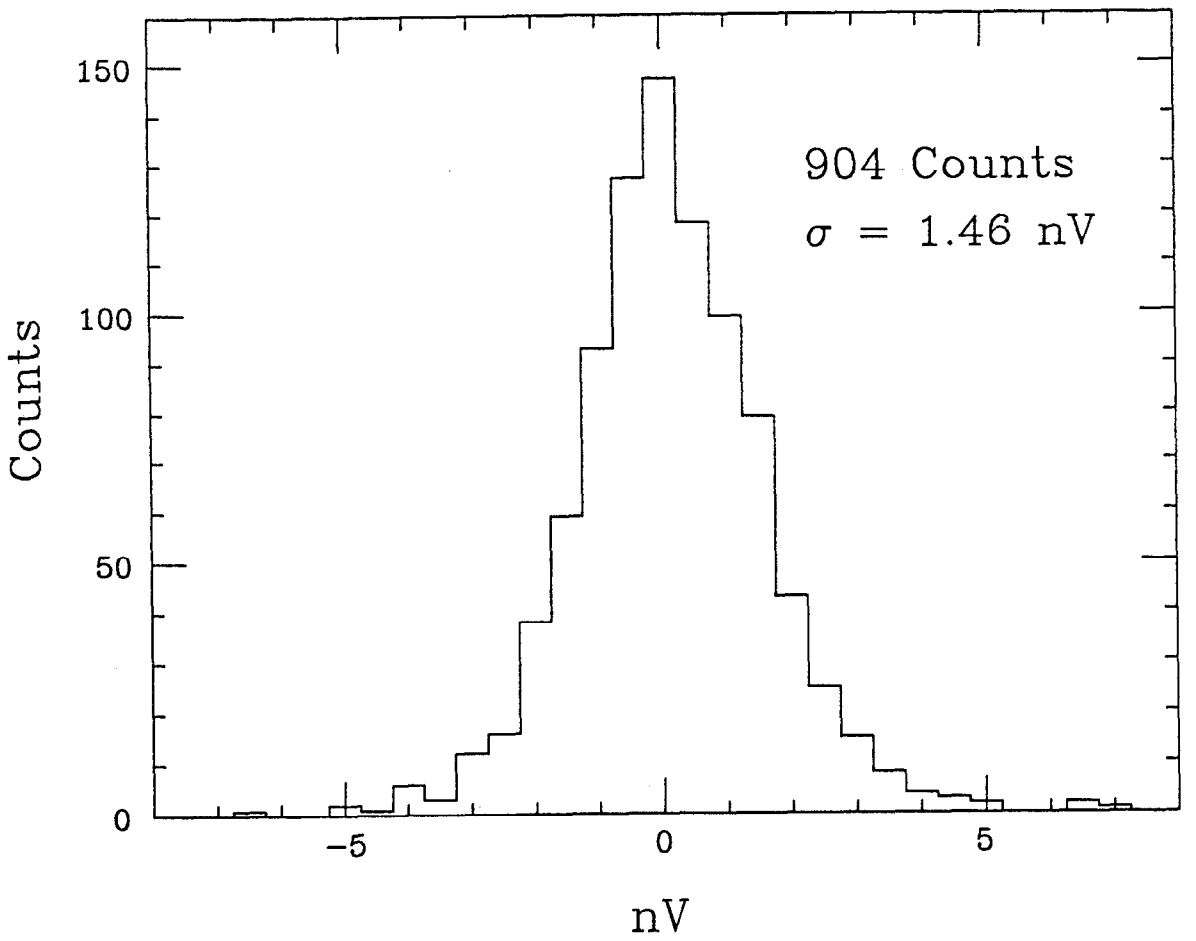

Figure 9.12. Sum of the SMIN histograms, excluding SMIN39

Table 9.2. Motion sensitivities for the SMIN data.

Record	V	R	Q
SMIN33	$2.4\,\mathrm{nV}/\mu\mathrm{m}$	$1.1\,\mathrm{nV}/\mu\mathrm{m}$	$-24\,\mu\mathrm{V}$
34	1.0	$<.1$	-18
35	1.4	.5	-19
37	$<.9$	$<.1$	$-.6$
38	$<.9$	$<.1$	-1.9
39	1.0	1.3	-5.4
40	$<.9$	1.7	$-.8$
41	$<.9$	.8	.9
42	$<.9$	2.4	.9

We now want to see to what extent we can account for the standard deviations of the histograms. The amount of rotor motion inside the passband of the 200 second average and difference filter can be calculated by integrating $|W(f)_T|^2$ times the square of the motion spectra given in the previous section. We find for the rms motions

$$\begin{aligned} \sigma_V &= .14 \pm .02\,\mu\mathrm{m}, \\ \sigma_R &= .30 \pm .05\,\mu\mathrm{m}, \\ \sigma_P &= .03 \pm .01\,\mathrm{mR}, \end{aligned} \tag{9.5}$$

where V, R, and P mean vertical, radial, and phase. To find the contribution to the total noise these must be multiplied by the measured motion sensitivities and quadrature signal, which are given for each run in Table 9.2. The amplifier noise contribution to the total noise is $(8.8\,\mathrm{nV}/\sqrt{\mathrm{Hz}})/(200\,\mathrm{sec})^{1/2} = .62\,\mathrm{nV}$.

Figure 9.13 displays the conclusions. The squares are the measured standard deviations of each histogram, with statistical errors shown. The dotted line shows the amplifier noise level and the diamonds are the total accounted for noise, meaning

the amplifier noise plus the motional noise. The motion sensitivities are small enough so that the motional noise is always less than twice the amplifier noise and is sometimes negligible.

Figure 9.14 shows the difference between the observed noise and the accounted for noise. Excluding SMIN39, the unexplained noise has an average value of $1.21 \pm .06\,\mathrm{nV}$ and is constant from record to record within the uncertainties. This noise cannot be accounted for by any of the mechanisms considered so far. We have not so far been able to identify the source of the unexplained noise, but will consider some possibilities below.

At some rate there must be spontaneous changes of the sample charge due to cosmic rays and natural radioactivity. If the sample charge were changing by $1q_e$ at random times it would generate a charge noise spectrum

$$\bar{q}_n = q_e \cdot \frac{(2R)^{1/2}}{2\pi f}, \tag{9.6}$$

where R is the mean charge change rate. This formula is simply the time integral of the formula for shot noise: $\bar{\imath}_n = (2q_e I)^{1/2}$. The result also holds if the changes are $-1q_e$, or if the changes are of both signs. Using Eqn. 9.3 above and the instrument's calibration of $4.7\,\mathrm{nV}/q_e$, the 1.2 nV of unexplained noise can be accounted for if $R = 1.8\,\mathrm{nV/hour}$. The frequency where the noise from charge changes and the amplifier noise make equal contributions would be 2.7 mHz, and the spectrum would rise as $1/f$ below this point. This seems to be roughly the behavior in the spectra for SMIN37, SMIN38, and SMIN41, for which the motional noise contribution is

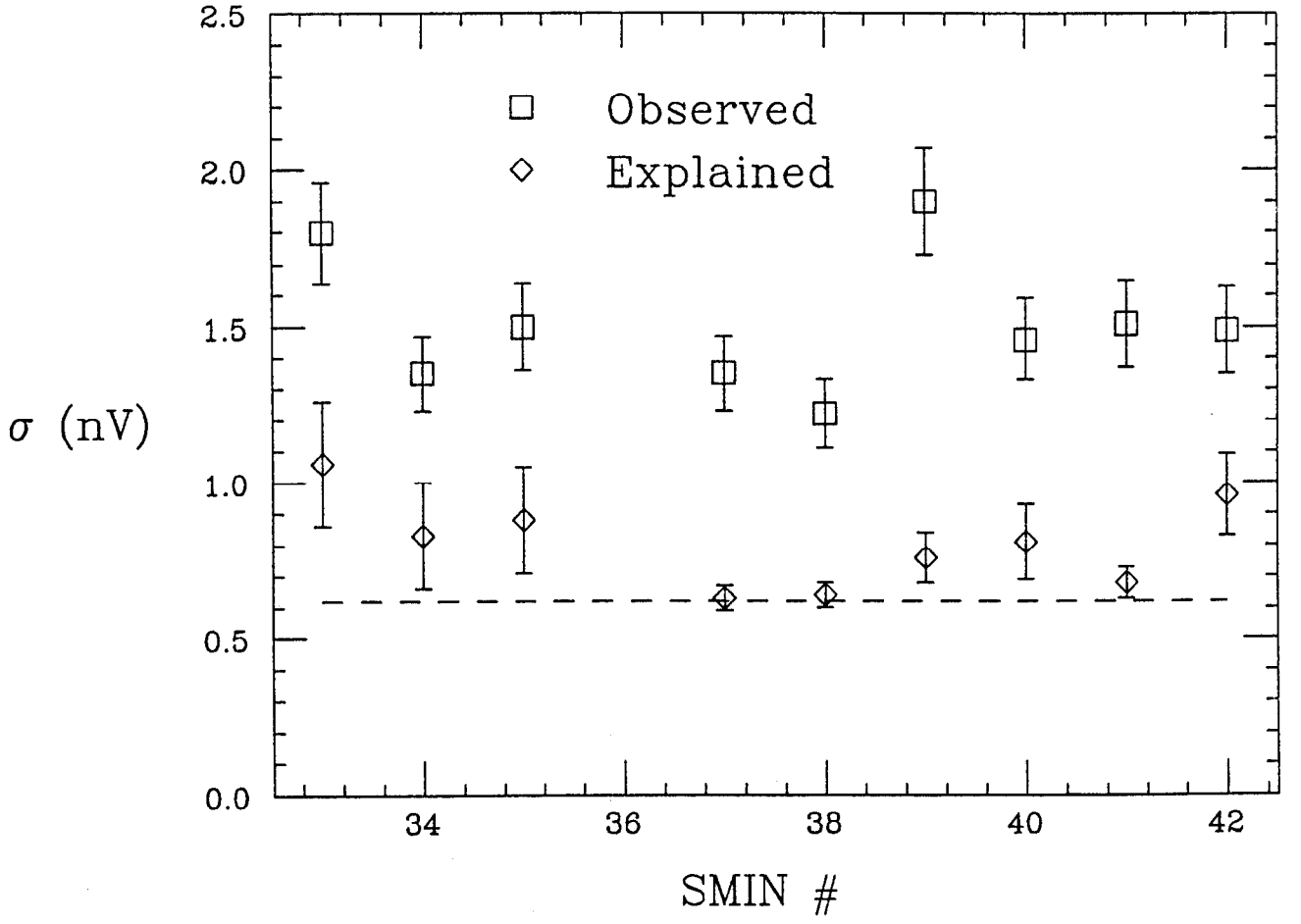

Figure 9.13. Noise through the 200 second square average filter.

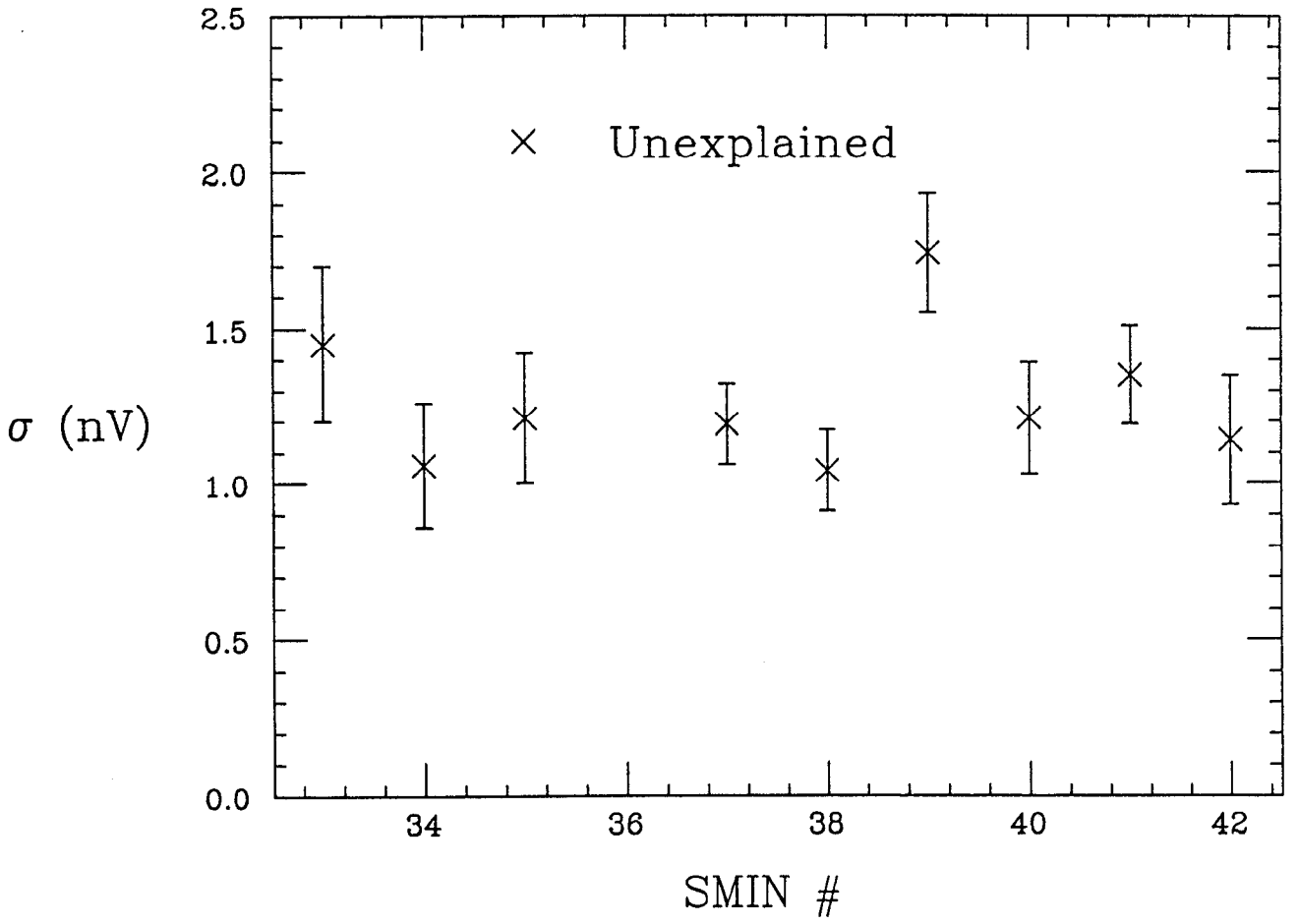

Figure 9.14. Unexplained Noise

negligible.

To test the hypothesis that the unexplained noise is due to charge changes, we can convolve the time domain data with the window of Fig. 9.8. If we set a threshold and count the number of times the convolved data crosses the threshold, we can hope to count the number of spontaneous charge changes. A problem arises however, because the raw data has an unknown drift, which may be due in part to spontaneous charge changes but is certainly not due entirely to them. If we make a linear fit to the data and subtract it off, we would cause an unknown offset in the convolution output if some of the drift is due to charge changes. We will instead convolve with the window in Fig. 9.15 which is immune to a linear drift. Convolution with this window is equivalent to making a least squares fit to the intervals on either side of $t = 0$, and then measuring the differences of the y-intercepts of the fit lines at $t = 0$. The bandwidth of the least squares window is $4/T$ instead of $1/T$ as for the square window. To regain some of the lost resolution we can increase T to 400 seconds, which should not result in intolerable pileup since we are looking for charge changes that occur at an average rate of 1/2000 seconds. The amplifier noise will now make a contribution of .88 nV.

We will restrict this analysis to SMIN37, SMIN38, and SMIN41, for which the motional noise contributions are at least three times less than the amplifier noise, and test the hypothesis that the total noise is due to amplifier noise plus spontaneous charge changes. If we set the threshold at 3σ for the amplifier noise, or ± 2.64 nV, then we can expect a false rate of one per 370 opportunities. An opportunity occurs

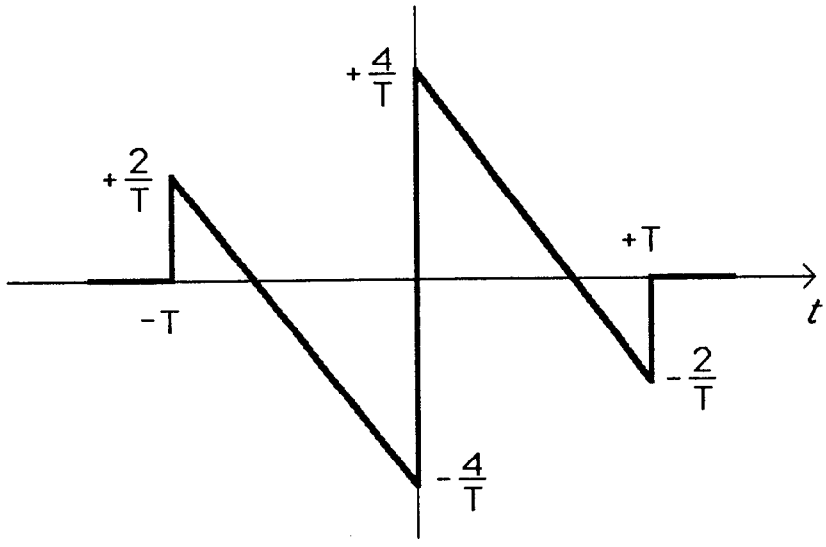

Figure 9.15. Least Squares Average and Difference Window

about once per 400 seconds (since the output will be highly correlated over about 400 seconds) so we estimate a false rate of $\sim 7 \cdot 10^{-6}$/sec. To test the estimate a data record of amplifier noise was convolved with the least squares window. One count was recorded in 21000 seconds, where .15 counts were expected according to the estimate.

Convolution with the 72100 seconds of data in SMIN37, SMIN38, and SMIN41 yielded 85 excursions above threshold, or a rate of 4.3/hour, with .50 false counts expected. Figure 9.16 is a histogram of the peak value of each excursion above threshold. The rate is 2.5 times too high to be due to spontaneous charge changes,

and the peak values do not cluster around $\pm q_e = \pm 4.7\,\mathrm{nV}$. Since the rate is high there is now considerable pileup (peaks above threshold occurring within 400 seconds of each other), so one objection that might be raised is that the background estimate could be wrong in the region ± 400 seconds around a true $\pm q_e$ charge change. This worry can be disposed of as follows. We can place an upper bound on the true charge change rate by setting the threshold at $\pm q_e = \pm 4.7\,\mathrm{nV}$, and then doubling the number of counts obtained to account for the fact that the amplifier noise will cause half of the charge changes to fluctuate above 4.7 nV, and half below. We find 10 counts, or a rate of $2 \cdot 10/20$ hours $= 1/\mathrm{hour}$. If we now look in the region 400 seconds before and after the 10 counts above $\pm 4.7\,\mathrm{nV}$, we find 11 more counts which might be considered false. We could perhaps thus account for as many as $2 \cdot (10 + 11) = 42$ of the counts, but this still leaves 43 unexplained. The conclusion finally is that there *could* be a spontaneous charge change rate of $2 \cdot (10 \pm \sqrt{10})/20\,\mathrm{hours} = 1 \pm .3/\,\mathrm{hour}$, accounting for about half of the unexplained noise, but that there is certainly also some other noise source.

Of course some spontaneous charge changes must occur. If the cosmic ray intensity is described by (79)

$$I = 1.10 \cdot 10^{-2} \cos^2\theta \cdot \mathrm{cm}^{-2} \cdot \mathrm{sec}^{-1} \cdot \mathrm{sterad}^{-1}, \tag{9.7}$$

where θ is the zenith angle, then the collision rate with the sample will be .25/hour. This may cause as many as .25 charge changes per hour. Also, the sample is made of a radioactive material. Natural indium is 95.7% In^{115}, which $\beta-$decays with a

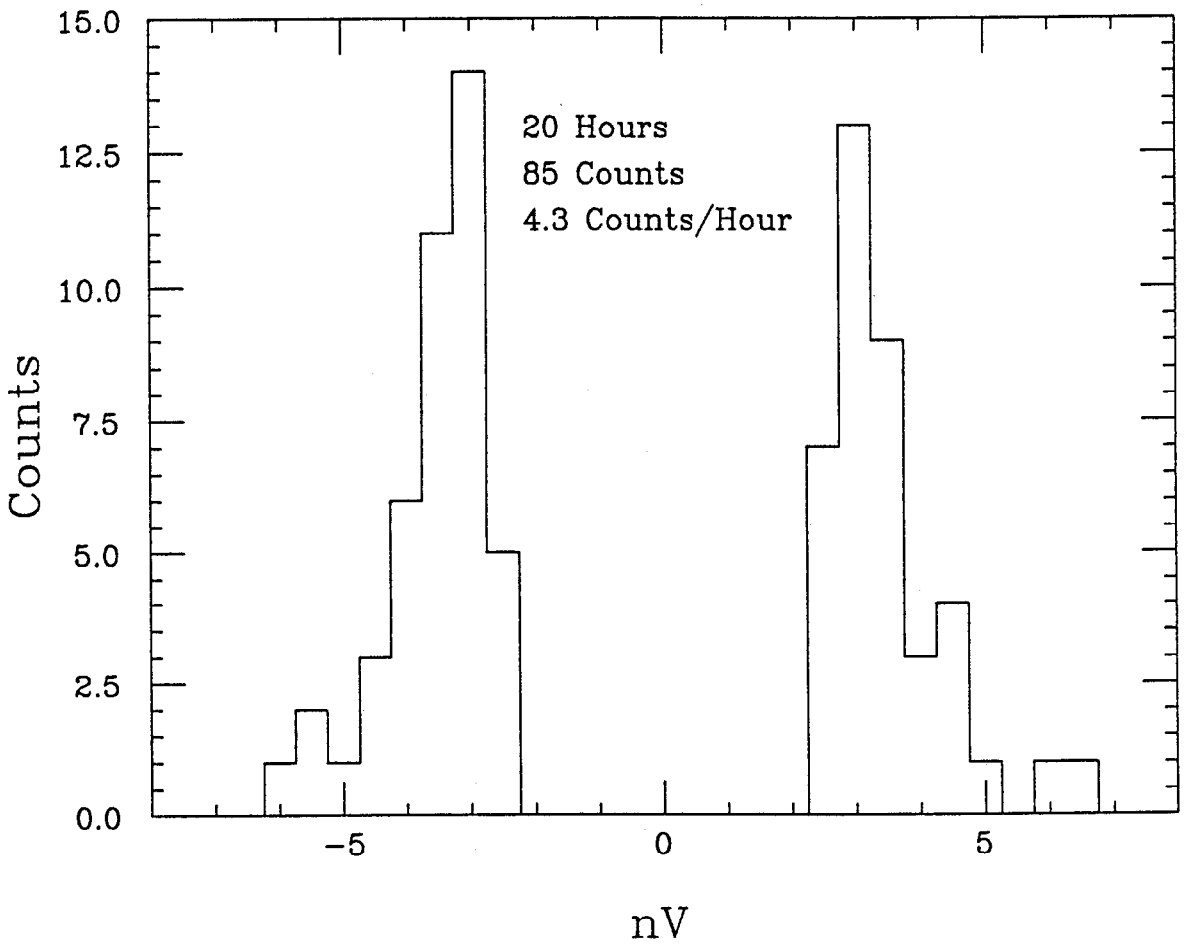

Figure 9.16. Peak value of each excursion above threshold. Three points are off scale at +14.14, +8.82, and +7.41 nV.

half life of $5 \cdot 10^{14}$ years and an end point energy of .5 MeV*. In our .73 mg sample there will be .6 decays per hour. The mean range for the electrons is about equal to the .2 mm sample thickness, so a large fraction of the emitted electrons will leave the sample. A charge change rate as large as .5/hour can be accounted for by this mechanism. The sum of these two rates is still within the 1/hour rate allowed by the analysis given above.

There are several other possible sources for the unexplained noise. A major worry is that somehow some motion has gone undetected. Although we have some information on each axis, it would be far preferable to continuously monitor the sample position relative to the rotor in all three axes while data is being recorded. This would certainly be recommended in a future instrument.

Another source of noise might be charge motion on the quartz fiber. Several studies have been made with conventional electrometers of the surface resistance of quartz glass (80). Unfortunately they do not provide enough information for our purposes, since the instrument could be disturbed by rare but highly mobile carriers. Even a single mobile ion on the quartz surface might be able to generate the noise we see, but would be undetected in a conventional measurement of surface resistivity. Perhaps this issue could be studied by trying samples with different fiber diameters.

---

* I thank Professor Cabrera for pointing out that indium is radioactive. This was overlooked when indium was chosen as the sample material.

9.5 Detection of Electrons

The INSR data records were made during four different runs, as shown in Table 9.1. The intensity and duration ($\sim$ .2 second) of the of the ultraviolet light pulses was not varied during a run, but was different from run to run. Figures 9.17 and 9.18 show histograms including all of the INSR records in each of the four runs, generated in exactly the same way as the SMIN histograms in Figs. 9.9–9.11. A quadratic fit was subtracted off each record as before by first making a linear fit to the slopes of each 200 second segment, and then integrating to get a quadratic fit to the data record. The average value of each 200 second segment was computed, and the differences of adjacent averages were histogrammed. No cuts have been made, but three points are off scale on the 3/22/85 histogram.

The explained noise, meaning the motional noise plus the amplifier noise, is given for each run on the histograms. The values are similar to those in Fig. 9.13 for the SMIN records. The run of 3/22/85 seems to be more noisy than the others. This is the same run during which SMIN39 was recorded. As was mentioned in the previous section, the instrument showed some peculiar behavior during this run, perhaps due to dust.

All of the runs show evidence for discrete changes in the sample charge. The charge changes are positive, showing that the photoelectrons are negatively charged. Judged from the run of 4/19/85, the instrument's calibration is $4.7\,\mathrm{nV}/q_e$. Figure 9.19 shows the number of counts in each peak in the run of 4/19/85. The

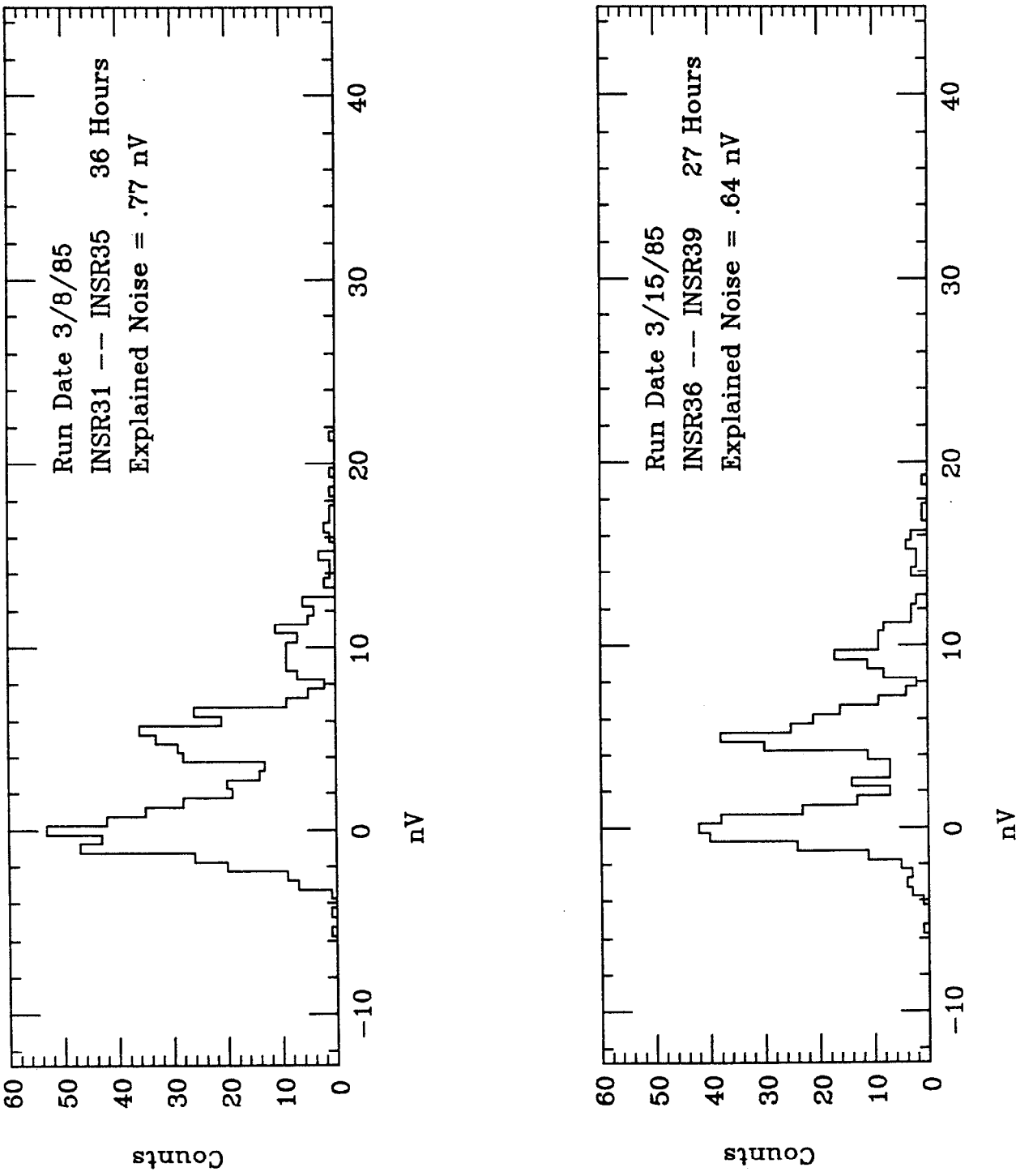

Figure 9.17. INSR31 – INSR35 and INSR36 – INSR39

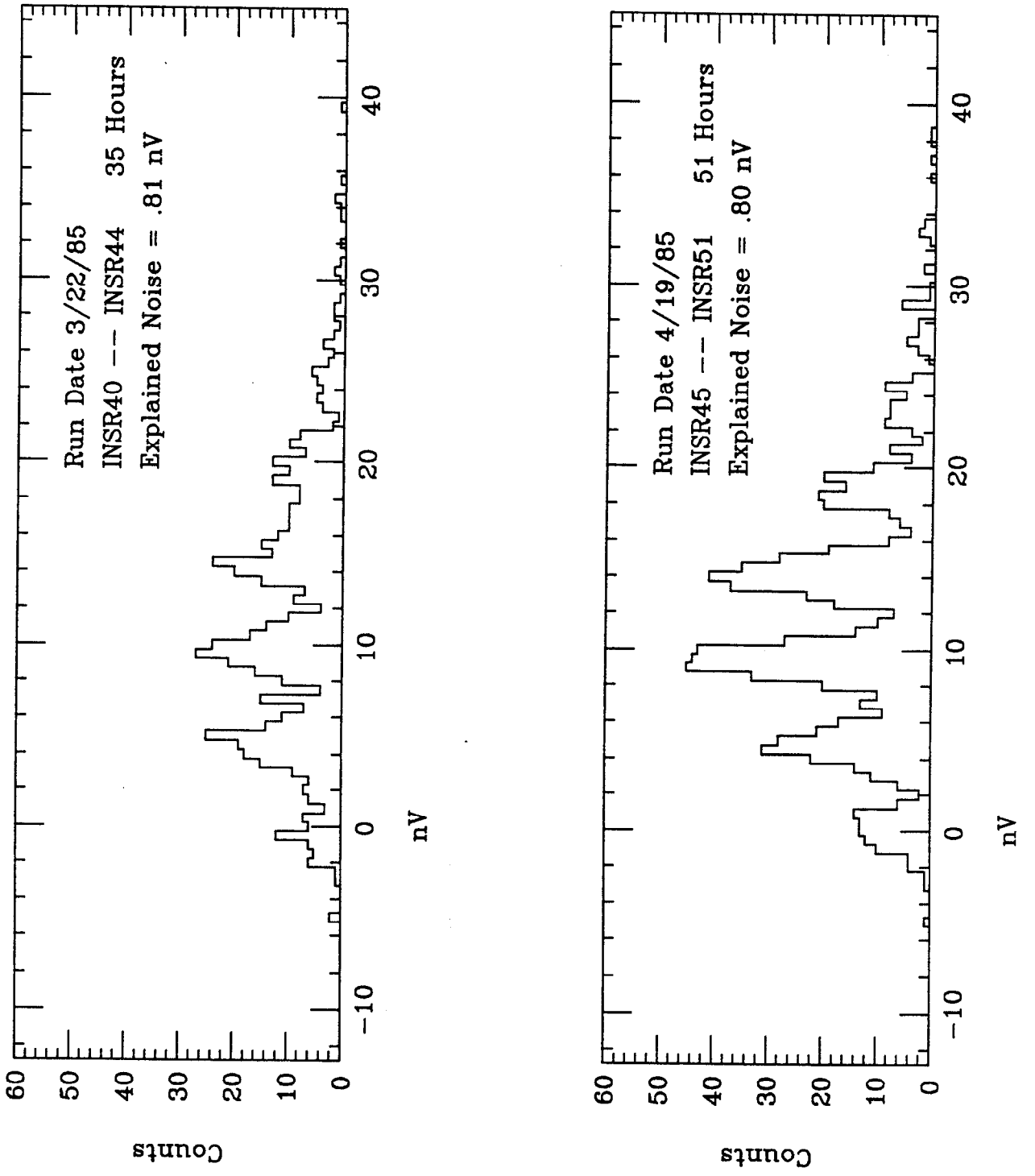

Figure 9.18. INSR40 – INSR44 and INSR45 – INSR51

crosses are the data while the squares are a Poisson distribution with the same mean as the data. This shows the Poisson statistics of the photoemission process.

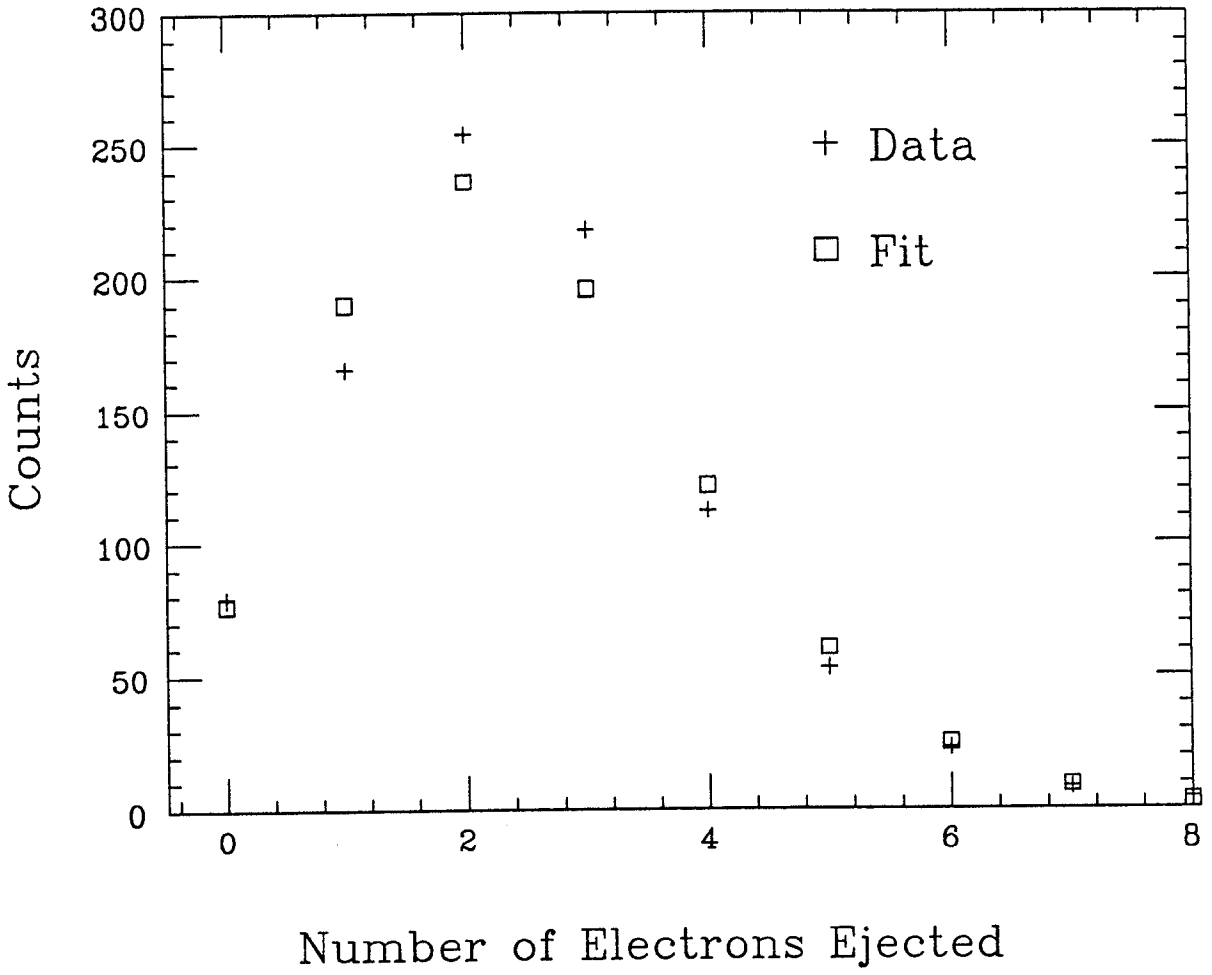

Figure 9.19. Photoemission Statistics. Number of counts in each peak in the run of 4/19/85. The fit points are from a Poisson distribution.

10. Prospects for a Fractional Charge Search

Let us first ignore the motional noise and the unexplained noise and consider whether the amplifier noise limited resolution can be made sufficient for a fractional charge search. As the instrument stands, the amplifier noise is $8.8\,\mathrm{nV}/\sqrt{\mathrm{Hz}}$ and the calibration is $4.7\,\mathrm{nV}/q_e$. For the 200 second square average and difference procedure the amplifier noise limited resolution is therefore

$$8.8\,\mathrm{nV}/\sqrt{\mathrm{Hz}} \cdot \frac{1}{(200\,\mathrm{sec})^{1/2}} \cdot \frac{1}{4.7\,\mathrm{nV}/q_e} = .13\,q_e.$$

A resolution of $.05\,q_e$ seems like a good goal, since then a peak at $1/3\,q_e$ would be separated from zero by 6.7 standard deviations, so a data point would have to fluctuate by more than 3 standard deviations to mimic a fractional charge. Thus a factor of 2.6 is needed. There are several places where it might be found:

- The total electrostatic inefficiency (which is not all understood) is 2.7. Perhaps it can be improved.
- A factor of about 1.4 can probably be gained by cooling the JFET.
- A thorough search might turn up a quieter JFET.
- A factor of two increase in the signal frequency together with a factor of two decrease in C_S would give a factor of 1.4 in resolution (see section 7.4).
- The averaging time can be increased.

Increasing the averaging time is a last resort, since this will slow down the measurement and may make the motional noise harder to control. It seems very

likely that by some means the amplifier noise limited resolution can be reduced to $.05\,q_e$.

The unexplained noise presently contributes $.25q_e$ to the resolution, so it must be reduced by a factor of 5. Hopefully the reader will not be too discouraged by this. As is evident from section 9.3, nearly all of the work so far with samples in the instrument has been aimed at reducing the motion sensitivity. Only with the last sample was the unexplained noise clearly identified, so there has been little opportunity to study it. A first step would be to see what effect changes in the sample size and fiber diameter have on the unexplained noise. With the new guarding technique it will very likely be possible to study somewhat larger samples, and it is certainly possible to study smaller ones.

With sample motion sensitivities of $1\,\mathrm{nV}/\mu\mathrm{m}$, as have been achieved with sample O, the motional contribution at present is about equal to the amplifier noise, and so it must be reduced by a factor of 3. If the motions are due to thermal effects they can certainly be reduced, since the instrument could be made more compact and from lower expansion materials. If the vertical motion is due to electronic noise in the suspension then this can certainly also be improved. It is encouraging to note that in the phase direction the motions are already small enough, since the .03 mR rms phase motion corresponds to $.06\,\mu\mathrm{m}$ rms.

Perhaps the most serious problem that remains is maintaining the sample container position when the sample is changed. With $1\,\mathrm{nV}/\mu\mathrm{m} = .2\,q_e/\mu\mathrm{m}$ motion sensitivity, to keep the systematic error below $.05\,q_e$ it would be necessary to

reproduce the sample container position to .25 μm after a sample change. This seems difficult but possible. Actually there is no reason why the motion sensitivity cannot be nulled more accurately than this. We have been limited to 1 nV/μm only because during an INSR data record the sample charge is changed by several hundred q_e, which changes the motion sensitivity by $\sim$ 1 nV/μm. This would not be a problem in a real experiment since the sample container charge may always be readjusted by photoemission after the sample is changed.

One might worry that a small change in the sample container weight would stretch the fiber by more than .25 μm. In fact for a 1 cm long 5 μm diameter fiber a mass change of 1 mg causes an extension of only .05 μm, so this does not by itself seem very serious. Much more worrisome is the fact that our description of the motions in terms of three translations will at some point be inadequate. When the sample is changed, the sample container and guard might move relative to one another, and then the relevant motion sensitivity might well be what was observed with unguarded samples; say 4 q_e/μm for small samples or 40 q_e/μm for large ones. This seems very discouraging. If stretching of the fiber is the only factor causing relative motion of the sample and guard, then by holding the sample weights equal to 50 μg even the 40 q_e/μm value could be tolerated. Unfortunately the structure may twist or, if the fiber is not quite straight, it may flex. These problems require careful study before the experiment can be attempted.

Perhaps the motion sensitivity difficulties could be greatly reduced if the sample container were magnetically levitated. Since we don't know how much of the motion

sensitivity is due to the fiber charge and how much is due to surface potentials, we can't say for certain how much good this would do. The rotor geometry would have to be changed to make room for the suspension magnet, and the pads would have to be very thin to eliminate heating from eddy currents. The motion of the pads through the suspension magnetic field would cause a $\sim 30\,\mathrm{mV}$ potential drop across each pad, but since this is of the same order as the surface potentials already present, it may not be a problem.

Whatever path is taken in the future, it seems likely that several more years of work remain before the rotor electrometer will first provide data on the existence of fractional charge. Because the ultimate goal of the project is still distant, and because the important intermediate goal of detecting single electrons has just been met, this seemed like a good point to stop and give a full report of the progress so far. It is hoped that the work presented here will be of interest to workers involved in the search for fractional charge. Also, if it should turn out that the rotor electrometer has other applications, it is hoped that some readers will be able to apply what is reported in this thesis to their own goals.

REFERENCES

1. G. S. LaRue, J. D. Phillips, and W. M. Fairbank, Phys. Rev. Lett. **46**, 967 (1981), and references therein.
2. M. Gell-Mann, Phys. Lett. **8**, 214 (1964).
3. G. Zweig, CERN Report No. 8182/TH 401 (1964) (unpublished), CERN Report No. 8419/TH 412 (1964) (unpublished).
4. A. J. G. Hey and R. L. Kelly, Phys. Rep. **96**, 71 (1983).
5. C. Quigg, *Guage Theories of the Strong, Weak, and Electromagnetic Interactions*, (Benjamin, Menlo Park, 1983), p.21.
6. Particle Data Group, Rev. Mod. Phys. **56**, (1984).
7. F. Close, *An Introduction to Quarks and Partons*, (Academic Press, London, 1979).
8. S. Gasiorowicz and J. L. Rosner, Am. J. Phys. **49**, 954 (1981).
9. M. Creutz, in *Proceedings of the* 20^{th} *International Conference on High Energy Physics*, (Madison, Wisc., July 1980).
10. A. De Rújula, R. C. Giles, and R. L. Jaffe, Phys. Rev. **D17**, 285 (1978).
11. R. V. Wagoner, preprint ITP-673-STANFORD (1980).
12. J. D. Bjorken, preprint SLAC-PUB-2366 (1979).
13. R. Slansky, T. Goldman, and G. Shaw, Phys. Rev. Lett. **47**, 887 (1981).
14. M. Han and Y. Nambu, Phys. Rev. **139B**, 1006 (1965).
15. P. M. Zerwas, preprint PITHA 84/30 (1984).
16. PLUTO collaboration, preprint DESY-84-070 (1984).

17. E. Fernandez *et. al.*, Phys. Rev. Lett. **54**, 95 (1985).

18. H. J. Lipkin, Nucl. Phys. **B155**, 104 (1979).

19. J. Pati and A. Salam, Phys. Rev. **D8**, 1240 (1973), Phys. Lett. **142B**, 91 (1984) and references cited therein.

20. J. H. Field, preprint LPNHE-84-04 (1984).

21. L. W. Jones, Rev. Mod. Phys. **49**, 717 (1977).

22. L. Lyons, Progress in Particle and Nuclear Physics **7**, 157 (1981).

23. G. Susinno, in *Proc. of the Int. Conf. on Physics in Collision: High Energy ee/ep/pp Interactions, Blacksburg, Virginia, 1981*, Vol. I, edited by W. P. Trower and G. P. Bellini (New York, Plenum Press, 1982) p.33.

24. H. Aihara *et al.*, Phys. Rev. Lett. **52**, 2332 (1982).

25. M. Banner *et al.* (UA2 collaboration), Phys. Lett. **156B**, 129 (1985).

26. S. W. Barwick *et al.*, Phys. Rev. **D30**, 691 (1984).

27. W. A. Chupka *et al.*, Phys. Rev. Lett. **17**, 60 (1966); D. M. Rank, Phys. Rev. **176**, 1636 (1968).

28. G. Morpurgo *et al.*, Nucl. Instrum. Meth. **79**, 95 (1970).

29. D. Joyce *et al.*, Phys. Rev. Lett. **51**, 731 (1983).

30. R. N. Boyd *et al.*, Phys. Rev. Lett. **40**, 216 (1978); R. N. Boyd *et al.*, Phys. Rev. Lett. **43**, 1288 (1979); W. Kutschera *et al.*, Phys. Rev. **D29**, 791 (1984); R. Bland *et al.*, Phys. Rev. Lett. **39**, 369 (1977); G. D. Putt and P. C. M. Yock, Phys. Rev. **D17**, 1466 (1978); J. P. Schiffer *et al.*, Phys. Rev. **D17**, 2241 (1978).

31. R. G. Milner *et al.*, Phys. Rev. Lett. **54**, 1472 (1985).

32. D. Liebowitz, M. Binder, and K. O. H. Ziock, Phys. Rev. Lett. **50**, 1640 (1983).

33. M. A. Lindgren *et al.*, Phys. Rev. Lett. **51**, 1621 (1983) and references therein. The most recent data on 2 mg of Hg has not yet been published.

34. M. Marinelli and G. Morpurgo, Phys. Lett. **137B**, (1984) and references therein.

35. P. F. Smith *et al.*, Phys. Lett. **153B**, 188 (1985).

36. J. P. Schiffer, Phys. Rev. Lett. **48**, 213 (1982).

37. G. Hirsch, R. Hagstrom, and C. Hendriks, Lawrence Berkeley Laboratory preprint LBL-9350 (1979).

38. J. Van Polen, R. Hagstrom, and G. Hirsch, to be published.

39. E. R. Williams and G. T. Gillies, Lett. Nuovo Cimento **37**, 520 (1983).

40. R. W. J. Barker, Proc. IEE, IEE Reviews **11R**, (1983).

41. Keithley Model 642 Digital Electrometer.

42. H. Palevsky, R. K. Swank, R. Grenchik, Rev. Sci. Instrum. **18**, 298 (1947).

43. E. R. Williams, G. T. Gillies, Lett. Nuovo Cimento **37**, 520 (1983).

44. J. R. Biard, Proc. IEEE **51**, 298 (1963); J. C. Decroly et al., *Parametric Amplifiers*, (John Wiley and Sons, New York, 1973); J. A. Davis, Ph.D. thesis, Stanford University Dept. of Electrical Engineering, 1974.

45. Private communications.

46. A. Einstein, Phys. Zeitschr. **9**, 216 (1908).

47. C. Habicht and P. Habicht, Phys. Zeitschr. **11**, 532 (1910). Other references to the instrument are given by A. Pais, *Subtle is the Lord—*, (Oxford University Press, Oxford, 1982), pp.484–485.

48. R. Gunn, Phys. Rev. **40**, 307 (1932).

49. R. H. Dicke, Rev. Sci. Instrum. **17**, 268 (1946).

50. W. Innes, S. Klein, M. Perl, J. C. Price, preprint SLAC-PUB-2938 (1982).

51. This technique for grounding shafts has also been used by J. W. Beams, Rev. Sci. Instrum. **42**, 637 (1971).

52. Thick film resistive ink was purchased from Micro Circuits Co., Rt. 1, Box 518, New Buffalo, MI 49117.

53. C. L. Wellard, *Resistance and Resistors*, (McGraw-Hill, N.Y., 1960), p.46; G. W. O. Howe, Wireless Engineer **XII**, 291 (1935); H. E. Kern, J. M. McKenzie, IEEE Trans. Nuc. Sci. **NS-17 #1**, 260 (1970).

54. Braycoat 815Z, Bray Oil Co., Los Angeles, CA 90032.

55. J. H. Moore, C. C. Davis, M. A. Coplan, *Building Scientific Apparatus*, (Addison-Wesley, London, 1983), p.91.

56. J. W. Beams, J. D. Ross, J. F. Dillon, Rev. Sci. Instrum. **22**, 77 (1951). Many other references to Beams' work are given by P. J. Geary, *Magnetic and Electric Suspensions,* (British Scientific Instrument Research Association, Kent, 1964).

57. W. S. Cheung *et al.,* Precision Engineering **2**, 183 (1980).

58. W. R. Smythe, *Static and Dynamic Electricity,* 3rd. Ed. (McGraw-Hill, New

York, 1968), p.233. The author gives an expression for the torque on a dielectric prolate spheriod in a uniform electric field. In the limit where the dielectric constant is infinite it may be taken over to magnetostatics with $\mu \longrightarrow \infty$.

59. J. Strong, *Proceedures in Experimental Physics,* (Prentice-Hall, Englewood Cliffs, N. J., 1938). The 3 μm fibers were blown out by flame drag.

60. L. Holland, *Vacuum Deposition of Thin Films,* (Chapman and Hall, London 1956), p.493.

61. H. Rothe and W. Dahlke, Proc. IRE **44,** 811 (1956).

62. D. G. Blair in *Gravitational Radiation, Les Houches, 1982,* edited by Deruelle and Piran (North Holland, 1982).

63. R. Gifford, Phys. Rev. **D14,** 2478 (1976).

64. S. Barbanera *et al.*, J. Appl. Phys. **49,** 905 (1978).

65. F. Bordoni *et al.*, Rev. Sci. Instrum. **52,** 1079 (1981).

66. H. E. Kern and J. M. McKenzie, IEEE Trans. Nuc. Sci. **NS-17 #1,** 260 (1970); IEEE Trans. Nuc. Sci. **NS-17 #3,** 425 (1970); IEEE Trans. Nuc. Sci. **NS-19 #1,** 345 (1972).

67. S. Klein, W. Innes, and J. C. Price, Rev. Sci. Instrum. **56,** 1941 (1985).

68. A. Van der Ziel, Proc. IRE **50,** 1808 (1962).

69. F. Bordoni and G. V. Pallottino, Rev. Sci. Instrum. **48,** 757 (1977).

70. References to the original work and a brief history of high speed rotation are given by S. Whitley, Rev. Mod. Phys. **56,** 67 (1984).

71. J. P. Den Hartog, *Mechanical Vibrations*, 4th ed. (McGraw Hill, New York, 1956), chapter 6. The author also discusses a more realistic model that does not constrain the center of mass, the center of the shaft, and the axis of rotation to be colinear. The same results follow and in addition stability may be shown.

72. F. M. Dimentberg, *Flexural Vibrations of Rotating Shafts*, (Butterworths, London, 1961), pp.42–50.

73. D. Macchia, *Acceleration of an Unbalanced Rotor through the Critical Speed*, Cornell University Master's Thesis, 1963, ASME paper number 63-WA-9, available through Dialog.

74. W. Flugge, *Handbook of Engineering Mechanics*, 1st ed. (McGraw Hill, New York, 1962), p.61–8.

75. R. N. Arnold and L. Maunder, *Gyrodynamics and its Engineering Applications*, (Academic Press, New York, 1961). Chapter 12 discusses a problem similar to ours but without the translational degrees of freedom.

76. L. E. MacHattie, Rev. Sci. Instrum. **12**, 429 (1941); see also ref. 57.

77. V. V. Vladimirskii and S. M. Kalebin, Instruments and Experimental Techniques, English translation: p.216 (1960), Russian original: #2 p.41 (1959).

78. C. W. F. Everitt in *Proceedings of the First Marcel Grossmann Meeting on General Relativity*, edited by R. Ruffini (North-Holland, Amsterdam, 1977), p.545.

79. B. Rossi, Rev. Mod. Phys. **20**, 537 (1948).

80. A. D. Martin and K. J. McLean, J. Appl. Phys. **48**, 2950 (1977), and references therein.